REFERENCE ONLY

UNIVERSITY OF LONDON THESIS

Degree PhD Year 2005 Name of Author HAMAD GOMEZ

COPYRIGHT

This is a thesis accepted for a Higher Degree of the University of London. It is an unpublished typescript and the copyright is held by the author. All persons consulting the thesis must read and abide by the Copyright Declaration below.

COPYRIGHT DECLARATION

I recognise that the copyright of the above-described thesis rests with the author and that no quotation from it or information derived from it may be published without the prior written consent of the author.

LOAN

Theses may not be lent to individuals, but the University Library may lend a copy to approved libraries within the United Kingdom, for consultation solely on the premises of those libraries. Application should be made to: The Theses Section, University of London Library, Senate House, Malet Street, London WC1E 7HU.

REPRODUCTION

University of London theses may not be reproduced without explicit written permission from the University of London Library. Enquiries should be addressed to the Theses Section of the Library. Regulations concerning reproduction vary according to the date of acceptance of the thesis and are listed below as guidelines.

A. Before 1962. Permission granted only upon the prior written consent of the author. (The University Library will provide addresses where possible).

B. 1962 - 1974. In many cases the author has agreed to permit copying upon completion of a Copyright Declaration.

C. 1975 - 1988. Most theses may be copied upon completion of a Copyright Declaration.

D. 1989 onwards. Most theses may be copied.

This thesis comes within category D.

☑ This copy has been deposited in the Library of UCL.

☐ This copy has been deposited in the University of London Library, Senate House, Malet Street, London WC1E 7HU.

The Royal Institution of Great Britain
Davy-Faraday Research Laboratory

Department of Chemistry
University College London

Computational study of the nucleation and growth of ZnS

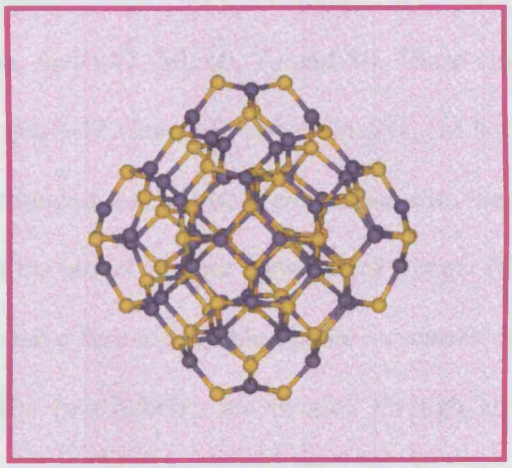

by

Said Hamad Gomez

2005

Supervisors: Prof. Richard Catlow and Dr. Dewi Lewis

UMI Number: U592889

All rights reserved

INFORMATION TO ALL USERS
The quality of this reproduction is dependent upon the quality of the copy submitted.

In the unlikely event that the author did not send a complete manuscript
and there are missing pages, these will be noted. Also, if material had to be removed,
a note will indicate the deletion.

UMI U592889
Published by ProQuest LLC 2013. Copyright in the Dissertation held by the Author.
Microform Edition © ProQuest LLC.
All rights reserved. This work is protected against
unauthorized copying under Title 17, United States Code.

ProQuest LLC
789 East Eisenhower Parkway
P.O. Box 1346
Ann Arbor, MI 48106-1346

ABSTRACT

Several computational techniques have been employed to perform an extensive theoretical study of different aspects of ZnS nucleation and growth. First, we use Density Functional Theory and ineratomic potential based calculations to calculate the surface energies for the most common surfaces in the two crystalline phases of ZnS; wurzite and sphalerite. This study allows us to calculate the crystal morphologies for both phases, which agree with those observed experimentally. The predicted morphologies correspond to those that crystallites of micrometer sizes would adopt, but in order to understand the nucleation processes we need models for nanoclusters. We therefore use a global minimization technique (simulate annealing), with which we obtain the most stable configuration in vacuum for (ZnS)n clusters, n=10-47, 50, 60, 70 and 80. These clusters are classified into two groups. Clusters with n=10-47, denoted bubble clusters, are hollow structures in which all the atoms are three coordinated. Such structures contrast with the expectation of bulk-like structures in which most of the atoms are four coordinated. Larger $(ZnS)_n$ clusters (n=50, 60, 70 and 80) adopt what we have denoted double bubble structures, in which one big bubble encloses a smaller one. The two bubbles are bonded through covalent bonds, therefore creating a network of four coordinated atoms. Density Functional Theory as well as interatomic potential based calculations are employed to calculate the properties of these particles. The thesis concludes with a molecular dynamics study of the nucleation of ZnS in water solution, which reveals that bubble clusters are also formed in the presence of water, and gives insight into the detailed mechanisms of their formation.

Caminante, son tus huellas
el camino, y nada mas;
caminante, no hay camino,
se hace camino al andar.
Al andar se hace camino,
y al volver la vista atrás
se ve la senda que nunca
se ha de volver a pisar.
Caminante, no hay camino,
Sino estelas en la mar.

Wanderer, your footsteps are
the road, and nothing more;
wanderer, there is no road,
the road is made by walking.
By walking one makes the road,
and upon glancing behind
one sees the path
that never will be trod again.
Wanderer, there is no road,
only wakes upon the sea.

Antonio Machado

Acknowledgements

I would like to express my appreciation and gratitude to my supervisor, Professor Richard Catlow, for his great support, encouragement and guidance throughout the course of this thesis.

Thanks to the EU, for funding my research through the NUCLEUS project, and to my secondary supervisor, Dr. Dewi Lewis, who helped me in many occasions.

I would also like to thank Dr. Alexei Sokol, with whom I had many fruitful discussions, and whose continuous pushing helped me to finish on time.

Thanks also to Dr. Eleonora Spanó and Dr. Sylvain Cristol, with whom many results of this thesis have been obtained.

To my friends in The Royal Institution, who have made my stay very enjoyable: Luis, Manuel, Eleonora, Gloria, Naseem, Rafael, Aurora, Iman, Alexei, David, Dan, Andrew, Matt, Amber, Will, Scott, Sam, Marc, and many others.

To Dr. Jose Antonio Mejias, who induced me to be a scientist.

Finally, I would like to thank my mother, brother and sister, for all their love, and my fianceé, for making this thesis possible with her constant love and support.

Contents

List of figures

List of tables

CHAPTER 1

METHODOLOGY

1.1 INTRODUCTION

This thesis aims to improve our understanding of the processes of nucleation and growth of Zinc Sulphide. ZnS has two polymorphs: the most stable at room temperature sphalerite (cubic) structure and the stable at high temperatures wurtzite (hexagonal) phase. The local structure is the same in both phases with a tetrahedral coordination for both zinc and sulphur. The two phases differ only through the stacking of the atomic planes: AB for sphalerite and ABC for wurtzite. Although the sphalerite phase is more stable than wurzite, it is common to find both in the same sample, and it is not clear which factors control which phase predominates.

The peculiar characteristics of ZnS make this compound appropriate to study the nucleation events from solution, which may be defined as the process by which atoms, ions or molecules in solution aggregate to form a stable cluster, a nucleus, which then acts as a seed for the crystal growth. Therefore, the characteristic of the nucleus will greatly influence the nature and properties of the growing crystal.

Crystal nucleation and growth is a key process, with huge importance in many different fields. For example a deeper knowledge of nucleation events could help to improve the processes of pharmaceutical drugs synthesis[1], while photographic, agrochemistry and computer industries also need to obtain a better understanding of nucleation events. Despite its great importance, there is little understanding at the atomic level of nucleation processes.

A typical nucleus is expected to consist of between ten and several hundred atoms, and its life span is extremely short, which is the basis of the difficulty in experimental studies[2]. Several investigations have been devoted to theoretical studies of nucleation processes[3, 4], but due to computing time limitations only simple to model systems are usually considered.

We adopt a two-pronged approach in understanding the nucleation process. The typical nuclei are clusters containing hundreds or a few thousands atoms - too many to permit an accurate atomistic description. Using thermodynamic principles, we can obtain information of the properties of small crystallites, which could consist of several thousands of atoms, with a size of few μm. Although this size is larger than that of the nuclei in which we are interested, it is important to know the characteristics of ZnS crystals on the micro-metre scale, because nuclei reach this size if they continue to grow. The other approach is to understand the behaviour of smaller clusters (nanoclusters), with very few atoms. We use computational techniques to obtain information on the atomistic processes involved in the formation and growth of ZnS nanoclusters. This two-pronged approach allows us to infer important features of the nucleation of ZnS.

There is an additional incentive to study nanoclusters, in which the number of atoms at the surfaces is comparable to the number of those which are located in the crystalline lattice itself. Physical and chemical properties of materials composed of nanoclusters are thus different to the properties of "normal" materials, which are dominated by the bulk[5] lattice properties.

A promising effect takes place in nanocrystalline semiconductors. Usually the de Broglie wavelength of electrons (and holes) is a few nanometers -very small compared to the size of the semiconductor in common electronic devices. But this wavelength is comparable to the size of a nanocrystal. Therefore the charge carriers must be treated quantum mechanically as "particles in a box", where the size of the box is given by the dimensions of the nanocrystal. This changes drastically the electronic properties of the semiconductor. For example the valence and conduction bands are no longer continuous, but split into discrete levels. The band gap and the spacing between these levels increase as the crystal size decreases. It is thus of relevance to have a good knowledge about the size and morphology of these crystals. These small semiconductor nanocrystals are usually known as quantum dots, and the material composed of these crystals is referred to as quantized matter.

Quantum dots have properties that could lead to new electronic devices. II-VI, II-V, III-V and other semiconductors are being investigated as possible materials to be used in these devices[6-9].

Following this introduction, we briefly summarise the structure of the thesis.

In chapter 1 we give an overview of the theoretical methods used in our study. In chapter 2 we use classical and quantum energy minimization techniques to make a comprehensive survey of the surfaces exposed in ZnS crystals, allowing us to predict the morphologies of small crystals for both phases. The effect of temperature on two of these surfaces is also investigated, using molecular dynamics calculations. Chapter 3 explains how we calculate the minimum energy structures of $(ZnS)_n$ clusters in vacuum for n=10-47, using simulated annealing. The most stable structures are found to be the "bubble" clusters. Since bulk-like clusters had been expected to be more stable, we performed DFT calculations to compare the energies of bubbles and bulk-like clusters, confirming that the latter are less stable. The next cluster studied is $(ZnS)_{60}$, which has a new structure, called double bubble, in which a large bubble encloses a smaller one. The geometry of that cluster is also reviewed in chapter 3. In chapter 4, the clusters $(ZnS)_{70}$ and $(ZnS)_{80}$ are presented (the difference of 10 ZnS units between two successive clusters is due to the great increase of computer time needed to perform the calculations). The structure of $(ZnS)_{50}$ is also calculated in order to gain an idea of the size in which double bubbles start to appear. These four large clusters are also double bubbles. In that chapter, we also calculate some properties that would be of interest for experimentalists trying to determine whether a certain set of clusters are bubble or bulk-like clusters. The final chapter contains a molecular dynamics study of the nucleation of ZnS clusters from the Zn^{2+} and S^{2-} ions in water solution. The results suggest that bubble clusters are indeed formed at room temperature without the need of any template.

1.2 THEORETICAL METHODS

In this chapter, we will discuss the different techniques employed in our study. The main approach used in this study is *lattice statics simulation*, in which we minimize the total energy of the lattice in order to determine the surface structure, employing interatomic potentials. Moreover, as noted, we have verified some of the surface and cluster structures with electronic structure techniques using Density Functional Theory, DFT. There is a great difference between Interatomic Potentials (IP) and DFT based calculations. IP calculations are simpler, being based on a semi-classical approximation of matter, while DFT takes into account its electronic structure, with its quantum characteristics. DFT is a powerful but time consuming technique, so we only use it in few key cases, in order to check the results obtained with IP calculations, which are entirely adequate for many of the problems studied.

1.2.1 Interatomic Potential Techniques

Classical Simulations are based upon a number of assumptions, strongly related to the physical behavior of the atoms that constitute the matter. These assumptions are gathered together to form what it is usually called the Born model of Solids. Within this model the crystal is assumed to be composed of formally charged ions. In reality there is no a clear separation between covalent and ionic crystals, so it is possible to use this model to study partially ionic crystals, such as ZnS.

The ions comprising the crystal interact with all the others by means of many kinds of forces. We assume that these forces have something in common; they only depend upon the atomic positions, so they do not depend upon the atomic velocities or accelerations (as, for instance, magnetic forces would do). Mathematically it means that the forces can be derived

from a potential energy function. Thus it is possible to obtain information about how the system behaves by having a good description of the potential energy of the system.

There are two main contributions to the energy of the system: the long-range interaction, i.e. the electrostatic interaction between the charges of all the ions to which is added a short-range potential:

Eq. 1 $$V_{Total}(\vec{r}_1,\ldots,\vec{r}_N)=\sum\left(\frac{1}{4\pi\varepsilon_o}\frac{q_iq_j}{r_{ij}}\right)+V_{Short-range}(\vec{r}_1,\ldots,\vec{r}_N),$$

where q_i and q_j are the charges of the interacting ions i and j, r_{ij} the distance between them and $\vec{r}_1,\ldots,\vec{r}_N$ are the positions of the N atoms.

1.2.1.1 *The Ewald sum*

The most important contribution to the total energy of ionic systems is the electrostatic energy. This energy is usually calculated following the Ewald method, which is used for periodic systems.

With this construction, each box is defined by a vector $\vec{n}=(n_xL,n_yL,n_zL)$ where n_x, n_y, n_z are integers and L is the length of the simulation box edges. This enables us to calculate the Coulombic energy of the simulation box, which is the sum of all the electrostatic interactions between the N ions in it and the sum of the interactions of these ions with all its periodic images. This energy is then expressed as:

Eq. 2 $$V_{Coulomb}=\frac{1}{2}\sum_{|\vec{n}|=0}^{\infty}{}'\sum_{i=1}^{N}\sum_{j=1}^{N}\frac{1}{4\pi\varepsilon_0}\frac{q_iq_j}{\left|\vec{r}_{ij}+\vec{n}\right|}$$

where the prime indicates that, when $|\vec{n}|=0$, the term i=j is not included.

The electrostatic energy is calculated as an infinite series. Half of the terms are positive and the other half negative. The positive terms form a divergent series. The complete series is then conditionally convergent, the sum depends on the order in which the terms are summed. Ewald solved this problem[10]. The Ewald method consists in splitting the conditionally convergent series into two convergent series, each of which converges rapidly. This is achieved by surrounding each point charge by a Gaussian charge distribution of equal magnitude and opposite sign, centered on the point charge, as shown in Figure 1.1a These Gaussian charges distributions screen the point charges they are surrounding, making lower the interactions between then. They are usually written as:

Eq. 3 $$\rho_i(\vec{r}) = \frac{q_i \alpha^3}{\pi^{3/2}} \exp(-\alpha^2 r^2)$$

The sum of the point charges plus these screening Gaussians is now a rapidly convergent series, which is summed in real space:

Eq. 4 $$V_{real} = \frac{1}{2} \sum_{i=1}^{N} \sum_{j=1}^{N} \sum_{|\vec{n}|=0}^{\infty}{}' \frac{1}{4\pi\varepsilon_0} \frac{q_i q_j}{|\vec{r}_{ij} + \vec{n}|} \operatorname{erfc}(\alpha |\vec{r}_{ij} + \vec{n}|)$$

where erfc is the complementary error function.

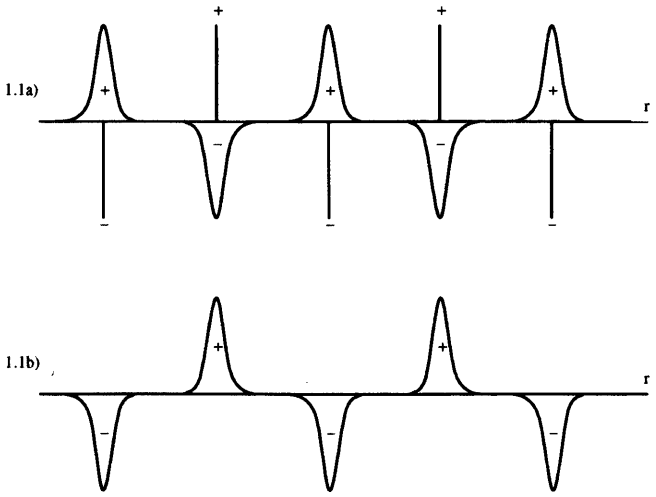

Figure 1.1

Charge distribution in the Ewald sum. Energy of distribution a) is calculated in real space and b) in reciprocal space.

Another charge distribution must be added in order to maintain the remove the effect of the added charges (see Figure 1.1b). This second distribution gives an electrostatic energy that is easier to calculate in reciprocal space:

Eq. 5 $$V_{reciprocal} = \frac{1}{2}\sum_{\vec{k}\neq 0}\sum_{i=1}^{N}\sum_{j=1}^{N}\frac{1}{\pi L^3}\frac{q_i q_j}{4\pi\varepsilon_0}\frac{4\pi^2}{k^2}\exp(-\frac{k^2}{4\alpha^2})\cos(\vec{k}\vec{r}_{ij})$$

where $\vec{k}$ are the reciprocal vectors, $\vec{k} = \frac{2\pi\vec{n}}{L^2}$.

In the sum calculated in real space the interaction of each Gaussian with itself is included:

Eq. 6 $$V_{self-energy} = -\frac{\alpha}{\sqrt{\pi}}\sum_{k=1}^{N}\frac{q_k^2}{4\pi\varepsilon_0}$$

The total electrostatic energy of the simulation box can be expressed as:

Eq. 7

$$V_{Coulomb} = \frac{1}{2}\sum_{i=1}^{N}\sum_{j=1}^{N}\left\{\begin{array}{l} {\sum_{|\vec{n}|=0}^{\infty}}' \frac{1}{4\pi\varepsilon_0}\frac{q_i q_j}{|\vec{r}_{ij}+\vec{n}|} erfc\left(\alpha|\vec{r}_{ij}+\vec{n}|\right) \\ \sum_{\vec{k}\neq 0}\frac{1}{\pi L^3}\frac{q_i q_j}{4\pi\varepsilon_0}\frac{4\pi^2}{k^2}\exp\left(-\frac{k^2}{4\alpha^2}\right)\cos\left(\vec{k}\vec{r}_{ij}\right) \\ -\frac{\alpha}{\sqrt{\pi}}\sum_{k=1}^{N}\frac{q_k^2}{4\pi\varepsilon_0} \end{array}\right.$$

1.2.1.2 *The short-range potential*

The electrostatic term is not the only one between ions. There are many other interactions in the crystal, referred to collectively as short-range interactions. The short-range energy is usually expressed as:

Eq. 8 $$V_{Short-range}(\vec{r}_1,...,\vec{r}_N) = \sum_{ij} V_{ij}(r_{ij}) + \sum_{ijk} V_{ijk}(r_{ijk}) + \sum_{ijkl} V_{ijkl}(r_{ijkl}) + ...$$

where V_{ij} refers to all two-body interactions, V_{ijk} to three-body interactions, V_{ijkl} to four-body interactions, and so on.

The most important contribution to the short-range interactions comes from the two-body interactions. There are many different potentials to model these two-body interactions. The best known of all is the 12-6 Lennard-Jones potential, which is a particular case of this general expression:

Eq. 9 $$V_{ij}(r_{ij}) = \frac{A}{r^n_{ij}} - \frac{B}{r^m_{ij}}$$

where A and B are fitted parameters and n and m are integer numbers. For the Lennard-Jones potential n=12 and m=6.

The first term models the repulsive interactions due to the Pauli forces, and the second one the attractive interactions due to the Van der Waals dispersion forces. At short distances the repulsive forces become much higher than the attractive ones. It implies that n must be greater than m. The r^{-6} dependence of the attractive forces has a physical background; it can be obtained from theoretical studies of the dispersion energy. In Figure 1.2 the Lennard-Jones 12-6 potential is plotted.

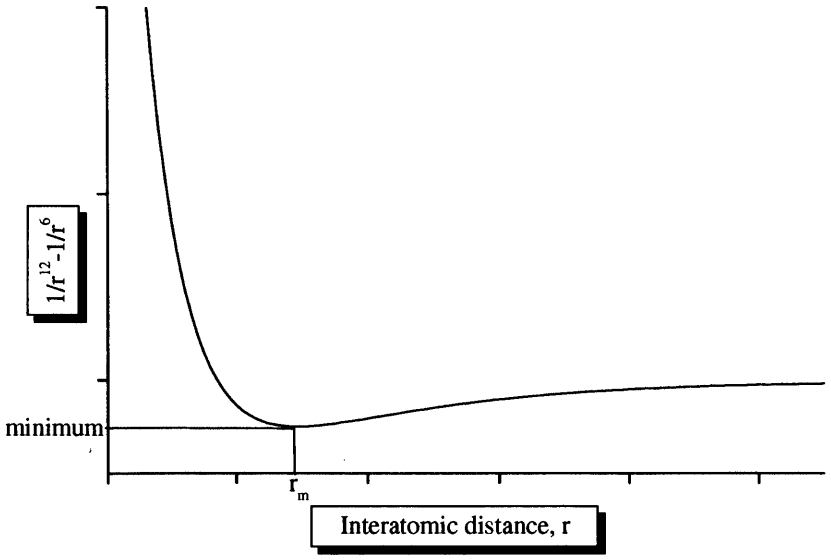

Figure 1.2

Plot of the Lennard-Jones 12-6 potential as a function of interatomic separation.

There is an energy minimum distance, r_m, dependant on the fitted parameters A and B. In the proximity of the minimum an exponential function could describe better the repulsive part of the potential. The Buckingham potential uses the r^{-6} term to model the dispersion forces, but the repulsive forces are modelled with an exponential function:

Eq. 10
$$V_{ij}(r_{ij}) = A\exp\left(-r_{ij}/\rho\right) - \frac{C}{r_{ij}^6}$$

where A,ρ and C are fitted parameters

Buckingham potentials generally perform better for ionic systems than Lennard-Jones potentials. In part, this could be due to the fact that it has three fitted parameters, one more than Lennard-Jones. In our case we use a mixed Buckingham and Lennard-Jones 9-6 potential to model the two-body short-range interaction.

Eq. 11
$$V_{ij}(r_{ij}) = A\exp\left(-r_{ij}/\rho\right) + \frac{B}{r_{ij}^9} - \frac{C}{r_{ij}^6}$$

With four fitted parameters (A, B, ρ and C) we obtain a better description of the system.

The second main contribution to the short-range energy is the three-body energy. It is necessary when dealing with covalent bonds, because of the directionality of the bonding. It is usually expressed as a harmonic potential:

Eq. 12 $$V_{ijk}(r_{ijk}) = \frac{1}{2} K_{TB} \left(\theta_{ijk} - \theta_o\right)^2,$$

where θ_o is the equilibrium angle between the three atoms and K_{TB} is a fitted constant. In our case we used a three-body term in order to take into account the directionality of the covalent S-Zn-S and H-O-H bonds.

The contribution of the four-body interactions to the total energy of ionic systems is small, so usually it is not taken into account. For covalent systems, it may be necessary to have a good description of a certain torsional angle of the system, as in the benzene molecule for example. The most common form of the four-body energy is as follows:

Eq. 13 $$V_{ijkl}(r_{ijkl}) = A\left(1 + \cos B\Psi_0\right),$$

where A is a fitted parameters, B is related to the periodicity of the four body angle and Ψ_o is the equilibrium torsional angle between the four atoms. However, it is not necessary to use four-body potentials to describe correctly ZnS.

Short-range interactions tend to zero rapidly when the interatomic distance increases. Therefore we can assume that every atom interacts not with all the atoms, but only with those atoms inside a certain spherical region of radius r_c. This cut off radius must be large enough to ensure that the interaction with the atoms outside this region is indeed negligible. In our case a cut off radius of 15 Å was found to be sufficient. In Figure 1.3 we can see the variation of the lattice energy as a function of the cut off radius. Another cut off distance is used for the three-body interactions. Since only first neighbors must be treated, shorter cut off radii are used, 2.6 Å for the Zn-S distance and 4.4 Å for the S-S distance.

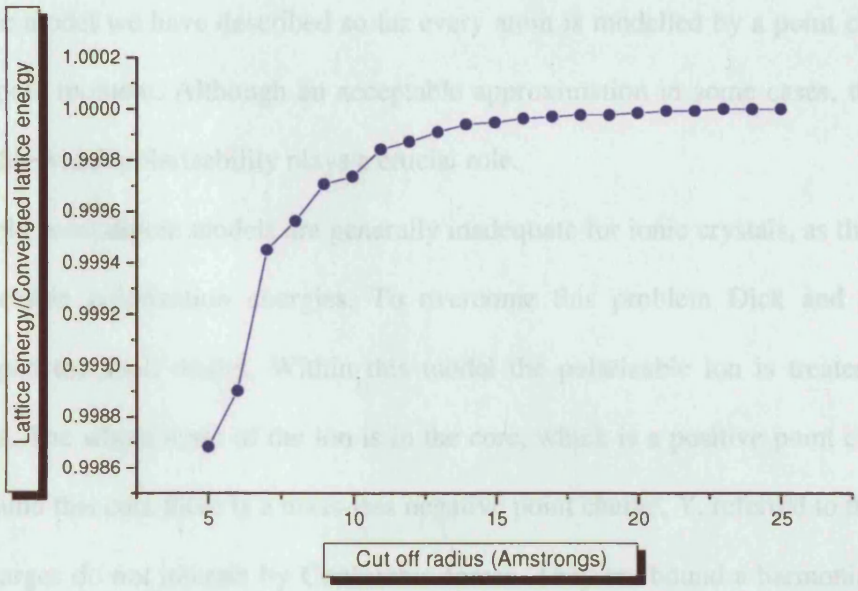

Figure 1.3

Lattice energy dependence with the cut-off radius for bulk ZnS, taking the converged value as reference, 1.

1.2.1.3 *Shell model*

In the model we have described so far every atom is modelled by a point charge, without any dipole moment. Although an acceptable approximation in some cases, there are many atoms for which polarisability plays a crucial role.

Simple point dipole models are generally inadequate for ionic crystals, as they often result in excessive polarization energies. To overcome this problem Dick and Overhauser[11] developed the shell model. Within this model the polarizable ion is treated as a pair of charges. The whole mass of the ion is in the core, which is a positive point charge of value X. Around this core there is a mass-less negative point charge, Y, referred to the shell. These two charges do not interact by Coulombic forces. They are bound a harmonic spring force, with a constant K:

Eq. 14
$$V_{ij}^{core-shell}(r_{ij}) = \frac{1}{2} K r_{ij}^2 ,$$

where r_{ij} is the core-shell separation, K is fitted as well as the shell charge.

The sum of the core charge and the shell charge leads to the total charge of the ion. As we can see in Figure 1.4, the higher the distance between core and shell, the higher the dipole moment of the ion, $\vec{d}$.

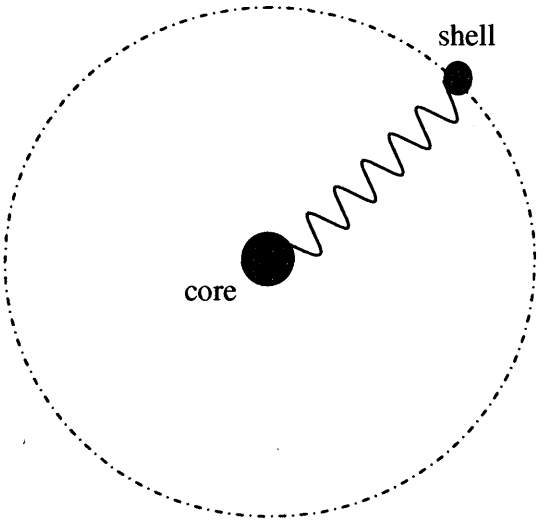

Figure 1.4

Schematic representation of an ion composed by core and shell.

The polarisability of the ion (α) is given by:

Eq. 15 $$\alpha = \frac{Y^2}{K}$$

The short-range interaction forces are mainly due to the interaction between electron clouds. Therefore in the shell model, short-range forces act between shells. Despite its simplicity, this model works well in static and dynamical simulations of ionic crystals.

1.2.1.4 *Energy minimization: MARVIN*

In the previous sections different models for calculating the energy of the systems have been presented. We are interested in finding the equilibrium state of the system. This state corresponds to a minimum in the potential energy hypersurface, in which:

Eq. 16 $$\frac{\partial V_{Total}(\vec{r}_1,...,\vec{r}_N)}{\partial r_i} = 0 \qquad i=1,.....,3N \quad ,$$

where $V_{Total}(\vec{r}_1,...,\vec{r}_N)$ is the total potential energy of the system, as defined in Eq. 1, and N is the number of atoms.

Transition states and local minima also satisfy Eq. 16, therefore it is necessary to calculate the second derivative to distinguish between a minimum and a transition state.

There are several minimisation algorithms. We use the MARVIN code[12] for surface calculations with interatomic potentials (IP), as discussed in greater detail below. MARVIN makes efficient use of three different minimization algorithms. System configurations at the beginning of the minimization may be far away from a minimum. The most efficient algorithm in this case is the downhill Simplex method, which requires only function evaluations, not derivatives. The Conjugate Gradient method requires both the energy and first derivative evaluations, and is the most efficient method at intermediate distances from the minimum. The norm of the gradient is checked to ascertain whether to switch from one method to another. When the system is very close to the energy minimum this method is very slowly convergent, so we now switch to the Newton method, which makes use of the second derivatives of the energy, in order to reach rapidly the energy minimum.

We have to define certain tolerance levels that will determine when the system has reached an energy minimum. Usually the optimization is stopped when the energy differences and displacements between two consecutive cycles, and also the energy gradients, are below these levels. Figure 1.5 shows the general scheme followed in geometry optimizations.

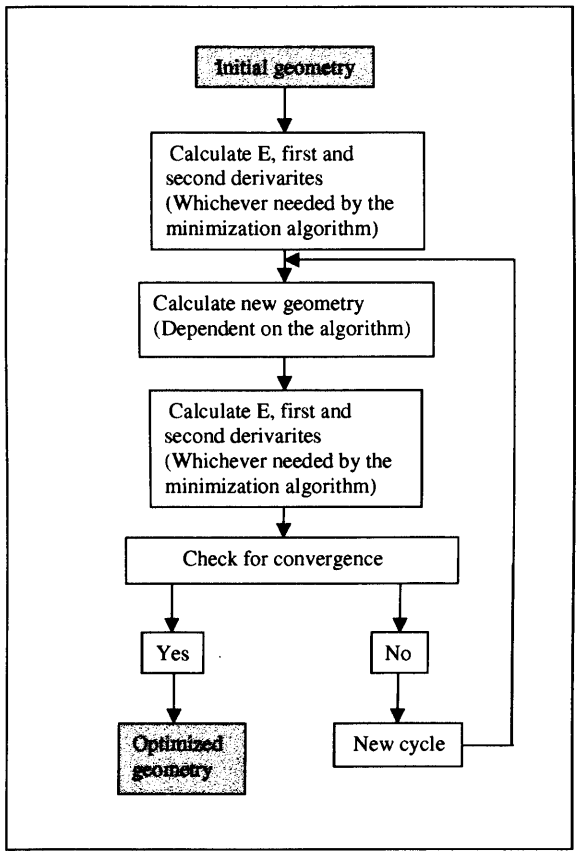

Figure 1.5

General scheme of an energy minimization process

Within the MARVIN approach the surface is modelled by repeating periodically the unit cell in two dimensions. The unit cell is split into two regions (Figure 1.6). Region 1 contains the surface atoms and the atoms near the surface region. All the atoms in region 1 are allowed to relax. The atoms in region 2 are kept fixed, in the equilibrium positions of the bulk structure and model the effect of the bulk on the surface.

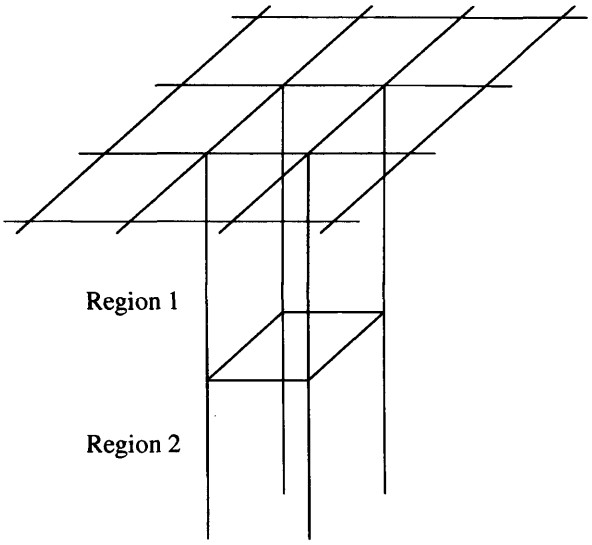

Figure 1.6

Schematic representation of the unit cell used in the MARVIN code, repeated in two dimensions and split in two regions. Atoms in Region 1 are allowed to relax, and atoms in Region 2 are kept fixed. The thickness of regions 1 and 2 is typically 15Å and 20Å, repectively.

If we only take into account the two-body terms, the total energy is calculated as:

$$\text{Eq. 17} \quad E_{total}^{(2)} = \sum_{a}^{N_1} \left[\frac{1}{2} \sum_{\vec{l} \neq 0} V_{aa}(|\vec{l}|) + \frac{1}{2} \sum_{b \neq a}^{N_1} \sum_{\vec{l}} V_{ab}(|\vec{r}_{ab} + \vec{l}|) + \sum_{b}^{N_2} \sum_{\vec{l}} V_{ab}(|\vec{r}_{ab} + \vec{l}|) \right]$$

where N_1 and N_2 are the total number of particles in regions 1 and 2 respectively, $\vec{l}$ are the two-dimensional lattice vectors and $\vec{r}_{ab}$ is the vector between particles a and b. The first term in the square brackets describes the interactions between a particle and its periodic images. The second describes the interactions between all region 1 particles and their periodic images. The factor of 1/2 eliminates double counting. The third term describes the

interactions between region 1 and region 2 particles. Analogous equations describe the energy for the three- and four-body interactions.

Two parameters of the calculation must be checked carefully to ensure a correct description of the surface. First, the thickness of region 2 must be large enough for the atoms at the bottom of region 2 to have a negligible interaction with the atoms of the bottom of region 1. Secondly, the thickness of region 1 must be large enough to ensure that the energy (per surface area unit) is converged. In our study, surface vectors range from 5 to 8 Å and region 1 is made of typically 8 layers (~15 Å) while region 2 contains approximately 10 layers (~20Å). This leads to a total number of atoms of ~150 for a 1x1 simulation cell, ~600 for a 2x2 and ~1400 for a 3x3 cell.

1.2.1.5 *Molecular Dynamics: DLPOLY*

Energy minimization techniques are useful when we wish to obtain the equilibrium state of the system. But this approach has many limitations. For example the effect of temperature is not taken into account. Moreover, time plays no role at all, so it is not possible to obtain information about any physical time-dependant property. The most obvious way of introducing both time and temperature in our treatment of the atoms is by using Newton's equations of motion for each atom i:

Eq. 18 $$m_i \frac{d^2\vec{r}_i}{dt^2} = -\vec{\nabla}_i V_{Total}(\vec{r}_1,...,\vec{r}_N) \qquad i=1,....,N$$

where m_i is the mass of the i atom, r_i its position vector, N the number of atoms and $V_{Total}(\vec{r}_1,...,\vec{r}_N)$ is the total potential energy of the system, as defined in Equation 1. Solving these equations we obtain the trajectory of every particle throughout time. This technique based on this simple approach is known as molecular dynamics (MD). The calculation of thermodynamic properties from such simulations is generally not straightforward. For example, the temperature is directly related to atom velocities, but the calculation of other properties like enthalpy or free energy is more difficult.

There are several programs for solving Newton's equations of atomistic systems. We use one of the most comprehensive: DLPOLY[13]. The algorithm used for solving the equations is based around the Verlet method[14]. Within this method positions, velocities and accelerations are expressed as Taylor expansions:

Eq. 19 $$\vec{r}(t+\delta t) = \vec{r}(t) + \delta t\vec{v}(t) + \frac{1}{2}\delta t^2\vec{a}(t) + ...$$

Eq. 20 $$\vec{v}(t+\delta t) = \vec{v}(t) + \delta t\vec{a}(t) + \frac{1}{2}\delta t^2\vec{b}(t) + ...$$

Eq. 21 $$\vec{a}(t+\delta t) = \vec{a}(t) + \delta t\vec{b}(t) + \frac{1}{2}\delta t^2\vec{c}(t) + ...$$

The Verlet algorithm uses the positions and accelerations at time t and the positions from the previous step, to calculate the new positions at (t+δt). This time step δt must be small enough to ensure that the system does not change significantly between t and (t+δt) (usually δt ranges from 0.1fs to 10fs). If this is the case the solutions obtained are very similar to the ones that would be obtained solving analytically the Newton's equations.

The trick of the Verlet algorithm is to add the positions at time (t+δt) and (t-δt), with the second order of approximation:

Eq. 22 $$\vec{r}(t+\delta t) = \vec{r}(t) + \delta t\vec{v}(t) + \frac{1}{2}\delta t^2\vec{a}(t),$$

Eq. 23 $$\vec{r}(t-\delta t) = \vec{r}(t) - \delta t\vec{v}(t) + \frac{1}{2}\delta t^2\vec{a}(t),$$

giving:

Eq. 24 $$\vec{r}(t+\delta t) = 2\vec{r}(t) - r(t-\delta t) + \delta t^2\vec{a}(t).$$

Velocities are not needed for solving the equations. But they are needed for calculating thermodynamic properties. Velocities may be calculated by dividing the difference in positions at times (t+δt) and (t-δt) by 2δt:

Eq. 25 $$\vec{v}(t) = \frac{[\vec{r}(t+\delta t) - \vec{r}(t-\delta t)]}{2\delta t}$$

But this method is not very precise. As can be seen from Eq. 24, r(t+δt) is obtained by adding a small term ($O(\delta t^2)$) to a difference of two large terms ($O(\delta t^0)$), which leads to loss of accuracy in the calculation.

The Verlet leap-frog algorithm[15] does not have this problem. The leap-frog algorithm is based on these equations:

Eq. 26 $$\vec{r}(t+\delta t) = \vec{r}(t) + \delta t \vec{v}(t+\tfrac{1}{2}\delta t),$$

Eq. 27 $$\vec{v}(t+\tfrac{1}{2}\delta t) = \vec{v}(t-\tfrac{1}{2}\delta t) + \delta t \vec{a}(t).$$

Velocities at time t may be calculated by:

Eq. 28 $$\vec{v}(t) = \frac{1}{2}\left[\vec{v}(t+\tfrac{1}{2}\delta t) + \vec{v}(t-\tfrac{1}{2}\delta t)\right].$$

Hence the velocities "leap-frog" over the positions to give their values at (t+½ δt). Then the positions leap over the velocities to give their new values at (t+δt), and so on.

The initial step in a molecular dynamics calculation is to assign the initial atom velocities distribution. Usually the velocities are randomly chosen from a Gaussian distribution. Any other random selection leads to similar results, but less efficiently, i.e. more time consuming. The Maxwell-Boltzmann distribution is rapidly established by molecular collisions within typically a few hundreds time steps. Therefore an atom i of mass m_i has a probability $p(v_{ix})$ of having a velocity v_{ix} in the x direction at a temperature T, given by the Maxwell-Boltzmann distribution:

Eq. 29 $$p(v_{ix}) = \left(\frac{m_i}{2\pi k_B T}\right)^{1/2} \exp\left[-\frac{1}{2}\frac{m_i v_{ix}^2}{k_B T}\right]$$

The temperature of the system is calculated using statistical mechanics relationships:

Eq. 30 $$K = \sum_{i}^{N} \frac{1}{2} m_i v_i^2 = \frac{k_B T}{2} (3N - N_C),$$

where N is the number of particles and Nc is a parameter related with the number of constraints of the system, which take the value 4 for a single atom, 5 for a linear molecule and 6 otherwise.

Due to the random choice of initial velocities, any physical property calculated from these values is not realistic. It is necessary to run for a long enough period until the properties of the system do not change with time. When that is achieved the system is equilibrated, and the time required is known as the equilibration period. Results of the calculation are only analyzed after this period, in the production period.

There are several ensembles in which we can run calculations, depending on the conserved quantities: NVE, NVT, NPT, etc. In this thesis we mainly use the NVT and NPT ensembles, with two different thermostats: Evans thermostat and Nosé-Hoover thermostat. In the Evans NVT thermostat (also called isokinetic thermostat) the temperature is kept exactly at a constant value during the whole calculation. The equations describing the dynamics of the system are isokinetic Gaussian equations of motion, and were proposed by Hoover et al[16, 17] and Evans et al[18, 19].

The modified Hamiltonian equations of motion in this case are:

Eq. 31 $$\frac{d\vec{r}_i(t)}{dt} = \vec{v}_i(t)$$

Eq. 32 $$\frac{d\vec{v}_i(t)}{dt} = \frac{\vec{f}_i(t)}{m_i} - \alpha(t)\vec{v}_i(t)$$

The additional frictional parameter α(t) is obtained from the requirement that the total kinetic energy is constant. From Eq. 30:

Eq. 33

$$\frac{dK}{dt} = \sum_i^N m_i \vec{v}_i(t) \frac{d\vec{v}_i(t)}{dt} = 0$$

$$\Rightarrow \sum_i^N m_i \vec{v}_i(t) \left[\frac{\vec{f}_i(t)}{m_i} - \alpha(t)\vec{v}_i(t) \right] = 0$$

$$\Rightarrow \alpha(t) = \frac{\sum_i^N \vec{v}_i(t)\vec{f}_i(t)}{\sum_i^N m_i \vec{v}_i^2(t)}$$

This additional force is applied to the system at each step during the whole calculation. In the Nosé-Hoover NVT thermostat, the temperature is not kept constant, but it is allowed to oscillate. In this case the Hamiltonian equations of motion are:

Eq. 34

$$\frac{d\vec{r}(t)}{dt} = \vec{v}(t),$$

Eq. 35

$$\frac{d\vec{v}(t)}{dt} = \frac{\vec{f}(t)}{m} - \alpha(t)\vec{v}(t),$$

where $\alpha(t)$ is a frictional parameter controlled by the following first order differential equation:

Eq. 36

$$\frac{d\alpha(t)}{dt} = \frac{1}{\tau_T^2}\left(\frac{T}{T_0} - 1\right),$$

where τ_T is a time constant that must be calculated for each system to give the best results (its value is typically between 0.5 to 2 ps), and T is the instant temperature, as calculated from Eq. 30.

The equation that describe the Evans thermostat (Eq. 31 and Eq. 32) are similar to those describing the Nosé-Hoover thermostat (Eq. 34 and Eq. 35); the only difference is the frictional factor that multiplies the velocities in the calculation of the accelerations. As noted

before, the Evans thermostat does not allow any oscillation of the temperature, which is always kept constant at a desired value. In the Nosé-Hoover thermostat, the frictional factor varies in time, controlled by Eq. 36. The consequence is that there is an influence over the system to change its temperature, but that temperature is not achieved instantly, it takes some time, which causes oscillations of temperature that occur during the whole simulation.

In Molecular Dynamics simulations there are problems implementing the shell model relating to solving the equations of motion for the shells. In energy minimization they are modelled as massless particles. But a massless particle would experience an infinite acceleration in response to a finite force when solving Newton's equations. It can be avoided by performing an energy minimization of shells at each step[20]. The alternative is to assign a small mass to the shell[21, 22], i.e. the adiabatic method, which is implemented in DLPOLY. The harmonic spring force between core and shell makes them vibrate with a frequency:

Eq. 37
$$\nu = \frac{1}{2\pi}\left[\frac{K}{x(1-x)m}\right]^{1/2},$$

where m is the atomic mass ($m=m_{core}+m_{shell}$) and $x=m_{shell}/m_{core}$.

The ion comprising core and shell may then be regarded as a diatomic molecule with a harmonic bond.

There is a certain energy associated with the vibrations of the core-shell unit. This energy steadily increases during the simulations, and it may be a problem in long simulations, since this causes a transfer of energy from the rest degrees of freedom of the system to this unphysical degree of freedom. In Chapter 5 we explain how we solved this problem, by introducing a frictional force in the core-shell motion, which keeps the vibrations below an acceptable level, while also giving a proper description of the polarizability.

1.2.2 Electronic Structure techniques; Density Functional Theory

The Schrödinger equation ($H\Psi = E\Psi$) has all the information needed for a complete quantum description of a time-independent physical system. The Hartree-Fock method[23] (HF) gives an approximate solution, but does not account for electronic correlation. Post-HF[24] techniques (Moller-Plesset, Configuration Interaction, etc) include correlation effects that are very time consuming and are only applicable to relatively small systems.

In the 60's, Hohenberg and Kohn presented a new method for solving the Schrödinger equation: The Density Functional Theory, which has grown in applicability in recent years.

1.2.2.1 *Hohenberg and Kohn theorems*

Hohenberg and Kohn[25] proved that the external potential V(r) and the total number of electrons N are uniquely determined by the electronic density ρ(r) of the ground state of the system. They also proved that V(r) and N uniquely determine ρ(r), as well as the Hamiltonian. Therefore, all properties of a physical system can be calculated if ρ(r) is known. Another result of their work is that there is a universal functional that allows calculation of the energy of a quantum mechanical system from this electronic density. For a given potential V(r) the energy of the fundamental state is written as:

Eq. 38
$$E[\rho(r)] = \int V(r)\rho(r)dr + F[\rho] = \int V(r)\rho(r)dr + \mathrm{T}[\rho] + V_{ee}[\rho]$$

where E[ρ(r)] is a functional of ρ(r), i.e. a mathematical entity which associates a number (the energy in this case) to a function[26] (in this case ρ(r)).

For a system comprising nuclei and electrons, the external potential, V(r), refers to the Coulombic attraction electron-nuclei and F[ρ] refers to the sum of the kinetic, Coulombic electron-electron and exchange-correlation energies. Hohenberg and Kohn also extended the Variational Principle to this function. This principle states that the energy E[ρ(r)] calculated with a given electronic density ρ(r) is higher than the energy of the real system, E_0. E[ρ(r)] equals E_0 only when ρ(r) is the exact electronic density of the system. Therefore, the minimization of the energy allows the calculation of the electronic density of the ground state of the system, and consequently all its properties. This summarizes the basic principles of Density Functional Theory (DFT). We need now to describe how to use these principles in calculations.

1.2.2.2 *Kohn-Sham method*

In order to facilitate the solution of the system, Kohn and Sham[27] expressed the wave function as a Slater determinant (N independent electrons in N orbitals ϕ_i). For this system the total wave function is:

Eq. 39 $$\Psi_s = \frac{1}{\sqrt{N!}}|\phi_1 ... \phi_N|$$

the electronic density:

Eq. 40 $$\rho(r) = \sum_i^N |\phi_i(r)|^2$$

the kinetic energy:

Eq. 41 $$T_0 = \sum_i^N \langle \phi_i | -\frac{1}{2}\nabla^2 | \phi_i \rangle$$

Therefore the energy can be written as:

Eq. 42

$$\begin{aligned} E[\rho(r)] &= \int V(r)\rho(r)dr + \mathrm{T}[\rho] + V_{ee}[\rho] \\ &= \int V(r)\rho(r)dr + \mathrm{T}_0[\rho] + J[\rho] - (T[\rho] - T_0[\rho] + V_{ee}[\rho] - J[\rho]) \\ &= \int V(r)\rho(r)dr + \mathrm{T}_0[\rho] + J[\rho] + E_{xc}[\rho] \\ &= \sum_i^N \langle \phi_i | -\frac{1}{2}\nabla^2 | \phi_i \rangle + \int V(r)\rho(r)dr + J[\rho] + E_{xc}[\rho] \end{aligned}$$

J[ρ] refers to the classic part of the electron-electron interaction, i.e. the Coulombic repulsion between two electronic density clouds. $E_{xc}[\rho]$ is the exchange-correlation energy, containing all the non-classic electron-electron interactions. We can introduce the definition

of $\rho(r)$ in $E[\rho(r)]$, obtaining a functional of N orbitals. The minimum of the energy hypersurface is found when this functional is stationary for any infinitesimal variation of ϕ_i. It leads to the Kohn-Sham equations:

Eq. 43
$$\left(-\frac{1}{2}\nabla^2 + V_{eff}\right)\phi_i = \varepsilon_i \phi_i ,$$

where

Eq. 44
$$\begin{aligned} V_{eff} &= V(r) + \int \frac{\rho(r')}{|r-r'|} dr' + \frac{\delta E_{xc}(\rho)}{\delta \rho(r)} \\ &= V(r) + V_H(r) + V_{xc}(r) \end{aligned} .$$

$V(r)$ is the external potential generated by the positive charges of the nuclei on the electric cloud. $V_H(r)$ is the potential associated with the classical (Coulombic) part of the electron-electron interactions (named the Hartree potential) and $V_{xc}(r)$ is the exchange-correlation potential, which contains all the non classical parts of the electron-electron interaction.

The minimization of $E[\rho]$ is achieved by the solution of N equations describing the behaviour of N independent electrons in the effective potential given by Eq. 44.

The solution of the equations involves the interaction of the electrons with the calculated electron density. This makes necessary the use of an iterative process, i.e. the Self Consistent Field (SCF), which is illustrated in Figure 1.7.

The molecular orbitals ϕ_i are expressed as linear combinations of basis functions (χ_p), which depend on the system studied.

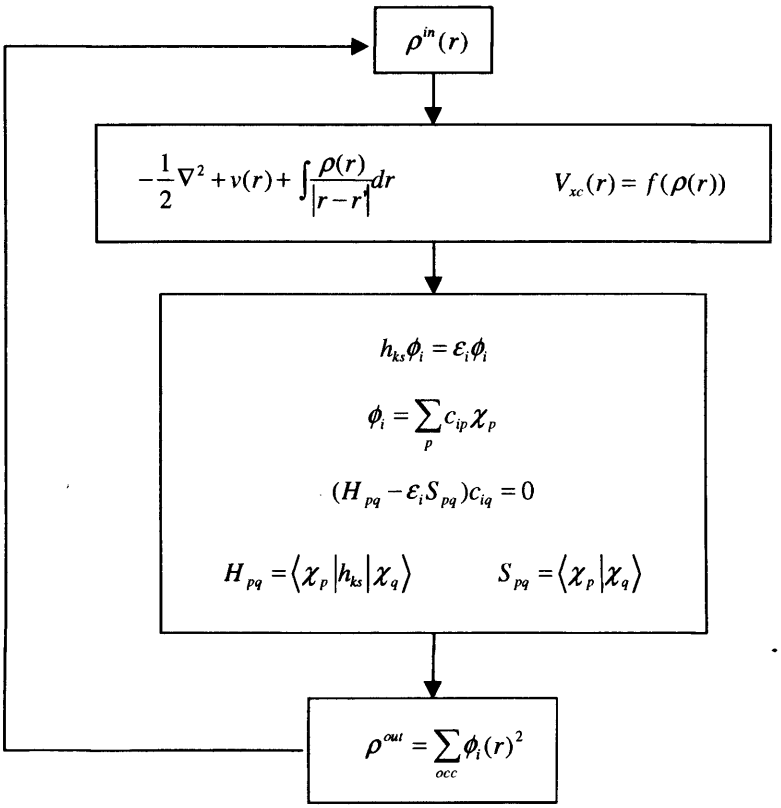

Figure 1.7

SCF iterative process for calculating electronic densities.

Once the stationary solution has been obtained, the energy is given by:

Eq. 45
$$E = \sum_i^N \varepsilon_i - \frac{1}{2}\int \frac{\rho(r)\rho(r')}{|r-r'|}drdr' + E_{xc}(\rho) - \int V_{xc}(r)\rho(r)dr$$

It is worth noticing that the SCF process gives us the energy for a given nuclear configuration, not the minimum energy of the system. The overall energy minimum is still obtained following the scheme presented in Figure 1.5, in which the geometry is optimized.

The power of the Kohn-Sham equations comes from the fact that the effective potential contains formally all the polyelectronic effects. The HF method only takes into account exchange effects. In theory the computer time required by HF and DFT methods scale as N^3, where N is the number of atoms, while post-HF methods scale at least as N^5.

1.2.2.3 *Exchange-correlation functional*

The main drawback of the method is that the functional $E_{xc}[\rho]$, which allows the calculation of the energy, is unknown. As we do not know $E_{xc}[\rho]$, we cannot calculate the electron density and the properties of the system. Therefore it is necessary to find a good approximation of this functional, in order to use the method.

Several conditions are known to be mandatory when building up a new functional, in order to describe properly a physical system (boundary conditions, integrability, etc). The first, and simplest, functional is the local density approximation, LDA:

Eq. 46 $$E_{xc}^{LDA}[\rho] = \int \rho(r)\varepsilon_{xc}[\rho(r)]dr \ ,$$

where $\varepsilon_{xc}[\rho(r)]$ is the exchange-correlation energy for a particle in a uniform electron gas. It can be calculated very accurately[28, 29]. Despite its simplicity, this approximation can yield good results. But LDA functionals have disadvantages: they generally overestimate bond energies and underestimate interatomic distances[30]. The problem with them lies in the fact that they do not take into account variations of electron densities , and in real systems the electron density is not homogeneous. For this reason many functionals have been developed taking into account the electron density gradient[31], $\nabla\rho(r)$. This approach is usually referred to as generalized gradient approximation, GGA:

Eq. 47 $$E_{xc}^{GGA}[\rho] = \int f\left(\rho(r), |\nabla\rho(r)|\right)dr$$

GGA functionals correct many of the failures of the LDA functionals[32].

1.2.2.4 *Energy Minimization: Dmol*^{3}

The Dmol^3 program[33, 34] has been used for our DFT calculations. Although the energy and its derivatives are calculated with a quantum mechanical treatment of the system, the general scheme for obtaining the minimum in the energy hypersurface remains unchanged (Figure 1.5). A complete SCF process is necessary in every energy cycle for calculating the energy and it derivatives. The minimization algorithm implemented in Dmol^3 is a modification of the Newton-Raphson method known as Eigenvector-Following[35].

As noted earlier, the molecular orbitals ϕ_i are expanded in terms of basis functions,χ_p. In Dmol^3 these functions are not analytical expressions (like Gaussian and Slater orbitals) but they are given numerically as values on an atomic-centered spherical-polar mesh, which has several advantages. For example, the molecule can be dissociated exactly into its constituent atoms, and the quality of these orbitals minimizes basis set superposition effects, obtaining a good description even for weak bonds.

We used a double numerical basis set and introduced polarization functions, which are particularly important in obtaining a correct description of the sulphur atom. The Kohn-Sham equations were solved using the gradient corrected exchange-correlation functional from Perdew et al[36, 37].

The integrals in the reciprocal space (over the reciprocal vectors $\vec{k}$) are approximated by a sum over selected k-points in the Brillouin zone. If the simulation cell is large enough, in principle it is possible to use only one k-point to calculate the integrals. Usually the k-point chosen is the origin, i.e. the Γ point. But in our case the simulation cell is large enough only in the z direction. The short lengths used in the x and y directions make necessary the use of more k-points. Convergence of energy in k-point sampling for Brillouin zone integration was checked for each surface, using a Monkhorst-Pack[38] mesh centered on the Γ point. The

converged k-point grids are found to be 5x5x1 for the (110) surface, 5x5x1 for $(11\bar{2}0)$ and 5x7x1 for the $(10\bar{1}0)$ surface.

Two-dimensional periodicity is not implemented in Dmol^3. We thus used the slab approach to model the surfaces with a three dimension periodic supercell. In this approach we cut out a slab containing the desired surface on both faces. This slab is repeated in the two dimensions parallel to the surfaces. In principle there should not be interactions between the surface atoms and any other atom above them, so a large vacuum gap is inserted in the direction perpendicular to the surfaces, so when the unit cell is repeated periodically in the three directions the interaction between two slabs is negligible.

In plane-waves based techniques, the vacuum gap between the slabs is normally limited because the computation time scales not only with the number of atoms, but also with the volume of the simulation cell as a larger volume requires more plane waves. Fortunately, the localized basis set used in Dmol^3 allow the separation between the slabs to be as large as necessary to avoid spurious interaction between slabs. Simulation cells of up to 40 Å in the direction perpendicular to the surface have been used, with the surfaces modelled by 8 layers (32 atoms). The upper four layers are allowed to relax and the bottom four are kept fixed in the optimized bulk geometry.

1.3 Surface energy

We will report a comparative study of a large number of surfaces, requiring the calculation of the surface energy, which is a quantity directly related to the stability of the surface, and is is the energy needed to cleave an infinite crystal to create a surface. For a surface described by the Miller indexes (hkl) it can be defined as follows:

Eq. 48 $$E_S(hkl) = \frac{E_{Total}(hkl) - n \cdot E_{Bulk}}{A(hkl)},$$

where A(hkl) is the surface area of the simulation cell, E_{Total} is the cohesive energy of all the atoms modelling the surface, n is the number of atoms and E_{Bulk} is the cohesive energy per atom in an infinite crystal.

The MARVIN code allows straightforward calculations of the surface energy. The cohesive energy of all the atoms modelling the surface is calculated by subtracting the interaction energy between regions 1 and 2 ($E_{Boundary}$), and the energy of a corresponding region of bulk crystal (E_{Bulk}), from the total energy of region 1 (E_{Total}). The surface energy in this case is:

Eq. 49 $$E_S(hkl) = \frac{E_{\text{Total}}(hkl) - E_{\text{Boundary}}(hkl) - nE_{Bulk}}{A(hkl)},$$

With Dmol[3] we obtain only the total energy of the slab (E_{Total}), so we calculate the surface energy in a different way. First, we calculate the surface energy of the unrelaxed slab:

Eq. 50 $$E_S^{unrelax}(hkl) = \frac{1}{2}\frac{E_{Total}^{unrelax}(hkl) - nE_{Bulk}}{A(hkl)}$$

The factor ½ comes from the presence of two surfaces in the slab. Since we only allow one of these two surfaces to relax, the relaxed surface energy is calculated as:

Eq. 51 $$E_S^{relax}(hkl) = E_S^{unrelax}(hkl) + \frac{E_{relaxation}(hkl)}{A(hkl)}$$

where $E_{relaxation}(hkl) = E_{Total}^{relax}(hkl) - E_{Total}^{unrelax}(hkl)$

We also used three-dimensional repetition of unit cell in the DLPOLY calculations, so the surface energies in this case are calculated with this expression:

Eq. 52 $$E_S(hkl) = \frac{1}{2}\frac{E_{Total}(hkl) - nE_{Bulk}}{A(hkl)}$$

1.4 Crystal morphologies

Having computed the surface energies, the crystal morphology can be obtained through the Gibb's criterion[39], which states that the equilibrium geometry of the crystal should have a minimal total surface energy for a given volume. The equilibrium morphology of the crystal is then that which minimizes the following energy:

Eq. 53 $$E_{STotal} = \sum_{hkl} E_S(hkl)\,A(hkl),$$

which leads to a simple geometrical procedure for calculating the shape of the crystal that minimizes the total surface energy. Each surface (hkl) has a normal vector, $\vec{n}_{hkl}$. It is possible to build a vector $\vec{v}_{hkl}$ for each surface, which is parallel to $\vec{n}_{hkl}$ and whose modulus is the surface energy $E_S(hkl)$. Wulff's theorem[40] states that the shape that minimizes the total surface energy is generated drawing a perpendicular plane at the end of each $\vec{v}_{hkl}$, and taking the volume enclosed by all these planes. The morphology obtained with this method is known as the equilibrium morphology.

The attachment energy, E_{att}, is another useful magnitude in studying surfaces. It is defined as the energy per formula unit released when a new slice of depth d_{hkl} is attached to the crystal surface. We can also use the Wulff construction to obtain the morphology of the crystal that minimizes its attachment energy, to generate growth morphology. In this thesis we wish to characterize the nature of the nuclei in initial stages of crystal growth. The equilibrium morphology has been found to agree better than the growth morphology with experimentally grown small crystallites[41, 42], while the growth morphology is found to agree better with large crystals, since then the crystal is very small, the distances for atomic migration to achieve the equilibrium configuration are negligible, i.e. the crystal is

rearranged instantaneously, so the system will be in equilibrium. Hence only the equilibrium morphology of crystals is studied in this thesis.

1.5 Stabilisation of polar surfaces

As shown by Bertaut[43], if the surface presents a dipole perpendicular to the surface direction, the surface energy will diverge due to the generation of a macroscopic field across the crystal. Considering a crystal as a repetition of planes, Tasker[44] made a classification of the surfaces into three types based on the presence or the absence of such dipoles, as shown in Figure 1.8.

Type I surfaces (Figure 1.8a) are constructed by a repetition of neutral planes and cannot present a dipole moment perpendicular to the surface. Type II surfaces (Figure 1.8b) are constructed by repeating a stack of planes; each stack is charge neutral, but depending on where the crystal is cleaved to expose the surface, the structure may or may not be polar. Type III surfaces (Figure 1.8c) consist of a repetition of charged planes, with no possibility of cleaving the crystal to have a non-polar surface. Polar surfaces are unstable, unless the dipole is removed. Several ways have been reported in the literature to remove this dipole: surface oxidation or reduction[45], electronic transfer across the crystal[46] or geometrical reconstruction. The latter is the one we used, following the method proposed by Harding[47]. This method consists of taking a fraction of the atoms from the top of the surface and moving them to the bottom of the slab that models the surface. By choosing the appropriate fraction of atoms, and their location, the dipole of the slab can be removed.

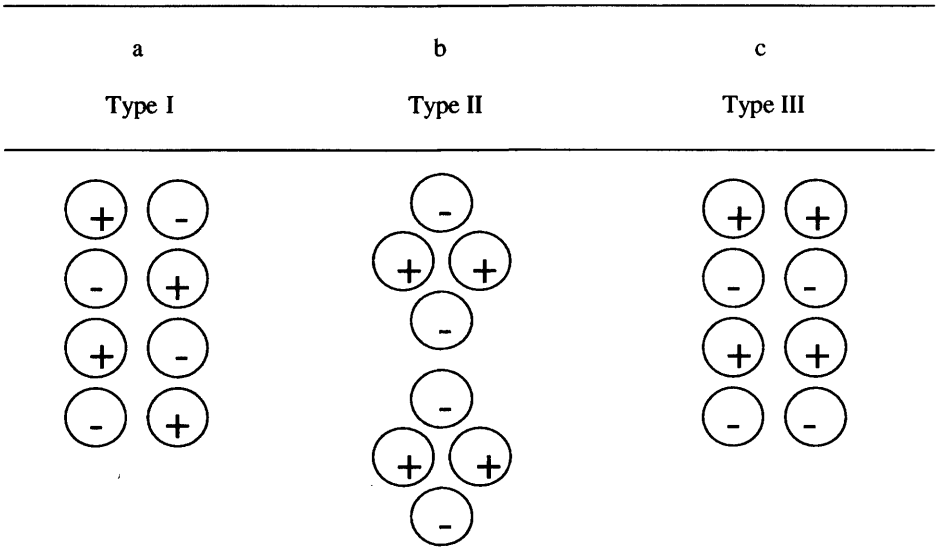

Figure 1.8

Charge arrangements characteristic of the three different types of surfaces. a) Type I surface, consisting in a repetition of neutral planes. b) Type II surface, constructed by a repeating of a neutral stack of planes, each one of which is charged. Depending on where the crystal is cleaved, the surface may be polar or non-polar. In the figure, the crystal is cleaved showing a non-polar surface. c) Type III surface, consisting of a repetition of charged planes that create a dipole, prohibiting cleavage to form a non-polar surface.

1.6 Global minimization techniques

Local minimization techniques are useful when we know that the initial structure of the system is close to the global minimum, which is often not the case, as there are many occasions in which we have little knowledge of the structure of the system, although we do know that it is very likely that the system must have the global energy minimum configuration. In these cases we have to resort to global minimization techniques. There are two main types of global minimization techniques: deterministic and nondeterministic.

Deterministic methods[48, 49] aim unambiguously to generate the global minimum of a potential energy surface; their expense limits their use to very small systems. Nondeterministic methods cannot guarantee finding the global minimum, but they often do so and have the advantage of enabling the study of large systems. We shall now discuss some of these methods.

One of the first global minimum methods proposed was simulated annealing[50] (SA). This method mimics the natural process by which a molten system gradually decreases its potential energy as the temperature decreases, and eventually reaches the global minimum configuration: the most stable crystalline phase. There are two ways of performing SA. The first is to use molecular dynamics, to simulate the time evolution of the system. It is a direct analogy of the physical process of cooling. As shown in Figure 1.9, the first step is to simulate the evolution of the system at very high temperature. At that temperature, the kinetic energy is enough to allow the system to overcome energy barriers between local minima very easily. The temperature is then lowered by a small amount and the evolution of the system is simulated again with molecular dynamics at the new temperature. The fall in temperature permits a lower potential energy configuration to be obtained, and decreases the probability of jumps between local minima. If this annealing process is continued and carried out slowly enough the final structure is likely to be the global minimum structure.

The other way of performing SA is using Monte Carlo sampling, using the Metropolis procedure. In this case, the energy of the initial configuration is computed. The structure is then subject to a random transformation. If the new configuration is more stable than the old one ($E_{new}<E_{old}$) the move is accepted. If $E_{new}>E_{old}$ the move is accepted with a probability $P = \exp\left\{-\frac{E_{new} - E_{old}}{k_B T}\right\}$. By accepting some moves in which the energy increases we avoid the system being trapped in the first local minimum that it finds. This process is repeated many times, with the temperature being gradually lowered from a very high level to the desired value, and the final structure is the global minimum.

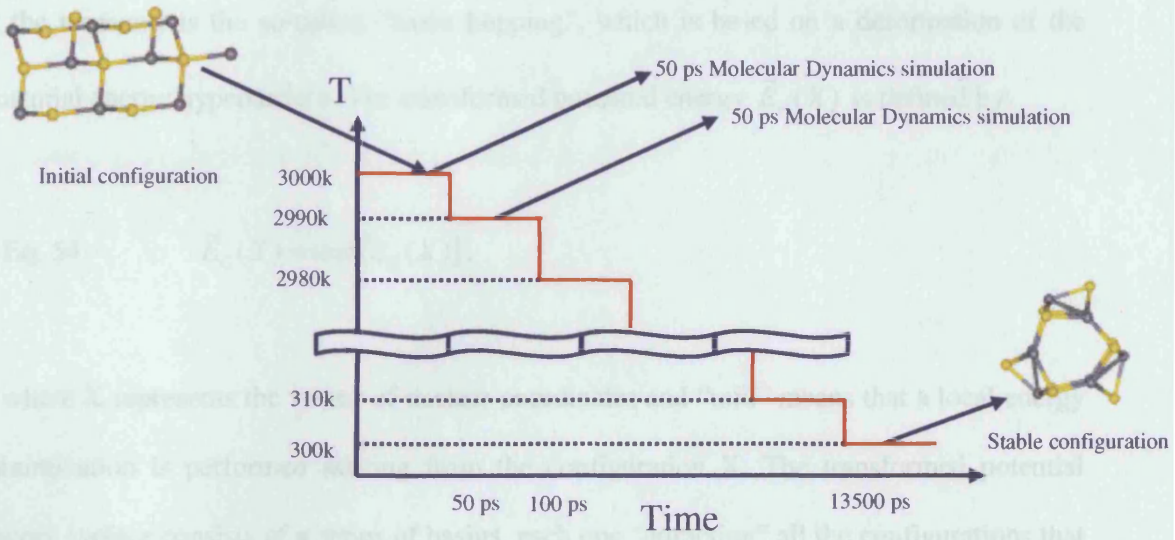

Figure 1.9

Schematic view of the simulated annealing process. The choice of initial configuration shown in the upper left side is not relevant, as the aim of the global minimization techniques is to find the global minimum regardless of the initial configuration. In this example the molecular dynamics simulations are 50ps long and the difference between two consecutive temperatures is 10K.

SA is able to make the system jump between minima while the temperature is high, but at low temperatures such jumps are very improbable; so the system is trapped in a local minimum, which is the main drawback of SA methods. Other methods have been proposed to try to solve this problem.

Evolutionary algorithms are related to another natural process; the evolution of living organisms. Firstly, a "population" of different configurations of the system is created: various operators change these configurations ("mutations") or exchange structural information between them ("crossover"). As a result a new "generation" of configurations has been "born". If this scheme is repeated over many generations, the system will evolve and the global minimum configuration will be reached.

One of the most efficient global minimization methods (and maybe the most fashionable at the moment) is the so-called "basin hopping", which is based on a deformation of the potential energy hypersurface. The transformed potential energy $\tilde{E}_C(X)$ is defined by:

Eq. 54 $$\tilde{E}_C(X) = \min\{E_C(X)\},$$

where X represents the vector of nuclear coordinates and "min" means that a local energy minimization is performed starting from the configuration X. The transformed potential energy surface consists of a series of basins, each one "attracting" all the configurations that are in the same local minimum well. The advantage of doing this is that some transitions are now barrierless and in the others the barriers have been lowered considerably. In Figure 1.10 we can see how transitions between configurations in region A and region B are much easier with the transformed potential energy surface. Any Monte Carlo move that changes the configuration from well A to B is automatically accepted. Moves from B to A are also more probable. As a result, a much broader sampling of the configuration space is achieved, largely improving the efficiency of the Monte Carlo sampling.

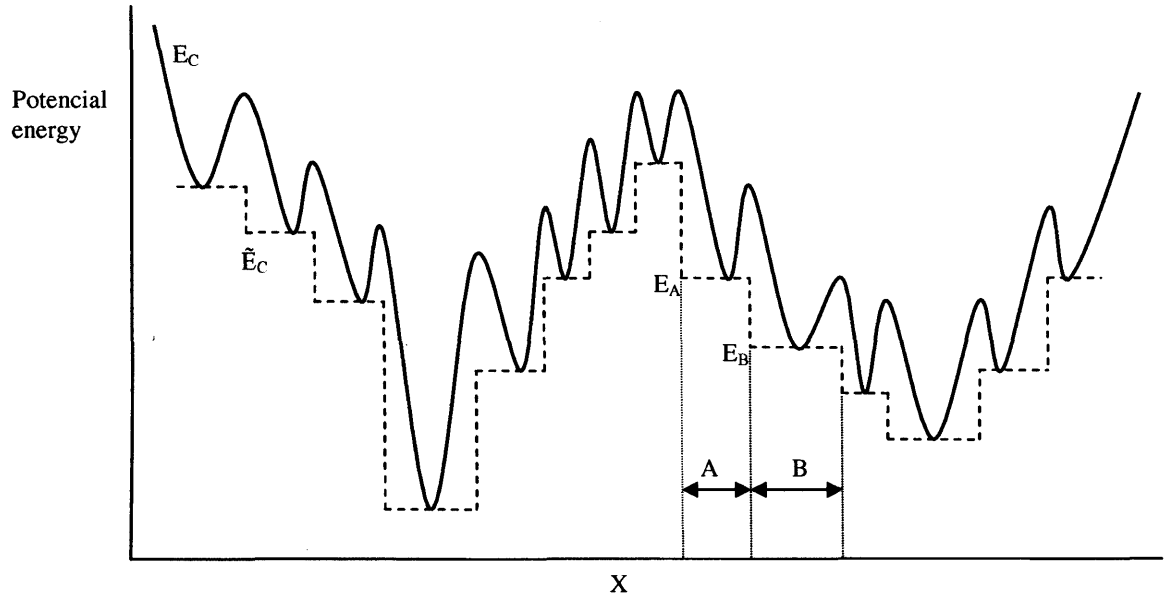

Figure 1.10

Schematic representation of a one-dimensional potential energy hypersurface (E_C) and its transformed hypersurface ($\tilde{E}_C$).

1.7 Classical Nucleation Theory

A very broad definition of nucleation is the process by which a system is transformed from one phase into another. Some physical examples in which nucleation plays a crucial role are condensation of vapours, transformation of a melting system into a crystal structure and transformation of one polymorph into another. Nucleation is a process of major importance in industry[51-53], and in fundamental science, despite which there is little knowledge about the mechanisms involved.

Figure 1.11 shows a schematic example of a liquid that has been undercooled (cooled below its freezing point). The system then undergoes a transformation to obtain a crystalline structure. Small clusters of atoms with crystal-like structure appear in the liquid, which will eventually grow to form the whole crystal structure.

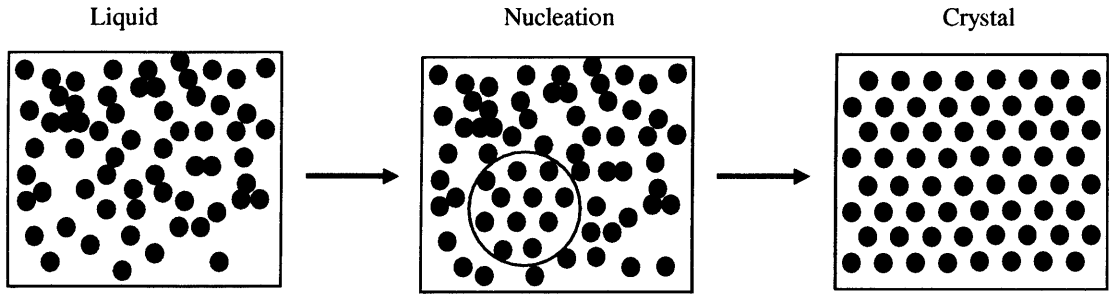

Figure 1.11

Schematic view of a liquid-solid transformation, driven by nucleation events. The nucleus is encircled.

This process occurs when water freezes. Below 0°C the solid, crystalline phase of water (ice) is more stable than the liquid, but the liquid-solid transformation is, of course, not instantaneous. As early as 1724, Fahrenheit reported[54] that water could be cooled to -9.4 °C without freezing. Recently, pure liquid water has been cooled to -40°C, since the nucleation process needs to initiate the phase transformation. The most successful theory of understanding these events is the Classical Nucleation Theory (CNT)[55-57]. Let us consider the case of water freezing to explain the CNT. When liquid water is undercooled (T < 0°C) the molecules continue moving due to their thermal energy. There is a certain probability for a few molecules to arrange in the same way as in the solid phase, therefore forming a "particle of ice" in the liquid water. The first assumption of the CNT is that this "particle", which is the nucleus, is spherical, with radius R. When the nucleus is formed there is a competition between the two energy terms that determine its growth. The first takes into account the fact that the molecules in the nucleus are in a solid phase, which is more stable than the liquid; this term depends on the volume of the nucleus ($\frac{4}{3}\pi R^3$), and can be expressed as:

Eq. 55 $$\Delta G_{bulk}(R) = \frac{4}{3}\pi R^3 \Delta G_{tr} \quad ,$$

where ΔG_{fv} represents the Gibbs free energy of the transition from the old to the new phase per unit volume. Since water in the frozen phase is more stable than in the liquid, this free energy is negative, so if this were the only term affecting the energy of the nucleus, it would be energetically favourable for any nucleus to grow and form a crystal. But, there is an energy penalty that precludes this behaviour: when the nucleus is created, a solid-liquid interface is also created. This interface has an associated positive energy, which depends on the surface area of the nucleus ($4\pi R^2$).

This second term is expressed as:

Eq. 56 $$\Delta G_{surf}(R) = 4\pi R^2 \gamma,$$

where γ is the interfacial free energy per unit area associated with the boundary between the solid nucleus and the surrounding liquid, which is always positive. It is evident that the bigger the cluster, the bigger the positive energy associated with its surface.

The total change in free energy when a nucleus of radius R is formed is therefore:

Eq. 57 $$\Delta G(R) = \frac{4}{3}\pi R^3 \Delta G_{tr} + 4\pi R^2 \gamma.$$

Figure 1.12 shows the typical dependence of $\Delta G(R)$ as a function of the size of the nucleus. When small, the square term is much larger than the cubic term, so the energy of the nucleus is mainly due to the liquid-solid interface. Any increase, would make the nucleus less stable, therefore, small nuclei tend to shrink and disappear. Only when the nucleus reaches a certain size, it is favourable for it to grow. This is the critical nucleus, and the critical radius can be easily calculated from Eq. 57, since it is the radius at which $\Delta G(R)$ goes through a maximum:

Eq. 58 $$R^* = \frac{2\gamma}{\Delta G_{tr}}.$$

The value of $\Delta G(R)$ at that point is the nucleation barrier:

Eq. 59 $$\Delta G^*(R) = \frac{16}{3}\frac{\gamma^3}{(\Delta G_{tr})^2}.$$

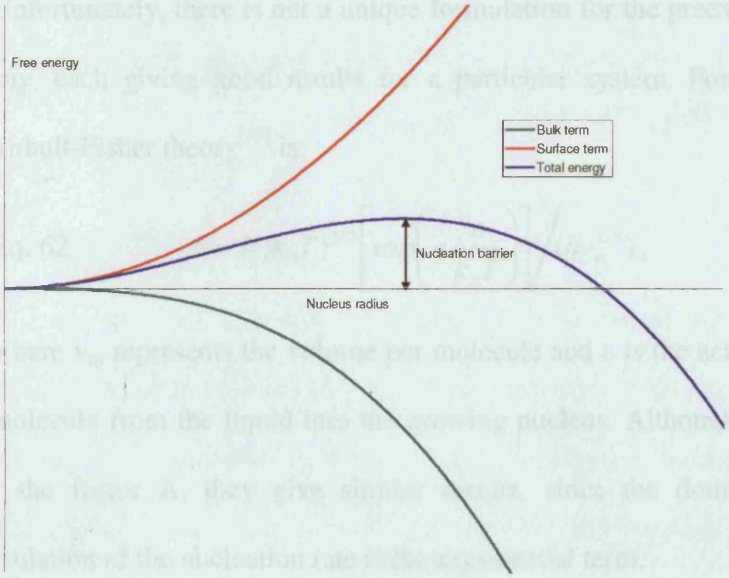

Figure 1.12

Qualitative view of the two energy contributions involved in the nucleation process, which lead to the nucleation barrier.

In order to grow and form a crystal, a nucleus must overcome the nucleation barrier. The standard rate theory gives the probability for the probability for the formation of a crystal nucleus as:

Eq. 60 $$P^* \propto \exp\left(-\frac{\Delta G^*}{k_B T}\right)$$

From Eq. 60, we can deduce one of the main expressions in CNT; the rate of production of critical nuclei of solid per unit volume of a supercooled liquid, which is the probability of creating a critical nucleus times a kinetic factor A that takes into account the rate (J) with which a critical nucleus grows:

Eq. 61 $$J = A\exp\left(-\frac{\Delta G^*}{k_B T}\right)$$

Unfortunately, there is not a unique formulation for the preexponential factor A: there are many, each giving good results for a particular system. For example, the factor in the Turnbull-Fisher theory[55] is:

Eq. 62 $$A = 2(\gamma k_B T)^{1/2}\left[\exp\left(-\frac{\varepsilon}{k_B T}\right)\right]\Big/(h v_m^{2/3}),$$

where v_m represents the volume per molecule and ε is the activation energy for motion of a molecule from the liquid into the growing nucleus. Although there are other expressions for the factor A, they give similar results, since the dominant term involved in the calculation of the nucleation rate is the exponential term.

CHAPTER 2

SURFACE ENERGIES AND CRYSTAL MORPHOLOGY OF ZnS CRYSTALS

2.1 Introduction

The use of computational techniques, in conjunction with thermodynamic principles enables us to obtain information about the properties of the small crystallites that will form after the nucleation has taken place. Many studies concerning theoretical methods, and experimental surface studies of II-VI compounds surfaces have been reported[2-4]. The main findings are that all the surfaces studied, i.e. (110) of the cubic phase and the $(10\bar{1}0)$ and $(11\bar{2}0)$ of the hexagonal phase present the same kind of surface relaxation: anions relax outwards from the surface, while cations relax inwards. Wang and Duke[3] indeed suggested that all the II-VI semiconductor surfaces have similar relaxed geometries.

We model ZnS systems using mainly lattice statics simulations based on interatomic potentials. Zinc sulphide has two polymorphs: the most stable sphalerite (cubic) structure and the high temperature wurtzite (hexagonal) phase. The local structure is the same in both phases with a tetrahedral coordination for both zinc and sulphur. The two phases differ only through the stacking of the atomic planes. Our first requirement is therefore to develop an interatomic potential that can describe accurately both phases. Having developed a satisfactory model, we then proceed with a comprehensive survey of the surfaces exposed in ZnS crystals, allowing us to predict the morphologies of both phases. The results of the calculation employing interatomic potential are compared with those based on Density Functional Theory, and both are compared with available experimental data, revealing a satisfactory measure of agreement.

2.2 Derivation of the new potential

The previously published set of atomistic potentials[58] gives acceptable structural parameters and elastic constants for the cubic phase, but does not describe its vibrational properties adequately. Furthermore, it uses a shell model on the zinc atom with a very low spring constant, which makes it unstable during molecular dynamics simulations. We therefore concluded that a new set of parameters for the description of both phases of zinc sulphide was necessary. In order to achieve that, we undertook parameter fitting with the GULP[59] code using structural parameters[60] and elastic constants[61] for both phases and Γ-point phonons frequencies for sphalerite[62]. Overall, ten experimental values have been used to derive nine parameters. The other experimental values were checked afterwards. We checked that the lattice energy is converged for a cut-off distance 15 Å. This quite high value is needed because of the large C ($1/r^6$) parameter in the S-S Buckingham potential. Table 2.1 shows the comparison between calculated and experimental values for both polymorphs, while the final parameters are compiled in Table 2.2.

The agreement between experimental and computed values is very good, although we note that the parameter fitting was weighted towards reproduction of the cubic structure, as it is the most important polymorph. We also checked that these parameters give reliable geometries for small clusters - $(ZnS)_n$, n = 2-7 - as computed by DFT calculations. This verification has been made by comparing geometries (bond distances within 0.1 Å and bond angles within 5°) obtained from the same starting geometry. This interatomic potential should then be transferable to surfaces and clusters although it is fitted on bulk properties. Checking the transferability of this potential when applied to study surfaces is one of the aims of this study.

This work was carried out in collaboration with Dr. Sylvain Cristol.

	Expt.	IP
Sphalerite		
a (Å)	**5.409**	**5.410**
C_{11} (10^{11} dyne/cm^2)	**10.46**	**10.51**
C_{12} (10^{11} dyne/cm^2)	**6.53**	**6.78**
C_{44} (10^{11}dyne/cm^2)	**4.61**	**4.31**
ε_{stat}	7.9	6.3
ν_1 (cm^{-1})	270	260
ν_2 (cm^{-1})	**350**	**351**
Bulk modulus (Gpa)	78	80
Wurtzite		
a (Å)	**3.85**	**3.87**
c (Å)	**6.29**	**6.10**
z_0	**0.375**	**0.384**
C_{11} (10^{11} dyne/cm^2)	**12.24**	**12.42**
C_{12} (10^{11} dyne/cm^2)	**6.01**	**5.98**
C_{13} (10^{11} dyne/cm^2)	4.554	5.80
C_{33} (10^{11} dyne/cm^2)	14.000	11.30
C_{55} (10^{11} dyne/cm^2)	2.864	3.73

Table 2.1

Comparison of the bulk properties calculated by the new interatomic potential with experimental values. Properties highlighted in bold have been used in the fitting procedure.

	A (eV)	ρ (Å)	B (eV. Å^9)	C (eV. Å^6)
Zn-S	213.20	0.475	664.35	10.54
S-S	11413.09	0.153	0.0	129.18
Spring potential	K (eV. Å^{-2})			
S core - S shell	27.690			
Three-body potential	θ_o (^{o})	K_{TB} eV.rad^{-2}		
Zn core - S shell - S shell	109.47	0.778		
Ion Charges	Charge (e)			
Zn core	2.0			
S core	1.357			
S shell	-3.357			

Table 2.2

Potential parameters used in this study.

2.3 Bare surfaces

In this section we study the bare surfaces. For the sake of clarity we will discuss separately the results obtained with energy minimization techniques (with both quantum and classical approaches) and the results obtained with classical molecular dynamics.

2.3.1 *Literature review of studies on bare surfaces*

Many studies concerning theoretical (mainly tight binding) methods, and experimental bare surfaces studies of II-VI compound semiconductor have been reported[63-65] The main findings are that all the surfaces studied, i.e. (110) of the cubic phase and the $(10\bar{1}0)$ and $(11\bar{2}0)$ of the hexagonal phase present the same kind of surface relaxation: anions relax outwards from the surface, while cations relax inwards. The distance between S and Zn of the first layer in the direction perpendicular to the surface is denoted as $\Delta_{1,\perp}$. Duke and Wang[64] indeed suggested that all the II-VI semiconductor surfaces have similar relaxed geometries. They probed that the magnitude of the $\Delta_{1,\perp}$ displacement is not dependent on chemical properties (like ionicity), but it is dependent on the bulk lattice of the compound. The dependence is linear. These are the formulae that better describe the dependence of $\Delta_{1,\perp}$ with the bulk lattice constant, a_0:

Eq. 63 For surface (110): $\Delta_{1,\perp} = 0.517 + 0.206 a_0$

Eq. 64 For surface $(10\bar{1}0)$: $\Delta_{1,\perp} = 0.178 a_0$

Eq. 65 For surface $(11\bar{2}0)$: $\Delta_{1,\perp} = 0.165 a_0$

However, one of the limitations of these studies is that only non-polar surfaces are studied. In contrast, this chapter considers polar as well as non-polar surfaces using computer

simulation techniques that have already been shown to be very effective in the prediction of solid state and surface properties and that can be extended to nucleation and growth phenomena[66, 67].

2.3.2 *Energy minimization study*

The two programs used for achieving the energy minimizations are MARVIN and Dmol^3. Cubic and hexagonal phases will be treated separately.

2.3.2.1 *Cubic phase*

In order to predict the morphology of a crystal it is necessary to study several surfaces. We have studied all the non-polar surfaces with Miller indexes 0, 1, 2, 3 and 4, and all the polar surfaces with indexes 0, 1 and 2. A general feature is that the higher the Miller index of a surface, the higher its surface area, and consequently the corresponding surface will be less likely to appear in the morphology. Hence, the condition of only showing faces with 0, 1, 2, 3 and 4 Miller indexes is not too restrictive. The (110) surface is the most important in zinc-blende II-VI semiconductors (Figure 2.1).

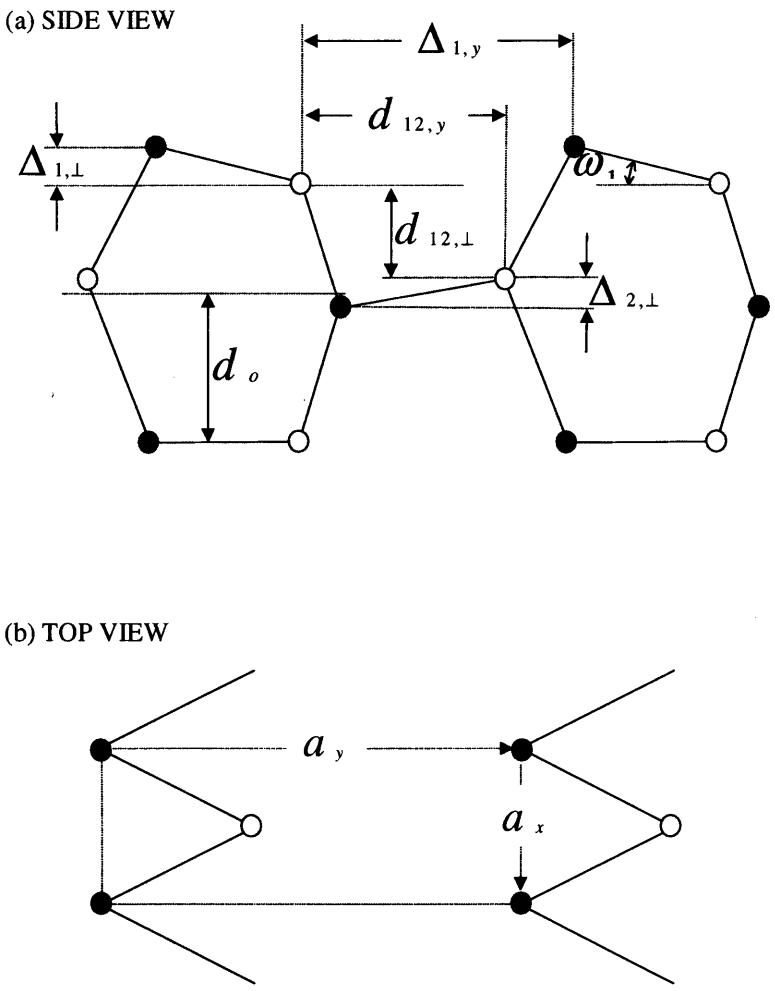

Figure 2.1

Side and top views of the relaxed surface geometry for the (110) surface of cubic ZnS. Full circles denote sulphur atoms, open circles zinc atoms.

We studied this surface using two approaches: lattice statics and DFT calculations. Both give the correct relaxation behavior: anions displace outwards from the surface whilst cations move inwards. As shown in Table 2.3, the distance between S and Zn of the first layer in the direction perpendicular to the surface is 0.35 Å when computed with lattice statics. The DFT result of 0.57 Å is closer to the experimental[68] value of 0.59 Å. In the second layer this perpendicular relaxation between S and Zn has been experimentally[68]

measured as close to zero, while the DFT calculations give 0.12 Å for this distance. In this case, the interatomic potential based result, 0.06 Å, is in better agreement with experiment. Lattice statics results are thus comparable in accuracy with DFT and we have an acceptable agreement with experimental results.

	IP	DFT	Experiments
a_x	3.825	3.868	3.825
a_y	5.410	5.470	5.409
$\Delta_{1,\perp}$	0.354	0.574	0.59
$\Delta_{1,y}$	4.231	4.381	4.296
$d_{12,y}$	2.947	3.120	3.149
$d_{12,\perp}$	1.593	1.443	1.403
$\Delta_{2,\perp}$	0.065	0.119	0.000
d_0	1.913	1.903	1.912
ω_1	16.72°	27.76°	28.0°

Table 2.3

Geometric parameters showing atomic relaxation displacements for the (110) surface of cubic ZnS, as defined in Figure 2.1. All data are in Å except ω_1, which is in degrees. Experimental data are collected from reference 68.

All the other surfaces in the cubic phase have been treated only with lattice statics calculations. Polar surfaces have been reconstructed geometrically by translating some atoms from the top layer to the bottom of the simulation cell in order to quench the surface dipole, as explained in section 2.5. Physically this procedure is equivalent to the creation of surface defects. There is, however, no unique way of creating these defects and various

arrangements of defect have been studied, in order to check which is the most stable reconstruction. We studied this effect on three polar surfaces: (100), (111) and ($\bar{1}\bar{1}\bar{1}$), with three different reconstructions for each. The first type of reconstruction is denoted "point" and is characterized by the largest possible separation between the defects. The goal is to be as close as possible to non-interacting local defects. The second type of reconstruction is denoted "linear", as defects are created following a linear arrangement on the surface. The third type is referred to as "terraced", as all the defects are localized in the same area, forming a terraced surface. Surface energies of the different reconstructions studied are shown in Table 2.4, while Figure 2.2 shows the three kinds of reconstruction. For symmetry reasons, the surface energy for "point" reconstruction does not change with an increase of the simulation cell: a change in the size of the simulation cell does not affect the structure of the surface. The behavior of the "terraced" reconstruction is, in contrast, divergent: an increase of the size of the simulation cell leads to larger terraces, inducing an increase in the surface energy. Linear reconstruction can only be obtained with a 2x2 surface because of the stoichiometry needed for the reconstruction.

The lowest surface energy is always obtained with a "point" reconstruction for which the surface relaxation is small. On the other hand, linear and terraced defect arrangements strongly distort the surfaces, inducing strong geometric relaxation and a high surface energy. The main conclusion is that, as far as geometrical reconstruction is considered, the most stable way of removing a dipole is by creating point defects with the maximum separation on the surface. Such models will therefore be used for all polar surfaces.

Surface				Surface Energy (J/m^2)
1 0 0	S	Point	1x1	1.30
1 0 0	S	Point	2x2	1.30
1 0 0	S	Point	3x3	1.30
1 0 0	S	Linear	2x2	2.02
1 0 0	S	Terraced	2x2	1.49
1 0 0	S	Terraced	3x3	1.68
1 0 0	Zn	Point	1x1	1.12
1 0 0	Zn	Point	2x2	1.12
1 0 0	Zn	Point	3x3	1.12
1 0 0	Zn	Linear	2x2	1.47
1 0 0	Zn	Terraced	2x2	1.16
1 0 0	Zn	Terraced	3x3	1.44
1 1 1	Zn	Point	1x1	0.87
1 1 1	Zn	Point	2x2	0.87
1 1 1	Zn	Point	3x3	0.87
1 1 1	Zn	Linear	2x2	1.41
1 1 1	Zn	Terraced	2x2	1.14
1 1 1	Zn	Terraced	3x3	1.83
$\bar{1}\,\bar{1}\,\bar{1}$	S	Point	1x1	1.01
$\bar{1}\,\bar{1}\,\bar{1}$	S	Point	2x2	1.01
$\bar{1}\,\bar{1}\,\bar{1}$	S	Point	3x3	1.01
$\bar{1}\,\bar{1}\,\bar{1}$	S	Linear	2x2	Does not converge
$\bar{1}\,\bar{1}\,\bar{1}$	S	Terraced	2x2	1.14
$\bar{1}\,\bar{1}\,\bar{1}$	S	Terraced	3x3	1.29

Table 2.4

Relaxed surface energies of differently reconstructed polar surfaces of cubic ZnS: (100) S-terminated, (100) Zn-terminated, (111) Zn-terminated and ($\bar{1}\bar{1}\bar{1}$) S-terminated. The first column in the surface description shows the surface, the second the atom with which it is terminated, the third the kind of reconstruction (see text) and the fourth the number of minimum unit cells contained in our simulation cell.

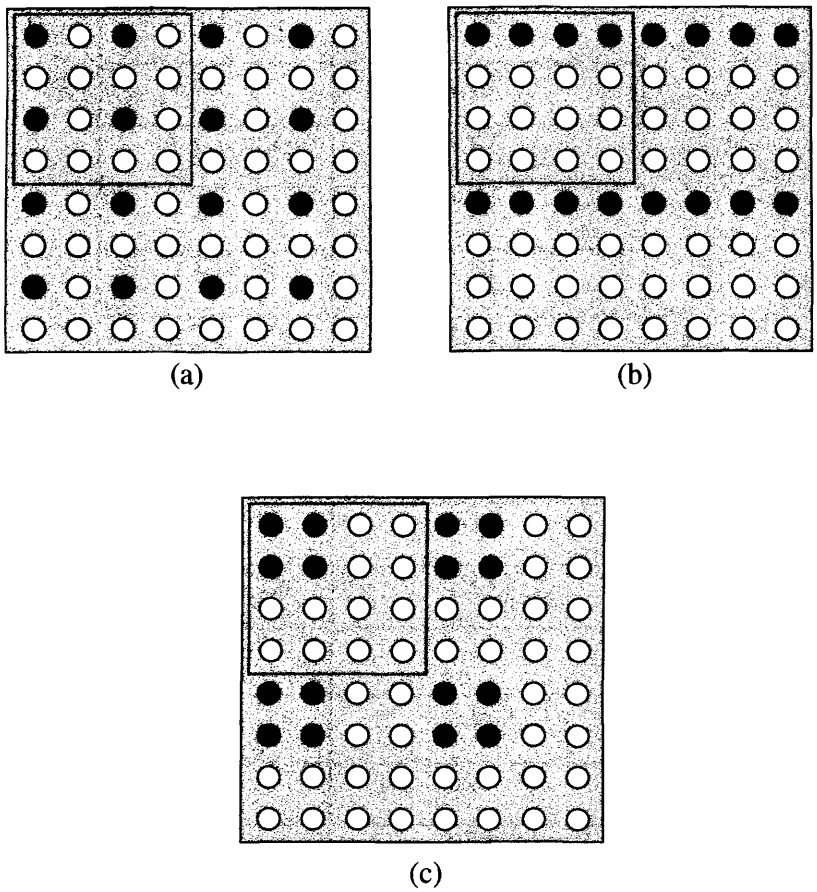

Figure 2.2

Schematic representation of a surface (top view). White circles represent surface atoms, while black atoms represent the vacancies created in order to remove the dipole. The repeated unit cell is surrounded by a dashed square. In this example dipole removal is achieved by translating 1 out of 4 surface atoms. a) "point" reconstruction. b) "linear" reconstruction. c) "terraced" reconstruction -see text.

The surface energies of all the surfaces modelled for the cubic phase ZnS surfaces are summarized in Table 2.5, where results on polar and non-polar surfaces are shown.

Surface	Surface Energy (J/m^2)
1 1 0	0.53
$\bar{4}$ 3 1	0.78
4 3 1	0.84
1 1 1 Zn	0.87
3 2 1	0.95
$\bar{1}\bar{1}\bar{1}$ S	1.01
2 2 1 Zn	1.01
2 2 1 S	1.06
2 1 0 S	1.08
1 0 0 Zn	1.12
2 1 0 Zn	1.14
2 1 $\bar{1}$	1.17
3 2 $\bar{1}$	1.19
3 1 0	1.27
2 1 1	1.28
1 0 0 S	1.30

Table 2.5

Surface energies for polar and non-polar surfaces of cubic ZnS. S and Zn denote the atom with which the polar surface is terminated.

The most stable surface is the (110), with a surface energy of 0.53 J/m^2, in good agreement with the value obtained from DFT calculations, of 0.46 J/m^2. The next most stable surfaces are the non-polar (431) and ($\bar{4}31$), 0.78 J/m^2, and 0.83 J/m^2 respectively, followed by the (111) polar surface, Zn terminated, 0.87 J/m^2. The higher stability of the (110) surface, compared with any other polar or non-polar surfaces, has also been observed experimentally[69, 70] in measurements on thin film layers of ZnS.

It is interesting to note that surface relaxation is not larger on the polar than on the non-polar surfaces. Taking the Zn-S distance as a measure of the relaxation, we found that in the non-relaxed surfaces the value is 2.34 Å, while in the relaxed surfaces it is measured between 2.18 Å and 2.40 Å, for both, polar and non-polar surfaces.

Figure 2.3 shows the predicted crystal morphology according to our calculations. Although many surfaces are taken into account, only the (110) surface is present in the morphology because of its much higher stability; the resulting shape is a dodecahedron, which is very isotropic.

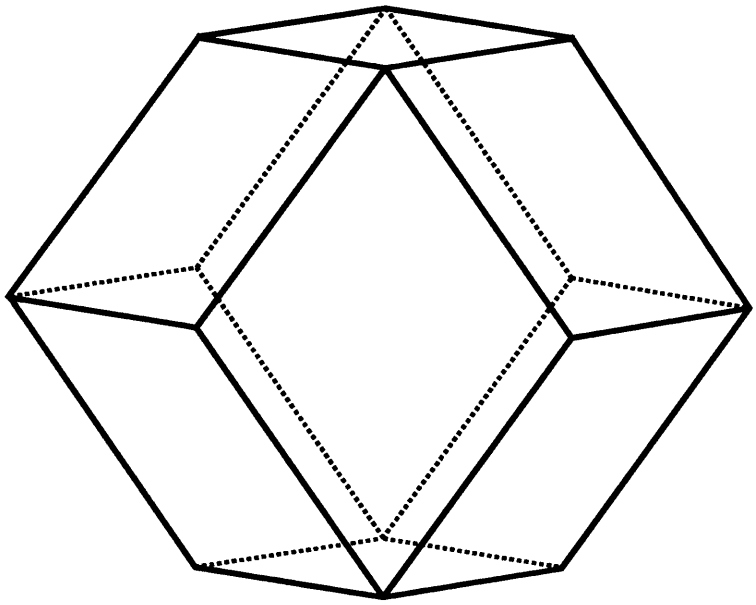

Figure 2.3

Calculated morphology of the cubic phase of ZnS, obtained by using relaxed surface energies. The only surface to appear is the (110).

2.3.2.2 *Hexagonal phase*

The hexagonal phase of ZnS has also been studied with lattice statics and with DFT calculations. Figure 2.4 and Figure 2.5 show the $(10\bar{1}0)$ and the $(11\bar{2}0)$ surfaces respectively, which have been modelled with both techniques.

(a) SIDE VIEW

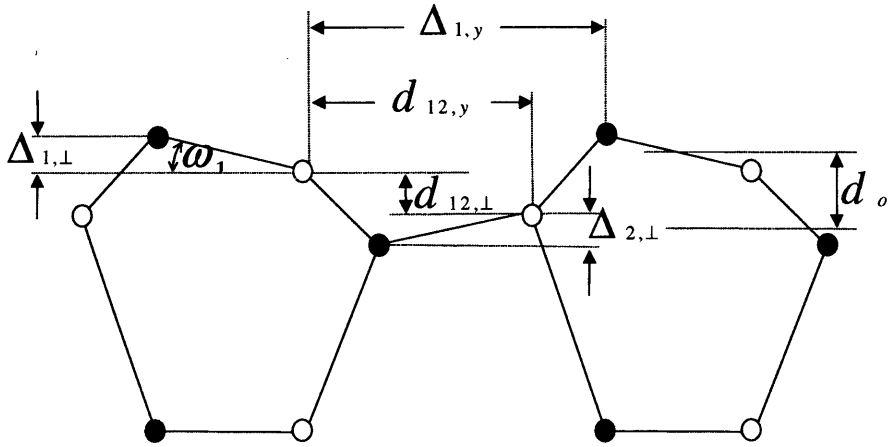

(b) TOP VIEW

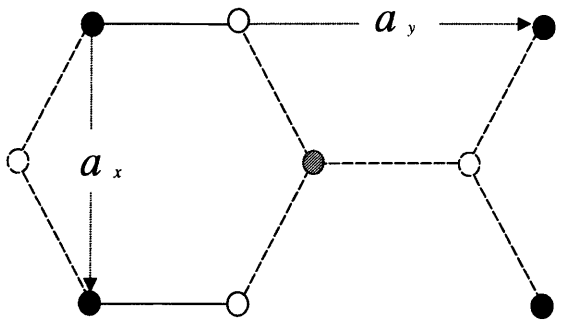

Figure 2.4

Side and top views of the relaxed surface geometry for the $(10\bar{1}0)$ surface of hexagonal ZnS. Full circles denote sulfur atoms, open circles zinc atoms. The top view also shows hatched circles and dashed open circles, representing sulphur and zinc atoms of the second layer, respectively.

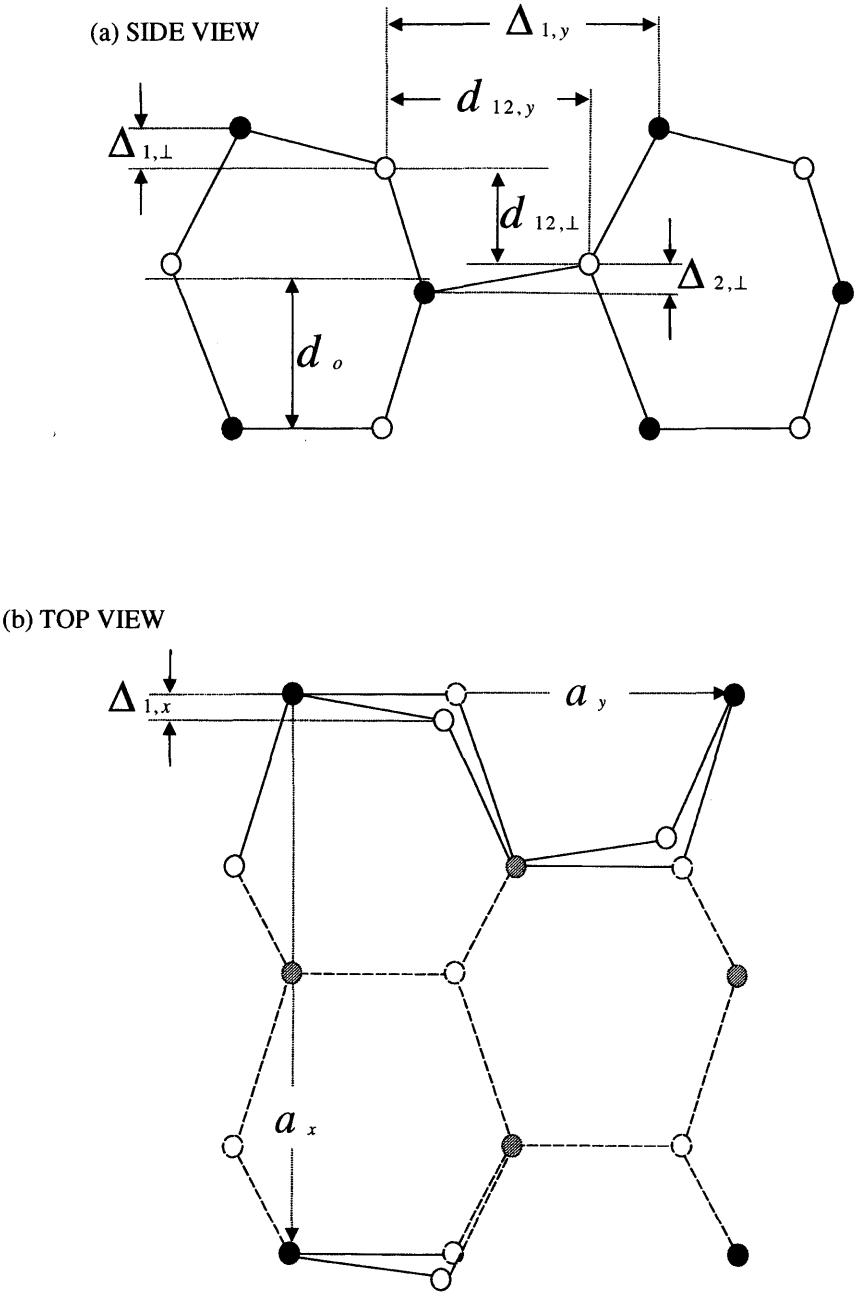

Figure 2.5

Side and top views of the relaxed surface geometry for the $(11\bar{2}0)$ surface of hexagonal ZnS. Full circles denote sulfur atoms, open circles zinc atoms. The top view also shows hatched circles and dashed open circles, representing sulphur and zinc atoms of the second layer, respectively.

There are no experimental results available for these surfaces of ZnS, although they have previously been studied theoretically[71]. These surfaces have also been widely investigated for other II-VI semiconductors[64, 65] (ZnO, CdS, CdSe...) and III-V semiconductors[72] (GaAs, AlP, InSb). Here we also report the first study of the non-polar $(12\bar{3}0)$ surface and two polar surfaces of wurtzite. Relaxed geometries are reported in Table 2.6 and Table 2.7, comparing DFT and interatomic potential based results for $(10\bar{1}0)$ and $(10\bar{2}0)$ surfaces respectively.

	IP	DFT
a_x	3.878	3.871
a_y	6.091	6.332
$\Delta_{1,\perp}$	0.421	0.671
$\Delta_{1,y}$	3.870	4.196
$d_{12,y}$	3.288	3.565
$d_{12,\perp}$	0.711	0.501
$\Delta_{2,\perp}$	0.114	0.120
d_0	1.120	1.100
ω_1	10.8°	17.4°

Table 2.6

Geometric parameters showing atomic relaxation displacements for the $(10\bar{1}0)$ surface of hexagonal ZnS, as defined in Figure 2.4. All data are in Å except ω_1, which is in degrees.

	IP	DFT
a_x	6.717	6.705
a_y	6.091	6.332
$\Delta_{1,\perp}$	0.363	0.566
$\Delta_{1,y}$	4.613	4.384
$d_{12,y}$	3.575	3.704
$d_{12,\perp}$	1.617	1.408
$\Delta_{2,\perp}$	0.065	0.100
d_{O}	1.903	1.955
$\Delta_{1,x}$	0.282	0.425

Table 2.7

Geometric parameters showing atomic relaxation displacements for the $(11\bar{2}0)$ surface of hexagonal ZnS, as defined in Figure 2.5. All data are in Å.

As in the cubic phase, the main characteristic of the relaxed surfaces is the displacement of the sulphur atoms outwards from and of the zinc atoms towards the surface. In the (110) surface of the sphalerite polymorph, the perpendicular relaxation displacement $\Delta_{1,\perp}$ was higher for DFT than for lattice statics results. The same trend is found for $(11\bar{2}0)$ and $(10\bar{1}0)$.

Surface energies of $(11\bar{2}0)$ and $(10\bar{1}0)$ surfaces calculated with the DFT techniques are 0.35 J/m^2 and 0.33 J/m^2 respectively, while lattice statics results are 0.49 J/m^2 and 0.52 J/m^2

respectively. The surface energies calculated with the two methods are therefore different, but both methods predict that the two surfaces have very similar energies.

The good agreement between the calculations (both those using the new set of interatomic potentials and these obtained with DFT) with experiment makes possible the transferability of the potential for ZnS, i.e. it can be used to predict physical properties not only in the bulk but also in the surface of the crystal.

The other surfaces, i.e. the non-polar $(12\bar{3}0)$, and the two polar surfaces (0001) and $(000\bar{1})$, have also been studied with the interatomic potential method. As we found with the polar surfaces in the cubic phase, the most favorable way of removing the dipole of the surface by geometrical reconstruction is the "point" reconstruction. We therefore used this technique for surface reconstruction of the wurtzite phase. Surface energies of all the surfaces studied for the hexagonal ZnS are reported in Table 2.8.

Surface	Surface Energy (J/m^2)
$11\bar{2}0$	0.49
$10\bar{1}0$	0.52
$12\bar{3}0$	0.52
0001 Zn	0.90
$000\bar{1}$ S	0.91

Table 2.8

Surface energies for polar and non-polar surfaces of hexagonal ZnS. S and Zn denote the atom by which the polar surface is terminated.

We find that all of the three non-polar surfaces have almost the same surface energies, which are much lower than the surface energies of the polar surfaces, and that the energies of the (0001) and $(000\bar{1})$ surfaces are very similar. Due to its high surface area, the $(12\bar{3}0)$ surface does not appear in the calculated crystal morphology of hexagonal ZnS (Figure 2.6), even though it has almost the same surface energy as the other two non-polar surfaces. The resulting morphology has a cylindrical like shape, which is highly anisotropic, with a large non-polar area exposing the $(11\bar{2}0)$ and $(10\bar{1}0)$ surfaces, and small areas closing the cylinder exposing the polar (0001) and $(000\bar{1})$ surfaces.

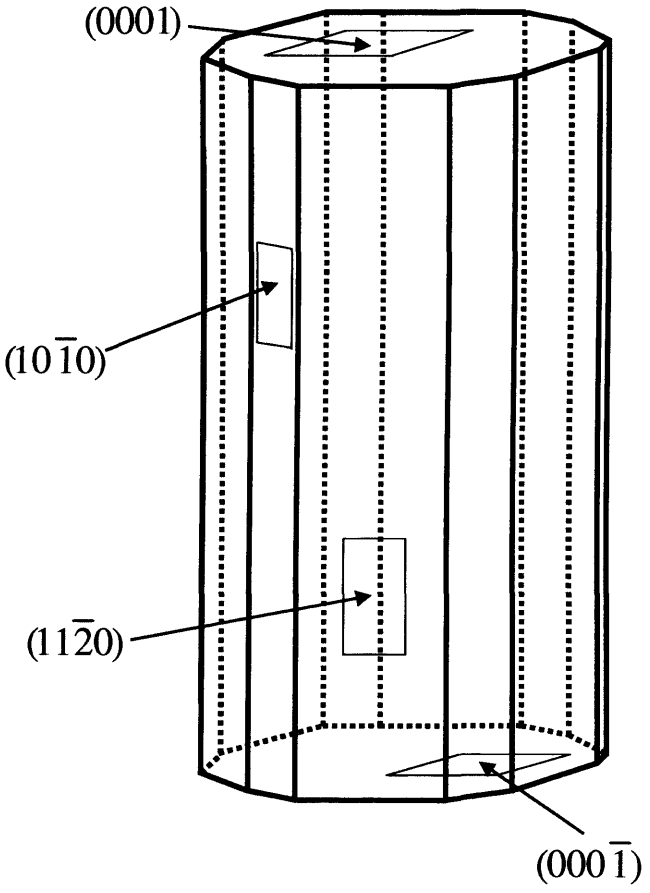

Figure 2.6

Calculated morphology of the hexagonal phase of ZnS, obtained using relaxed surface energies. The indexes of the surfaces exposed are also shown.

2.3.3 *Molecular dynamics study*

The results presented so far in this chapter are based upon lattice statics techniques, in which temperature is not taken into account. In order to assess the influence of temperature, we perform MD simulations of some selected surfaces. The MD simulations are performed with the DLPOLY program (discussed in section 2.1.5), which does not support two dimensional repetition of the unit cell. Therefore, as noted earlier, the slab model was used to model the surfaces. The three most stable surfaces of the cubic phase ((110), (431) and ($\bar{4}31$)) have been studied with MD. There is a problem when surfaces are modeled by three-dimensional repetitions of a slab. The crystal may be cleaved to expose the (110) surface on both sides of the slab. But, due to its geometrical characteristics, it is not possible to build a slab showing the (431) surface on both sides. If the (431) is shown on one side, the other will inevitably show the ($\bar{4}31$) surface. However, in the present case this is not a major problem, because the two surfaces have very similar structures, and their surface energies are almost the same. The surface energy we obtain with the slab calculation will be regarded as an "average" of both surface energies.

The temperature of the calculations is maintained constantly at 300K using the Evans isokinetic ensemble. The timestep is 0.3 fs, and the production time is 100ps, preceded by a 20ps equilibration period.

The molecular dynamics results are very close to those obtained with lattice statics. For example, the (110) surface energy is, surprisingly, exactly the same (0.53 J/m^2). The MD surface energy of the {(431) ($\bar{4}31$)} slab is 0.81 J/m^2. In Table 2.5 we see that the surface energies calculated with lattice statics are 0.78 J/m^2 for ($\bar{4}31$) and 0.84 J/m^2 (431).

Atomic relaxation displacements also show very good agreement. Table 2.9 shows a comparison between values obtained with both methods. Those obtained from molecular dynamics calculations are computed as averages of all the values in the last configuration.

	Lattice statics	Molecular dynamics
a_x	3.825	3.825
a_y	5.410	5.410
$\Delta_{1,\perp}$	0.354	0.369
$\Delta_{1,y}$	4.231	4.296
$d_{12,\perp}$	1.593	1.601
$\Delta_{2,\perp}$	0.065	0.058

Table 2.9

Geometric parameters showing atomic relaxation displacements for the (110) surface of cubic ZnS, as defined in Figure 2.1. All data are in Å.

All these results indicate that the effect of temperature on the bare surfaces is small. The results confirm the reliability of the lattice statics results presented in the previous section. Although a recent MD study on ZnS surfaces[73] suggested that MD simulations give results different to those from lattice statics to model them, our calculations do not show that. The origin of this disagreement might lie in the different set of interatomic potentials used by them. In that article, they do not initially reconstruct the polar surfaces, which might be another reason for the disagreement; because there are thermal barriers that need to be overcome to achieve the self-reconstruction of the surface (necessary to remove the dipole), which might cause the system to be trapped in local minima.

2.4 Hydrated surfaces

In this section we study the hydration of the main surface of sphalerite, the (110) surface. We only study one surface since water is a molecule that can adopt many different positions on the surface, which makes the study much more complicated than in the case of bare surfaces. There were no potential parameters to model the interaction between ZnS and water, so we developed a new potential, which is discussed in section 3.4.2.

2.4.1 *Literature review of studies on hydrated surfaces*

Water adsorption on II-VI compound surfaces has not been studied previously, but extensive studies are reported on other surfaces. For example, Density Functional Theory calculations were performed to investigate water adsorption at CaO(100) and CaF_2(111) surfaces[74]; they found that water molecules are adsorbed by their oxygen atom to surface calcium ions, although there are strong interactions between surface anions and hydrogen atoms, which is the usual way in which water is adsorbed on most ionic surfaces.

Since neither experimental nor theoretical studies are available for water adsorption on II-VI compound surfaces we cannot compare our results with any other previously published. However it is valuable to see what kinds of calculations have been done on other materials. Atomistic simulations were performed to model the effect of water on the surface structure and stability of forsterite[75], finding a very good agreement between experimental and calculated morphologies. Atomistic modeling of water adsorption on hematite has been found to agree well with ab initio calculations with only slight differences in the hydrogen bonding motif[76]. The most studied surface is probably MgO(100), on which water adsorption has been investigated with several experimental techniques, including low energy electron diffraction[77], and temperature programmed desorption[78]. Water adsorption has

also been investigated on three-, four- and five-coordinated surface sites of magnesium oxide[79]. Results suggest that intermolecular interactions between the physisorbed water molecules stabilise or destabilise the adsorbed layer, depending on geometry. But the electrostatic interactions between the surface Mg cation and water oxygen anion are strong enough to be the most important factor in the adsorption process. The authors also found that physisorption of water is energetically preferred at surfaces containing low-coordinated rather than the five-coordinated sites.

Many molecular dynamics studies of water adsorption on ionic surfaces have been reported. For example, molecular dynamics calculations were successfully used to study crystal dissolution from calcite steps[80]. Marmier et al[81] studied the structure of water layers adsorbed on MgO(100), using MD. Their results agree very well with TPD, LEED and FTIR data, showing that water forms a very stable, planar monolayer on the surface, with weak hydrogen bonds between molecules. MgO(100) and MgO(310) surfaces were studied by de Leeuw and Parker[82]. They also obtained the water monolayer for MgO(100), partially hydrated with a 75% coverage. This monolayer was found to disrupt ordering in the next layers, leading to a low water density zone at 10Å above the surface. As in the atomistic static calculations, they observed that water adsorption is more favorable in the low-coordinated surface MgO(310) rather than in the five-coordinated MgO(100).

2.4.2 *ZnS – water potential parameters derivation*

In order to derive a potential model for water interacting with ZnS, we computed the adsorption energy of water molecules on different ZnS clusters using the density functional theory scheme implemented in the $Dmol^3$ code, discussed in section 2.2.4. We used a double numerical basis set and polarisation functions, which were introduced to account for sulphur polarisability. The Kohn-Sham equations are solved using the gradient-corrected functional of Perdew et al[36, 37]. The geometry of the ZnS clusters as well as the ones of the complex (cluster + water molecules) were fully relaxed and the interaction energy (E_{int}) is defined as the energy of the complex minus the energy of the free molecules.

In order to obtain reliable and transferable parameters, we selected the clusters with different Zn coordinations, as presented in Figure 2.7. Two different binding modes were found possible depending on the charge of the initial cluster. Negatively charged clusters (ZnS_2^{2-}) bind water through hydrogen bonding between the sulphur atom and the hydrogen atom of the water molecule, although this adsorption mode is found to be unstable for neutral clusters; on the latter, water binds through an interaction between the zinc atom and the oxygen atom of the molecule. Once these interaction energies and geometries have been computed, we then fitted the potential parameters describing the interaction between ZnS and water, using the GULP[59] code. We used the interatomic potential for ZnS that we developed in chapter 2, and the well established CVFF water model[83] . The interaction of the water molecules and the ZnS clusters was modelled using two Buckingam potentials (Zn-O and S-O). A Lennard-Jones potential with a small A (repulsive) term and a zero B (attractive) term was included between the hydrogen atom of the water molecules and the sulphur atom; it does not, however, significantly influence the computed energies. It has been introduced to improve the stability of the MD simulations by avoiding excessively close approaches hydrogen to the sulphur atoms. The parameters summarized in Table 2.10

are the best compromise we found between a good reproduction of the interaction energies and reproducing the correct Zn-O and H-S distances in the complexes.

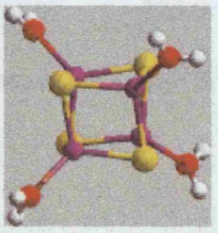

Eint = 2.7 eV (DFT)

Eint = 2.5 eV (IP)

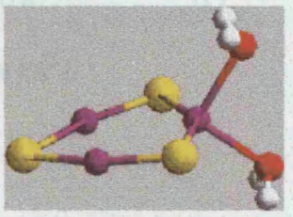

Eint = 1.1 eV (DFT)

Eint = 1.0 eV (IP)

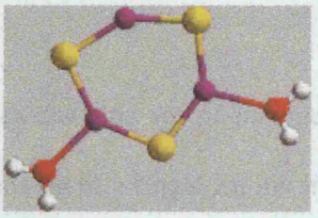

Eint = 1.0 eV (DFT)

Eint = 1.2 eV (IP)

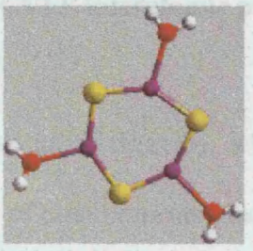

Eint = 1.5 eV (DFT)

Eint = 1.8 eV (IP)

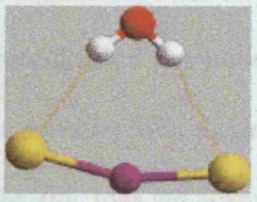

Eint = 1.1 eV (DFT)

Eint = 0.9 eV (IP)

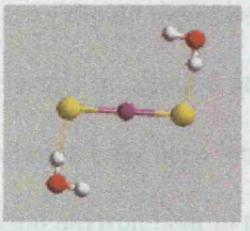

Eint = 2.09 eV (DFT)

Eint = 1.80 eV (IP)

Figure 2.7

Geometry of hydrated ZnS used for potential derivation with the computed DFT energies as well as the interaction energies obtained with the interatomic potential (IP) derived.

Buckingham	*A(eV)*	*ρ(Å)*	*C(eVÅ^6)*
$S - O_w$	123571.0	0.25	0.0
$Zn - O_w$	125.0	0.4	0.1
Lennard-Jones	***A(eVÅ^{12})***	***B(eVÅ^6)***	
$S - H_w$	3.5	0.0	

Table 2.10

Values of the parameters fitted to model the interaction between ZnS and water molecules. Water-water interaction is modelled using CVFF interatomic potenrials.

We emphasize that this set of parameters allows us to describe, with acceptable accuracy, the coordination of a single Zn ion in a variety of environments, namely with two sulphurs bound to water molecules, with two sulphurs and one water molecule, with two sulphurs and two water molecules, and with three sulphurs and one water molecule. The results obtained in MD simulations with this set of parameters should therefore be reliable as most of the possible coordination possibilities for ZnS clusters in solution are represented. No data concerning the solvation of a single Zn^{2+}ion in solution have been introduced in the fitting procedure and the zinc ions are always in a tetrahedral environment in the clusters we studied. It will be seen in the next section however, that the correct octahedral coordination is obtained for Zn^{2+} in water with a distance of 2.07 Å between the ion and the water molecules in good agreement with available experimental data[84]. The interatomic potential we have developed is thus versatile enough to accommodate different coordination spheres around the Zn^{2+} ion.

2.4.3 *Energy minimization and MD studies of hydration*

Lattice statics is the main technique used in this hydration study. We will study the effect of water on crystal morphologies. At the end of this section we present the results of a molecular dynamics study to model water adsorption with a large number of water molecules, including bulk liquid of water far away from the surface. With lattice statics it is more appropriate to study only a water monolayer, for two main reasons: first, a static model of more than one monolayer would model the interface between the ZnS crystal and ice, rather than liquid water; second, we would like to provide results that are comparable with future experiments. Most of the experimental techniques employed in surfaces studies deal with ultra-high vacuum conditions dosed with gaseous water. For example it could be possible to compare our hydration energies with temperature programmed desorption experiments.

The influence of the hydration coverage has been studied by performing many geometry optimizations, in order to find the most stable configuration. The simulation box consists of 2x2 unit cells.

Three quantities have been used to characterize the adsorption of water. The energetic aspects of the interaction of the water molecules with the surface are analyzed by the hydration and dehydration energies. The process in which one out of n water molecules is desorbed from the surface and taken to a gas phase is described by this equation:

Eq. 66 $$\{ZnS\}\{nH_2O\} \leftrightarrow \{ZnS\}\{(n-1)H_2O\} + H_2O_{(g)}$$

We thus define the dehydration energy as:

Eq. 67 $$\Delta E_{dehydration} = \left(E_{\{ZnS\}\{(n-1)H_2O\}} + E_{H_2O_{(g)}}\right) - E_{\{ZnS\}\{nH_2O\}}$$

Another useful quantity is the hydration energy, which is defined it as the energy released when n water molecules in gas phase are attached to the surface.

Eq. 68 $$\Delta E_{hydration} = E_{\{ZnS\}\{nH_2O\}} - E_{\{ZnS\}} - nE_{H_2O_{(g)}}$$

The calculated values of these two quantities are shown in Figure 2.8, which clearly demonstrates that water has a stabilizing effect. The hydration energy is linear with coverage, so all the water molecules have the same effect in terms of the stabilization of the surface. This can also be seen from the dehydration energy, which remains constant for each added water molecule. The main component of the interaction energy between water and surface comes from the electrostatic attraction between its oxygen atom and the zinc in the surface, as in the other systems discussed in the literature review. There are also interactions between the hydrogen atoms of water with the sulphur anions in the surface.

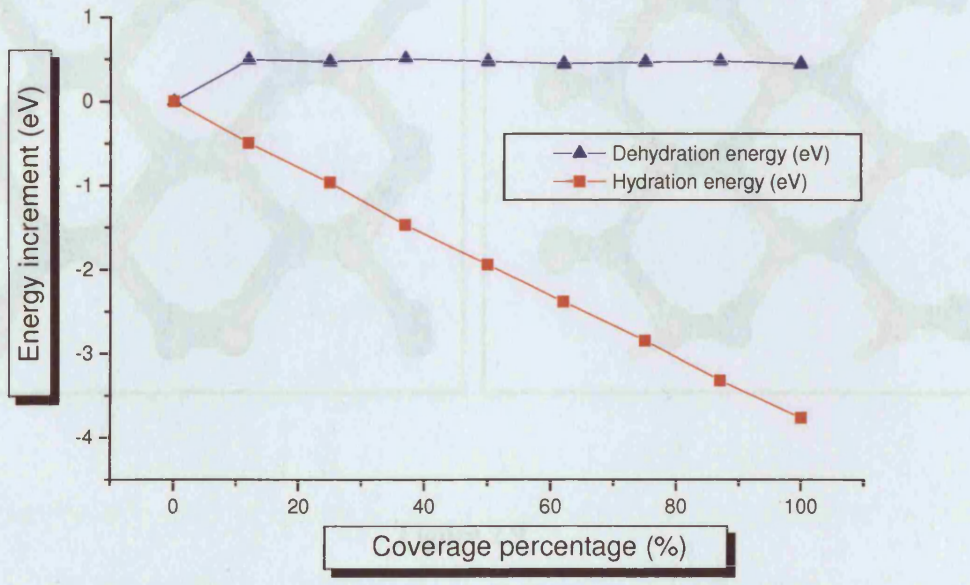

Figure 2.8

Hydration and dehydration energies of the (110) surface.

Figure 2.9 shows two views of the (110) surface, hydrated with a full monolayer. The distance between the two water molecules is around 3.8 Å, which makes the interaction between the water molecules very weak. All the Zn atoms of the surface are equivalent, and the water molecules do not interact strongly with each other, so we can readily understand why the stabilization of the surface is essentially independent of coverage.

(a) Side view (b) Top view

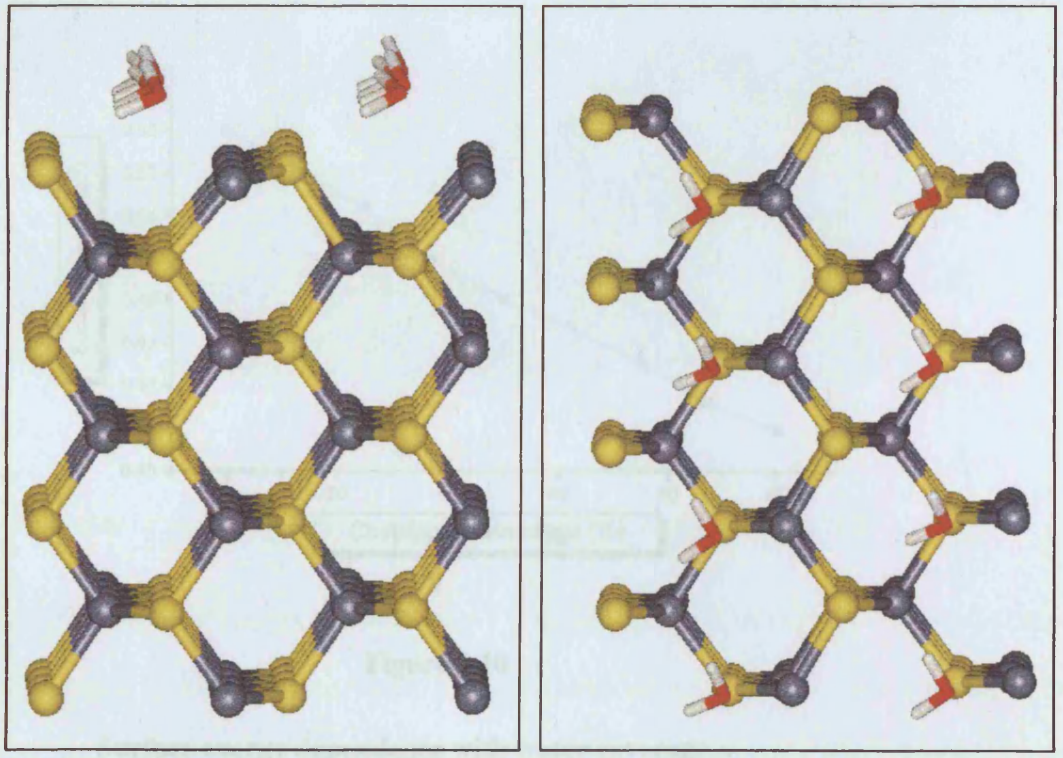

Figure 2.9

Top and side views of the (110) surface, hydrated with a full monolayer of water. Water molecules are shown as cylinders. Zn atoms are darker than S atoms.

The surface energy also provides useful information about the hydration process. We calculate the surface energy of a hydrated surface with the following formula:

Eq. 69 $$E_S(hkl) = \frac{E_{hyd}(hkl) - (E_{Bulk} + nE_{H_2O})}{A(hkl)}$$

where $E_{hyd}(hkl)$ refers to the energy of the hydrated surface, E_{Bulk} refers to the energy of the same number of atoms in the crystal bulk, A(hkl) is the surface area, n is the number of water molecules hydrating the surface and E_{H_2O} is the energy of a water molecule in the bulk of liquid water. Figure 2.10 shows how the surface energy varies with the water coverage.

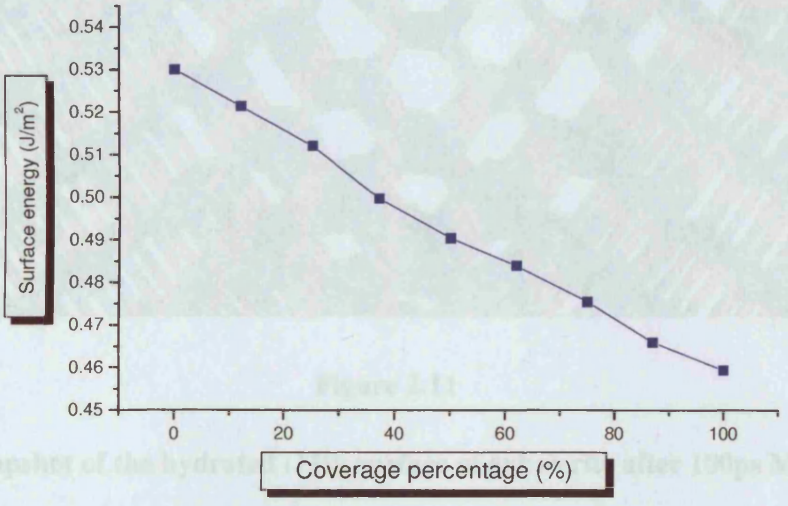

Figure 2.10

Surface energy dependence with water coverage.

The stabilization effect of hydration can be observed through the decrease of the surface energy with water coverage, but the effect is small. The total stabilization of the surface energy by the hydration process is only 0.07 J/m^2, so we cannot expect that the full monolayer is the most stable way of hydrating the surface.

This is observed in MD simulations, which show that the actual coverage at T=300K of the surface is between 0.4 and 0.5. The explanation could be that the thermal motion of the

water molecules induces the water molecules to be more separated. The interaction between the water molecules and the ZnS surface is weaker than the interaction between the water molecules, as can be seen in Figure 2.11.

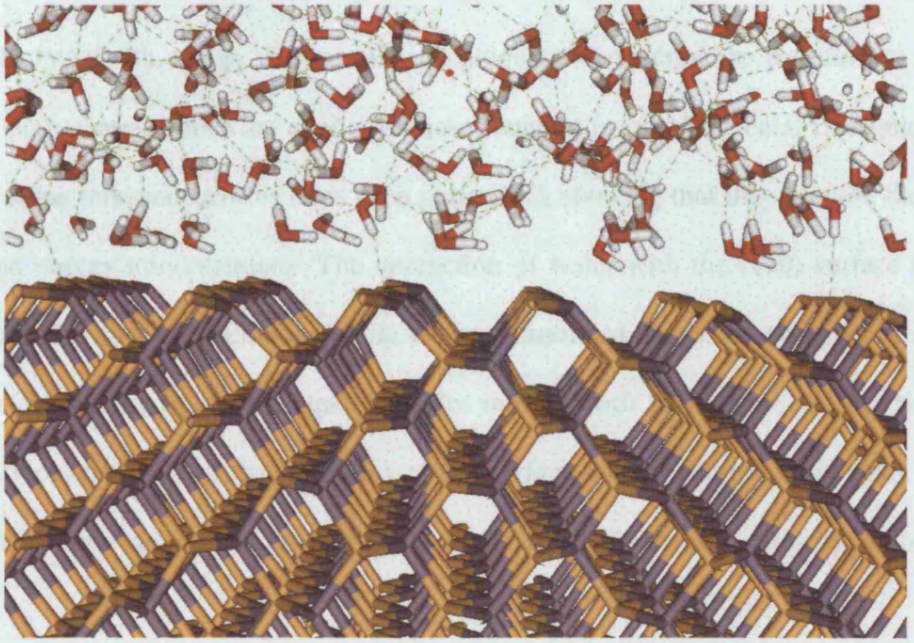

Figure 2.11

Snapshot of the hydrated (110) surface of sphalerite after 100ps MD

All these results suggest that ZnS is not a highly hydrophilic system, so the nucleation from solution will be very fast, since Zn and S atoms prefer to interact between themselves rather than with the water, thus forming quickly ZnS clusters. This is in agreement with experiment. These facts will be further discussed in chapter 5, in which we study the formation of ZnS from an aqueous solution.

2.5 Summary

In this chapter we have carried out a study of the surfaces of both ZnS phases. A new interatomic potential has been fitted to reproduce bulk properties. Its transferability to study surfaces has been tested, finding that it gives acceptable results. From the surface energies calculated with energy minimization techniques we obtained the equilibrium morphologies of both phases, which are similar to those found in nature. Molecular Dynamics simulations of some relevant surfaces have been performed, showing that they provide the same results than energy minimizations. The interaction of water with the (110) surface has also been studied with both methods. While energy minimization techniques predict a decrease in surface energy as more water molecules interact with the surface, in MD simulations we only observe half of the Zn atoms of the surface being hydrated. This study suggests that MD is more appropriate than energy minimization techniques to study hydration of surfaces.

CHAPTER 3

MINIMUM ENERGY STRUCTURES OF $(ZnS)_n$: CLUSTERS IN VACUUM, n=10-47,60

3.1 Introduction

In the previous chapter we obtained information about ZnS systems relating to bulk crystal and surface properties. The use of thermodynamics principles would allow us to use such calculations to predict the structure of microcrystals, which would, however, be considerably larger than the nuclei in which we are interested. In the rest of this thesis we carry out the second of the two-pronged approach mentioned in the Introduction, i.e. the study of clusters smaller than the nuclei. We aim to gain an understanding of the structures and properties of such clusters; and by undertaking calculations as a function of cluster size, we are able to infer the trends followed during the process of cluster formation and nucleation.

Several studies have been devoted to the understanding of the structure and properties of semiconductor nanoclusters, but no clear consensus has emerged as to the structures of the most stable clusters. Since the discovery of fullerenes[85] and carbon nanotubes[86], the exploration of the chemistry of nanoclusters with different chemical compositions has expanded rapidly; in particular several studies have focused on the search for non-carbon nanotubes[87] and fullerene-like structures[88]. Boron nitride is one of the most widely investigated systems, since, owing to the similarity between B-N bonds and C-C bonds, BN can assume almost all the structures adopted by carbon: both diamond-like and graphite-like structures as well as BN nanotubes can be routinely synthesized[87, 89]. Fullerene-like BN cages have also been studied experimentally, revealing that they form onion structures, in which a small cage in the centre in usually surrounded by three or more other cages[90], or

isolated hollow cages as in the case of $B_{24}N_{24}$[91] and $B_{28}N_{28}$[92]. These fullerene-like structures show a B/N stoichiometry of ~1; they are thought to be formed by an arrangement of hexagons and squares.

Small $(ZnS)_n$ clusters, with n=1-9, have been previously studied[93], using DFT methods, which found that there are no four-coordinated atoms in these clusters, all atoms are three-coordinated. The strain introduced in the structure by the formation of those four-coordinated exceeds the gain in energy obtained by the increase of the coordination number. In this chapter we develop a more comprehensive study by simulating the structures of larger $(ZnS)_n$ clusters, n=10-47.

3.2 Methodology

To obtain the most stable structures of the clusters we must use one of the global minimization techniques described in section 2.6. Since we had already performed MD simulations of ZnS systems, we choose Simulated Annealing, based on MD simulations. The Simulated Annealing procedure uses interatomic potentials, but *ab initio* calculations have been performed in order to check the reliability of the interatomic potentials in some key cases and to provide more accurate values of the cluster energies.

For every $(ZnS)_n$ cluster a Simulated Annealing procedure is performed in order to attempt to identify the global minimum. The first step in the procedure is to run a 50ps MD simulation at a very high temperature, 3000K (using the DL_POLY code). After that, the system is cooled, running simulations of 50ps every 10K until the temperature is 300K.

As discussed in section 2.6, there is no method of calculating unambiguously the global minimum for systems; all available methods can generate local minima. We tried to minimise the possibility of reaching a local minimum by performing at least three different Simulated Annealing processes for each cluster. In some cases, the final cluster structure is the same regardless of the process, but in others, each Simulated Annealing process gives slightly different geometries. In these cases, we chose the most stable cluster configuration as the closest structure to the global minimum. The high temperature used for the initial steps of the Simulated Annealing has the effect of removing any possible influence that the initial configuration could have on the final structure. Indeed, we found that the same structures were obtained starting from a random arrangement of atoms or from a cluster cut from the bulk crystal.

The final cluster structures obtained with the Simulated Annealing procedure are then optimised employing three different methods. The first is based on interatomic potentials, and is carried out using the GULP code[59] to minimise the energy of the clusters. The

potential parameters were obtained in chapter 1, by careful fitting to reproduce crystal and molecular properties of ZnS.

Two *ab initio* methods were also employed in order to provide more accurate cluster energies. We studied small clusters using hybrid Density Functional Theory calculations, with the B3LYP exchange-correlation functional[25, 95], as implemented in the Gaussian98 code[96]. We used the Stevens, Krauss, Basch and Jasien (SKBJ) valence basis set[97], with 10 core electrons modelled by effective core potentials. An extra d function was added on both Zn and S. This kind of calculation is denoted B3LYP/SKBJ(d). Previous studies on ZnS clusters have proved the reliability of this basis set[93]. For bigger clusters, we also performed pure Density Functional Theory calculations using the DMol^3 code.[33, 34] We used the PW91 exchange-correlation functional,[36, 37] with effective core potentials and a double numerical plus polarisation basis set. We denote this calculation PW91/ecp-dnp.

We checked that the three methods employed provide similar results. The interatomic potential parameters were developed to predict bulk properties, where atoms always form $(ZnS)_3$ rings. Therefore we use the energy per ZnS unit in a $(ZnS)_{3\text{-ring}}$ as the reference energy for the three methods. Figure 3.1 shows the plot of the cluster cohesive energy as a function of the size, where this energy for a $(ZnS)_n$ cluster is defined as:

$$E_{cohesive} = \frac{\left\{ [E(ZnS)_n]_{Cluster} - n\left[\frac{E(ZnS)_{3-ring}}{3}\right]\right\}}{n}$$

It can be observed that the two *ab initio* methods provide remarkably similar results. Since B3LYP/SKBJ(d) are much more time consuming calculations, PW91/ecp-dnp is the method of choice for calculating accurate cluster energies for bigger clusters. It is gratifying that the trend described by the interatomic potential calculations is the same as that calculated with *ab initio* methods. It suggests that they can be used to calculate the relative stability of the clusters with acceptable accuracy.

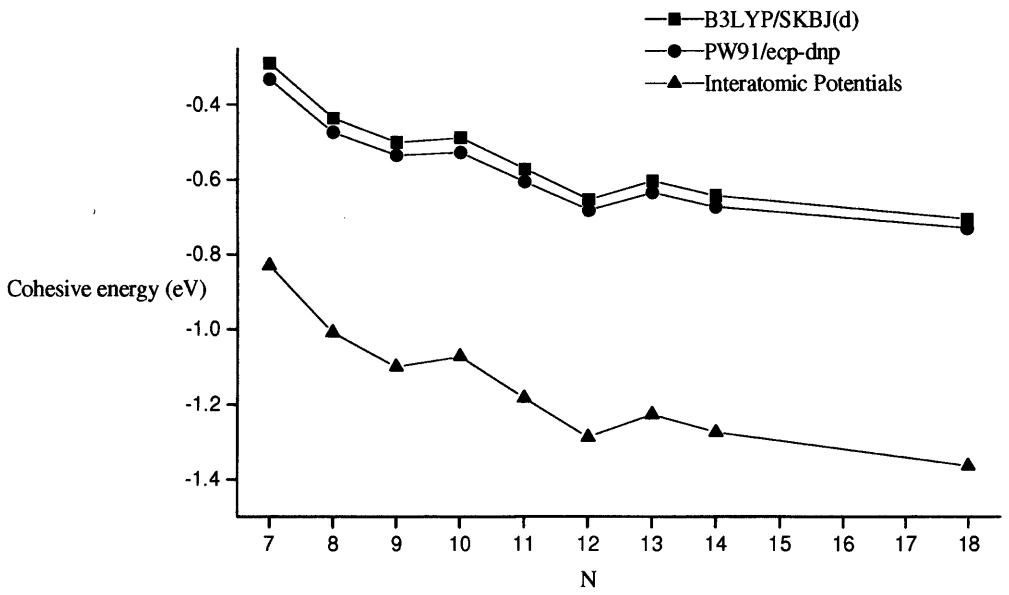

Figure 3.1

Cohesive energies calculated with the three methods used in our study, as a function of the cluster size. Data obtained from hybrid DFT calculations (B3LYP/SKBJ(d)) are represented by solid squares, data obtained from pure DFT calculations (PW91/ecp-dnp) by solid circles and data obtained from interatomic potential calculations by solid triangles. Energies are calculated by performing geometry optimisations (with the three methods) on the cluster structures obtained with Simulated Annealing.

3.3 Bubble clusters and comparison with bulk-like clusters

It has commonly been assumed that large $(ZnS)_n$ clusters (n>20) should have bulk-like structures, with most of the atoms four coordinated. However our studies show that up to n=47, spheroidal clusters with only three coordinated atoms are more stable than the bulk-like ones. We denote these spheroidal open clusters as "bubble clusters". These clusters are formed by the spatial arrangement of 4, 6 and 8 atom rings, where all the atoms are three coordinated. The rings are non-planar distorted polygons; and the bond distances and the bond angles in the same ring are unequal. The number of rings appearing in the lowest energy structure of a $(ZnS)_n$ cluster can be predicted following these two formulae:

Eq. 70 $$N_{6-ring} = n - 4 - N_{8-ring} \qquad N_{4-ring} = 6 + N_{8-ring},$$

which can be deduced from the Euler's Law, which states that for a closed structure formed by polyhedra the number of vertices plus the number of faces will always equal the number of edges plus two. We note that when there are no 8-rings, there must necessarily be six 4-rings.

Our calculations suggest that the presence of 8-rings reduces the stability of the structure. For some clusters we obtained more than one spheroidal structure and the most stable is that with the least number of 8-rings. For example, for $(ZnS)_{13}$ we obtained two local minima with 8-rings (previously reported[98]) but the lowest energy cluster is formed only by 4 and 6-rings. One of the two local minima has one 8-ring and is more stable than the other local minimum, which has two 8-rings. However, we note that in some cases, our simulations did generate structures with octagons. Another characteristic of the stoichiometric bubble clusters is that they cannot contain any odd numbered polygons, which would force Zn-Zn or S-S bonds, leading to high energies. Further calculations are in progress to estimate the energetics associated with non-stoichiometry.

Bulk ZnS occurs in two common polymorphs, zincblende (or sphalerite) and wurtzite. In both structures, the atoms are tetra-coordinated. Zincblende is based on a face-centred cubic array of atoms, whereas wurtzite is derived from a hexagonal close-packed array. In the two structures, the nearest neighbour connections are the same, but the distances and angles to more distant neighbours are different. In order to give added confidence in our results we have cut clusters from the wurzite and zinblende structures and compared the energies of these clusters with the energies of the bubble clusters, as shown in Figure 3.2. We can see that bubble clusters are always more stable than bulk-like clusters. Only one cluster with the zincblende structure is shown, as wurtzite clusters are more stable than those based on zincblende, as the former clusters usually have lower dipole moments than the latter. Both bulk-like clusters have some two coordinated atoms. The relaxation of the structures removes in part the dipole, but some atoms remain two coordinated. On the other hand, in all the spheroidal clusters the total dipole is very small and there are no two coordinated atoms, which will be one factor promoting the stability of these clusters.

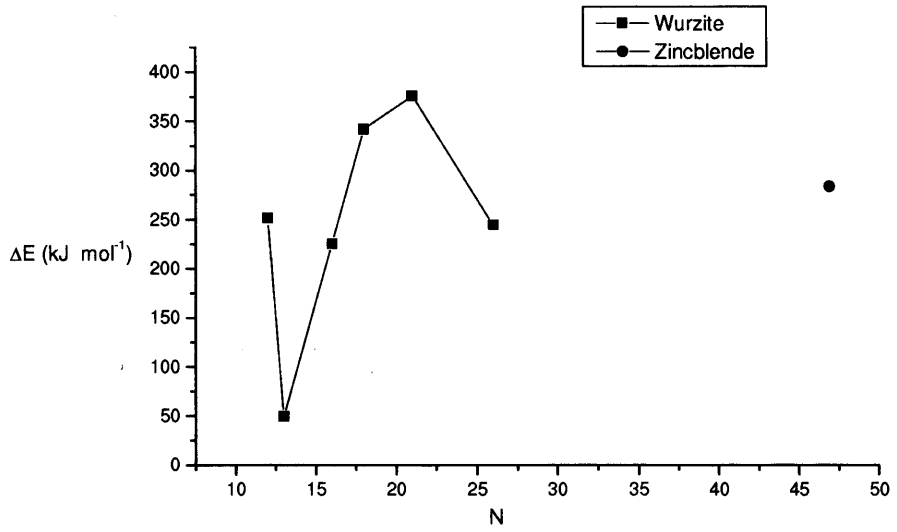

Figure 3.2

Difference between the energies of bulk-like clusters and the energies of bubble clusters, as a function of cluster size. Energies are calculated by performing geometry optimisations of the clusters, with PW91/ecp-dnp level of theory. The zero energy level for each cluster is the energy of the bubble cluster with the same number of ZnS units, calculated with PW91/ecp-dnp as well.

Although atoms in bubble clusters are more stable than in bulk-like clusters, they are less stable than in any of the two bulk polymorphs. We studied the possibility of forming crystals using bubble clusters as building units. Since the $(ZnS)_{12}$ cluster has the structure of a sodalite cage, we repeated it periodically in three dimensions to build a ZnS-based material isomorphous with siliceous sodalite. The resulting crystal is based on the structure of a bubble cluster, but with all the atoms being four coodinated, which would increase its stability. PW91/ecp-dnp calculations show that this is a metastable structure compared to both zincblende and wurtzite polymorphs (the difference in energy is around 25 kJ/mol per ZnS unit). We should also consider another interesting possible bulk structure. Since all the bubble clusters are three coordinated, it would be useful to study the possibility of creating a

bulk material in which all the atoms are three coordinated. With PW91/ecp-dnp calculations we found that a planar graphite-like structure (composed of layers of ZnS hexagons) is a metastable phase, which is 49.4 kJ/mol per ZnS unit less stable than the zincblende phase. All these features suggest that there must be some cluster size above which bubble clusters start being less stable than bulk-like clusters. Global Minimisation techniques applied to bigger clusters than the ones we have studied in this chapter could provide useful information about this transition between bubble and bulk-like structures.

Figure 3.3 and Figure 3.4 show some particularly interesting cluster structures: $(ZnS)_{12}$, $(ZnS)_{18}$, $(ZnS)_{26}$ and $(ZnS)_{47}$. $(ZnS)_{12}$ has six 4-rings and eight 6-rings forming a spheroidal structure with the shape of the beta cage (building units of Sodalite). This cluster is highly symmetric, and is the smaller cluster in which there are no 4-rings sharing edges; 6-rings separate the 4-rings, reducing considerably the structural strain. $(ZnS)_{18}$ is characterised by a tubular structure, and $(ZnS)_{26}$ is an ellipsoid.

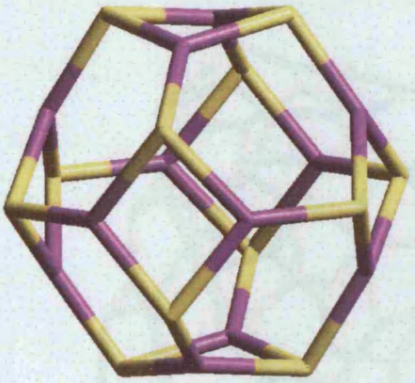

$(ZnS)_{12}$

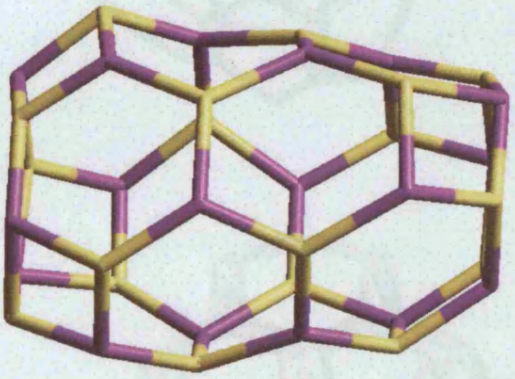

$(ZnS)_{18}$

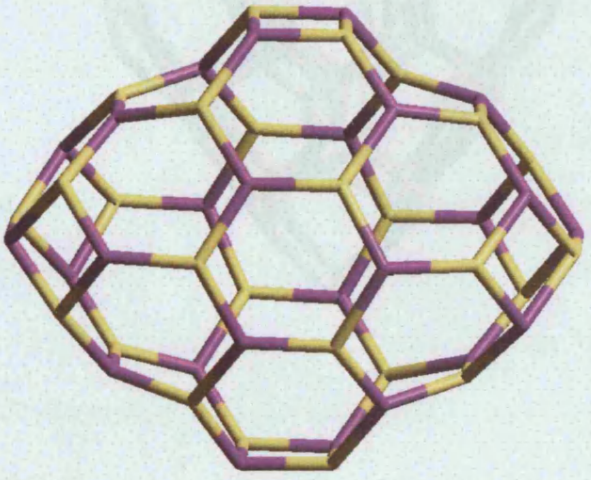

$(ZnS)_{26}$

Figure 3.3

Structures of selected bubble clusters. Yellow sticks refer to Sulphide atoms and blue Grey sticks to Zinc atoms

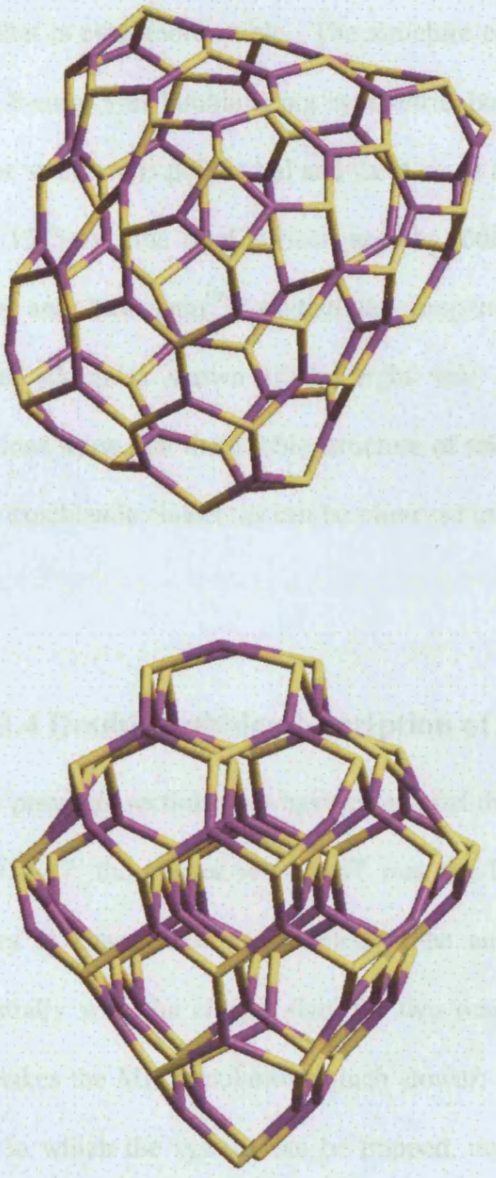

Figure 3.4

Structures of two $(ZnS)_{47}$ clusters. The bubble cluster is on top, and the bulk-like cluster on the bottom. Yellow sticks refer to Sulphide atoms and blue sticks to Zinc atoms.

The $(ZnS)_{47}$ bubble cluster includes a 8-ring, suggesting that it might be possible to find a cluster that is even more stable. The structure consists of seven 4-rings, forty-two 6-rings, and one 8-ring. This bubble is not symmetric, but there is an interesting arrangement of the rings: the structure is polyhedral and the 4-rings make the seven corners. The volume of the cage is 1375 $Å^3$, the total surface area is 1666 $Å^2$ and the radius approximately 15 Å. Gavartin and Stoneham[99] studied the properties of a $(ZnS)_{47}$ cluster with zincblende structure, which is shown if the right side of Figure 3.4. *Ab initio* PW91/ecp-dnp calculations show that the bubble structure of this $(ZnS)_{47}$ cluster is 283 kJ/mol more stable than the zincblende cluster, as can be observed in Figure 3.2.

3.4 Double bubble; description of its geometry

In the previous sections, we have calculated the most stable structures of $(ZnS)_n$ clusters, with n=10-47; the cluster with n=47 was the largest. To investigate larger clusters it is necessary to change our methodology. The amount of computer time needed increases exponentially with the cluster size, for two reasons: firstly because the larger number of atoms makes the MD simulations much slower; and secondly because there are more local minima in which the system can be trapped, necessitating a slower annealing. These two reasons compel us to perform Simulated Annealing of selected clusters, rather than studying all values of n. We continue our study therefore by a detailed investigation of the $(ZnS)_{60}$ cluster.

We use the Simulated Annealing procedure described in section 3.2 to calculate the global minimum structure. The resulting structure is a new type of cluster, which is we shall describe now.

The structure of the $(ZnS)_{60}$ cluster obtained with the Simulated Annealing procedure is shown in the centre of Figure 3.5. To make it clearly visible there is a circle surrounding the inner core of the cluster, a $(ZnS)_{12}$ bubble that is also shown in the right side of the

figure. The left side shows the outer cluster, a $(ZnS)_{48}$ bubble. Neither of these two bubble clusters have octagons: $(ZnS)_{12}$ is formed of 6 squares and 8 hexagons and $(ZnS)_{48}$ is formed of 6 squares and 44 hexagons. The squares of both clusters are placed in the vertices of two octahedra and are very well aligned, so that both octahedra share the same axis, which can be clearly seen in Figure 3.6, where the squares have been highlighted. The diameter of the whole particle is 1.65 nm, and the diameter of the innermost bubble is 0.75 nm.

All these findings accord with the observed behavior of the analogous BN system. High resolution transmission electron microscope (HRTEM) studies[90, 100] have shown that BN forms fullerene-like structures, with a small number of layers (typically ≤ 3). Their stoichiometry B/N is ~1. They are also formed by octahedral cages concentrically arranged, with the smallest inner cage being very often a $(BN)_{12}$ cluster.

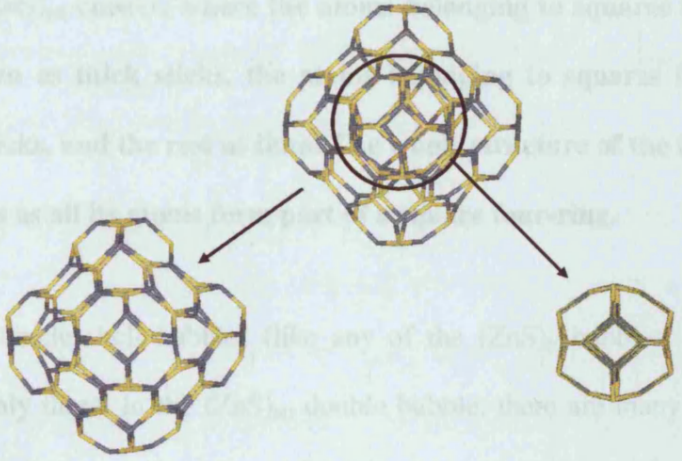

Figure 3.5

Structure of the $(ZnS)_{60}$ cluster. The central cluster is the double bubble. The innermost encircled shell is also shown in the right corner, and is a $(ZnS)_{12}$ bubble with the structure of a sodalite cage, which provides it a high stability. The outermost shell, which is a $(ZnS)_{48}$ buble, is shown in the left side.

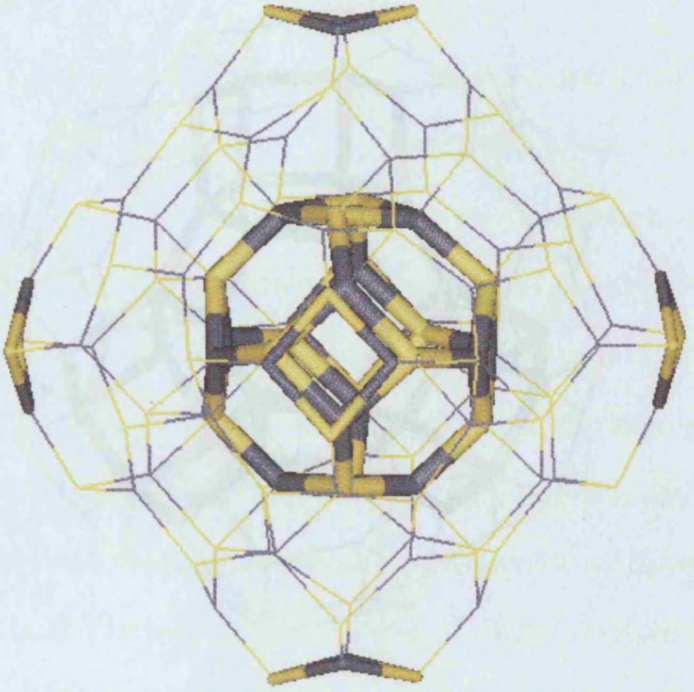

Figure 3.6

View of the $(ZnS)_{60}$ cluster, where the atoms belonging to squares in the innermost bubble are drawn as thick sticks, the atoms belonging to squares in the outermost bubble as thin sticks, and the rest as lines. The whole structure of the $(ZnS)_{12}$ bubble is drawn with sticks as all its atoms form part of a square four-ring.

Atoms in single shell bubbles (like any of the $(ZnS)_n$ bubbles, n=10-47) have a coordination of only three. In the $(ZnS)_{60}$ double bubble, there are many four-coordinated atoms. Figure 3.7 shows another view of the particle, highlighting the four-coordinated atoms, as well as the atoms bonded to them. Most of the atoms in the innermost bubble belong to a network of tetra-coordinated atoms; the average bond distance of the innermost bubble is ~2.36Å. For the outermost bubble, the distance is ~2.31Å. The distance between atoms bonding the two shells is ~2.46Å. This larger distance implies that the bonds between the two shells are weaker than the bond within any single shell.

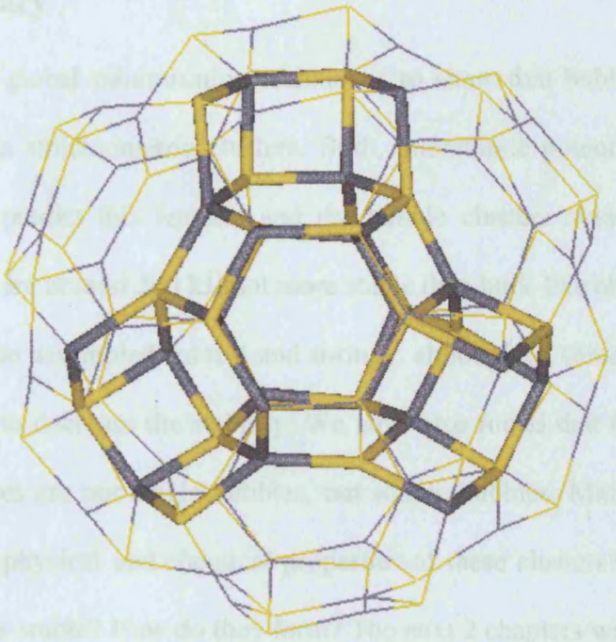

Figure 3.7

View of the $(ZnS)_{60}$ cluster, where the tetra coordinated atoms and those bonded to them are shown as sticks, while the rest are lines. Note the five channels formed between the innermost and outermost shell, three of which are clearly seen and the other two are aligned in a direction perpendicular to the figure.

The presence of the network of tetra coordinated atoms, and recent experimental and theoretical studies[101] suggest a possible path whereby bubble clusters can grow and form bulk-like clusters, which are more stable for larger cluster sizes. It might be possible for some of the atoms in this network to undergo slight changes and form a region of bulk-like structure inside the cluster. This region could nucleate the process of structural transformation of the whole cluster.

3.5 Summary

We have applied global minimisation techniques to show that bubble clusters are more stable than bulk-like stoichiometric clusters. Both, interatomic potentials methods and *ab initio* calculations, predict this feature; and the bubble clusters obtained with Simulated Annealing methods are around 200 kJ/mol more stable than bulk-like clusters.

Bubble clusters are assembled from 4 and 6-rings, although in some cases octagons also appear, which tend to decrease the stability. We have also found that for larger clusters the most stable structures are not single bubbles, but souble bubbles. Many questions are now open. What are the physical and chemical properties of these clusters? Up to what size are these open structures stable? How do they form? The next 2 chapters will try to answer these questions. We also note that in our study, only stoichiometric clusters were investigated, as in experimental studies on onion fullerenes-like clusters of BN[90]. It may be that under certain conditions, the growth of ZnS clusters, occurs via structures whose composition is non-stoichiometric, which may favour more bulk-like structures. This question will be addressed in the chapter 5. The present study, however clearly shows that large spheroidal stoichiometric clusters of ZnS may be stable, as well as onion-like structures formed inserting one bubble inside another.

CHAPTER 4

THEORETICAL PREDICTION OF THE PROPERTIES OF $(ZnS)_n$ CLUSTERS, n=10-80

4.1 Introduction

The appearance of the double bubble structure for large clusters, discussed in the previous chapter, provides an additional incentive to the study of larger clusters; so in this chapter we present the results obtained for the $(ZnS)_{70}$ and $(ZnS)_{80}$ clusters. $(ZnS)_{50}$ is also investigated to gain a better idea of the cluster size at which double bubbles start to predominate. The structures of these three new clusters are calculated with the same Simulated Annealing described in the previous chapters. In this chapter, however, we also carry out an extensive study of the properties of all the clusters we have investigated, with the double goal of getting a better understanding of these structures, and also providing information that can be compared with experimental data, in order to guide future experimental studies.

4.2 Results and discussion

We divide this section in 5 separate subsections: first we present the structures of several representative clusters, followed by an analysis of their radial distribution functions. Their vibrational spectra are also calculated and discussed. The last two subsections study the relative stability of the bubble clusters and the band gap of all the clusters. We focus on the variation of these properties with the cluster size.

4.2.1 *Structural analysis: cluster structures*

We presented the structures of some bubble clusters, and the onion-like structure of the $(ZnS)_{60}$, in chapter 3. In the next two figures we now present the structures of some other bubbles, as well as the three new double bubbles: $(ZnS)_{50}$, $(ZnS)_{70}$ and $(ZnS)_{80}$ (see Figure 4.2).

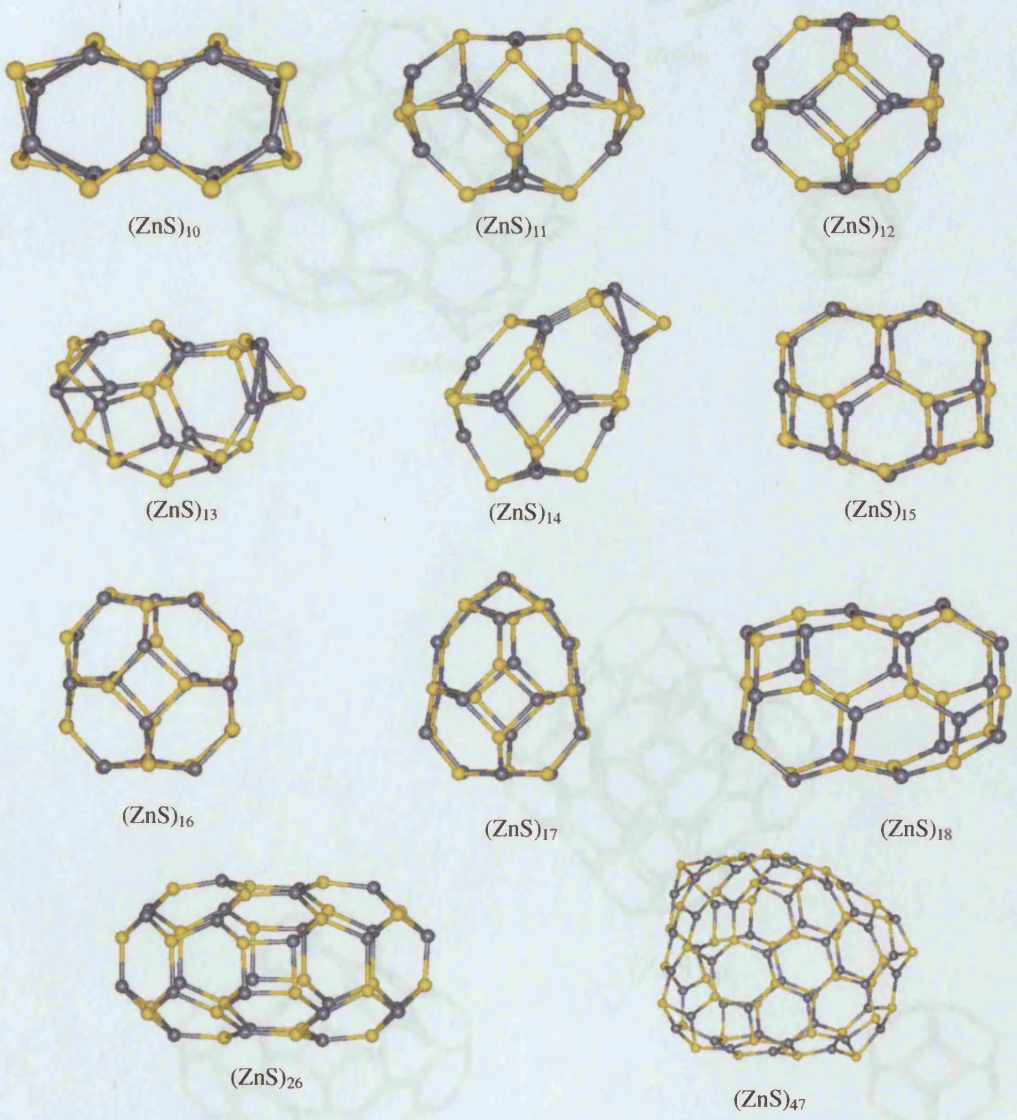

Figure 4.1

Structures of selected bubble clusters. Yellow balls refer to sulphide atoms and blue balls to zinc atoms.

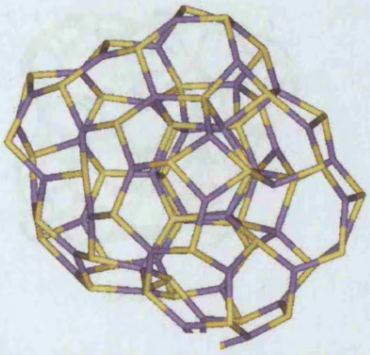

$(ZnS)_{50}$

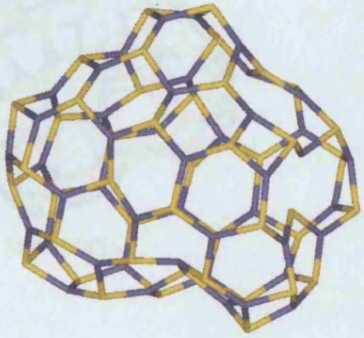

$(ZnS)_{44}$

$(ZnS)_6$

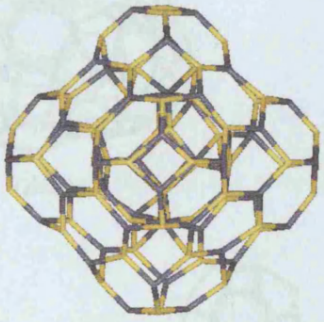

$(ZnS)_{60}$

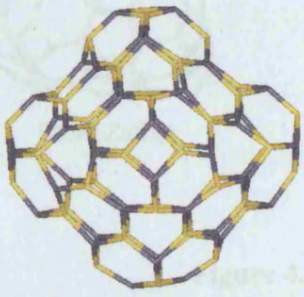

Shell $(ZnS)_{48}$

Core $(ZnS)_{12}$

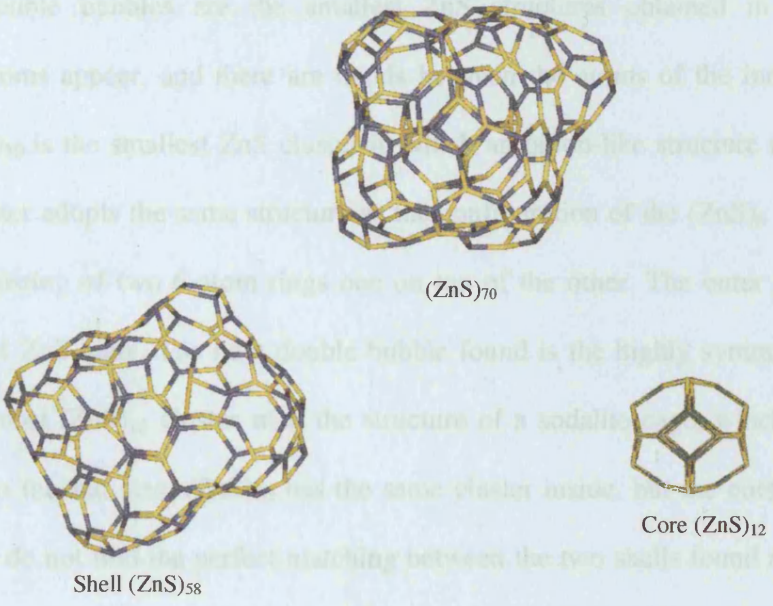

Figure 4.2

Structures of the four bubble clusters studied. The complete structures are shown in the central figures, while the innermost and outermost clusters are shown below them.

The double bubbles are the smallest ZnS structures obtained in which four coordinated atoms appear, and there are bonds between the atoms of the inner and outer bubbles. $(ZnS)_{50}$ is the smallest ZnS cluster in which an onion-like structure is found. The innermost cluster adopts the same structure as the configuration of the $(ZnS)_6$ cluster found in vacuo, consisting of two 6-atom rings one on top of the other. The outer structure is a bubble with 44 ZnS units. The next double bubble found is the highly symmetric $(ZnS)_{60}$, with an innermost $(ZnS)_{12}$ cluster with the structure of a sodalite cage, which is the most stable in vacuo for that size. $(ZnS)_{70}$ has the same cluster inside, but the outside bubble is larger, and we do not find the perfect matching between the two shells found in the $(ZnS)_{60}$ cluster. The structure of the $(ZnS)_{80}$ cluster shows a larger bubble inside, which is the same as that obtained for the $(ZnS)_{17}$. The outermost bubble is the largest found so far, with 63 ZnS units.

4.2.2 *Structural analysis: radial distribution functions*

The radial distribution function (RDF) gives us more detailed information on the geometrical properties of clusters. Analyses of the calculated RDFs are therefore reported for selected clusters and comparisons are made with the RDFs of the bulk polymorphs. The Zn-S RDF in Figure 4.3 shows that the first neighbour Zn-S bond distances in the bubble clusters (≈2.25Å) are shorter than in both bulk polymorphs (=2.34Å), which is primarily a consequence of the lower coordination numbers in the clusters compared to the bulk. The Zn-S bond distances seem to be independent of the size of the bubbles, as there is no significant shift in the first neighbour peak with size. The double bubbles are the first clusters in which there are tetracoordinated atoms, which makes the atomic surroundings more similar to those found in the bulk structures; indeed the Zn-S distance increases to 2.30Å, very close to the bulk value. Note, however, that the Zn-S-Zn and S-Zn-S angles in the double bubbles vary between 100° and 125° far away from the 109.5° corresponding to a

tetrahedral arrangement. The network of four coordinated atoms clearly still needs to undergo substantial structural transformation in order to resemble either of the bulk-like phases.

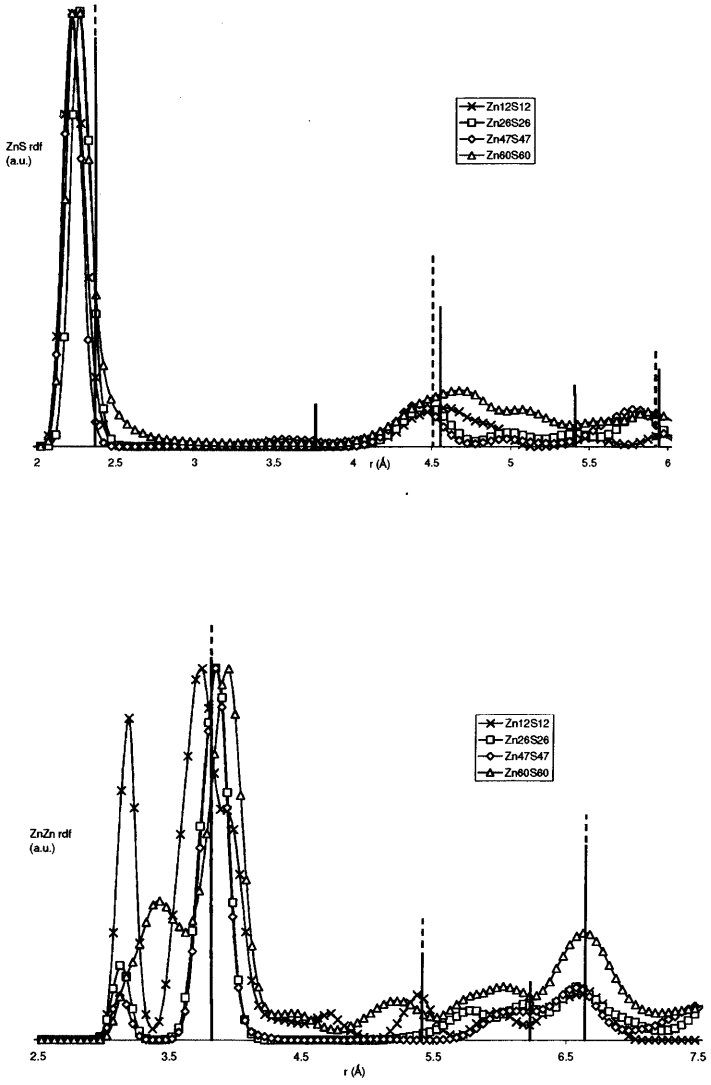

Figure 4.3

Zn-S and Zn-Zn radial distribution functions of representative single and double bubble clusters. For comparison, the RDFs of the two ZnS bulk phases are also plotted; the continuous lines correspond to wurtzite and the discontinuous lines to sphalerite.

Figure 4.3 also shows the Zn-Zn RDF of the same set of clusters. There is a peak at 3.75Å, associated with the Zn-Zn distance in a 6-ring for both polymorphs, because both are formed by three dimensional stacking of 6-rings. Since single and double bubble clusters have 6-rings in their structures, they also show a similar peak in the RDF. Double bubbles also have at least six 4-rings beside the 6-rings. These 4-rings contribute to the RDF with the first peak observed, at a distance of 3.15Å. While the second Zn-Zn peak seems to be constant for all the clusters, the first peak tends to decrease as the cluster size increases, since the ratio (number of 4-rings)/(number of 6-rings) decreases with the cluster size.

The Zn-Zn RDF of the $(ZnS)_{12}$ cluster is quite different from the others, since $(ZnS)_{12}$ is an unusual structure, in which all the Zn atoms are part of 4-rings as well as 6-rings, hence generating a shift of the first peak to a larger distance and the second to a shorter distance.

The Zn-Zn RDF of the $(ZnS)_{60}$ cluster is similar to those of the other double bubbles, and shown in Figure 4.3. Remarkably, however, there is no sharp peak associated with the first neighbour. The first peak is very broad, spreading significantly in the range 3.4Å-3.7Å, for which there are two reasons: (i) the structures are less spherical: they have more protuberances, which lead to some bent 6-rings in which the Zn-Zn distance decreases from 3.75 to the range previously noted; (ii) the Zn atoms of the innermost bubbles do not necessary form 4- or 6-rings with the atoms of the outermost bubbles; they form the bonding structure that minimises the global energy, which results in the Zn-Zn distances between atoms in the two bubbles varying within the described range. It is interesting to note that, unlike the disorder associated with the first Zn-Zn neighbours, the second, third and fourth neighbours show peaks that are similar to those found in the two bulk phases.

4.2.3 *Vibrational analysis*

Here we present a vibrational analysis of the bubble structures and related bulk-like clusters, by calculating harmonic frequencies at the PW91/ecp-dnp level of theory using the DMol^3 code. These harmonic frequencies have been fitted with Lorentzian transformations in order to obtain theoretical IR spectra, which are comparable to the experimental IR spectrum. In Figure 4.4, the calculated spectra of bubble clusters are displayed, showing the existence of a dominant peak at around 360 cm^{-1}, the only significant peak observed, which can be assigned to the motion of three-coordinated S atoms.

The calculated spectra of selected bulk-like clusters are also presented in Figure 4.4, showing clear differences with respect to the bubble structures, of which the main is that the spectra are much broader, with several peaks giving significant intensities. There is a peak in the same frequency as the dominant one for the bubble clusters (360 cm^{-1}), which arises from the three-coordinated atoms that the clusters have in the outer regions. There is another prominent peak at around 320-330 cm^{-1}, which is assigned to the vibrations of the four-coordinated atoms in the inner regions of the bulk-like clusters. There are also some two-coordinated atoms that contribute to the broadening of the spectra in the region from 220 cm^{-1} to 360 cm^{-1}.

Clearly, if clusters of this size can be synthesized, the vibrational spectra could help to determine the structures. In particular, if the lower frequency features in the range 200 cm^{-1}-360 cm^{-1} were observed, bulk like structures would be indicated.

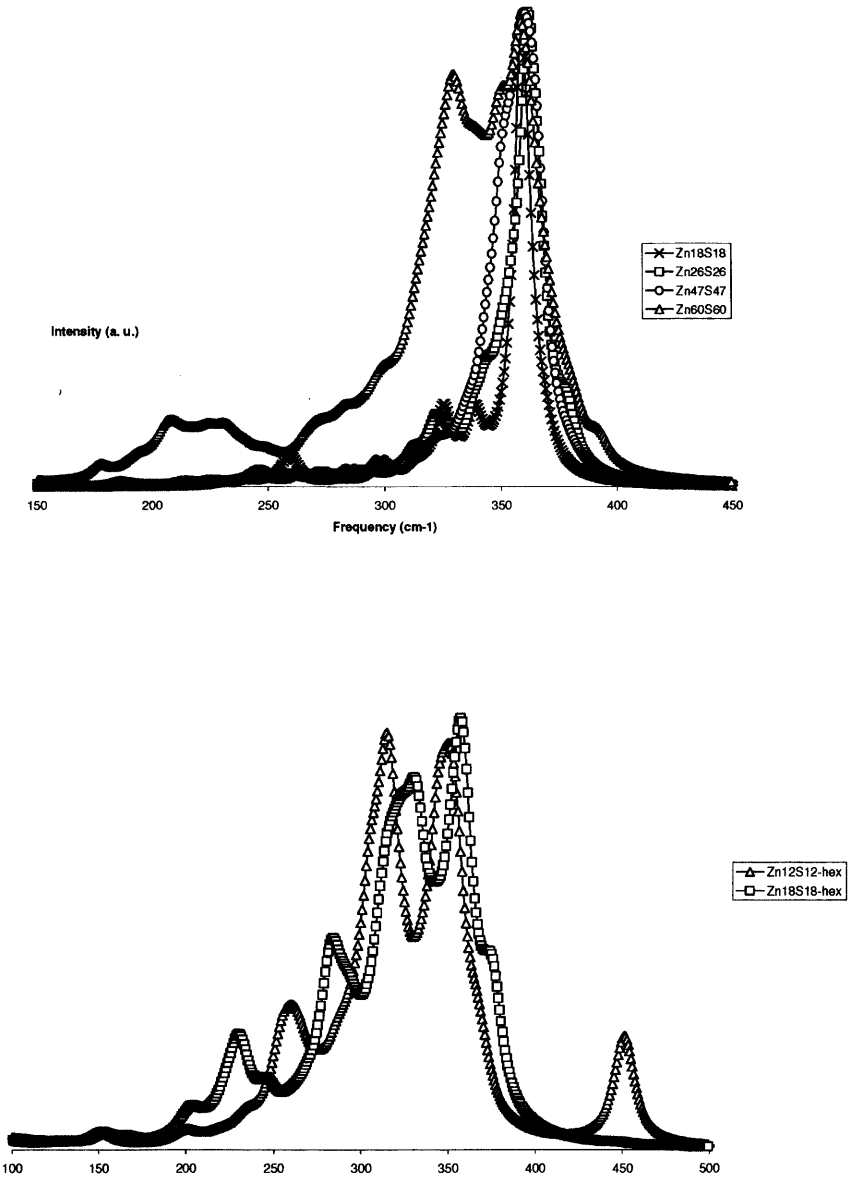

Figure 4.4

IR spectra of selected ZnS clusters. The top figure shows the spectra of three single bubbles and one double bubble. There is no trend followed as the cluster size increases; all clusters show a prominent peak at 360cm^{-1}. The main difference comes with the appearance of a different peak for the $(ZnS)_{60}$ double bubble, due to the network of four coordinated atoms. The bottom figure presents the spectra of bulk-like clusters.

The IR spectrum of the $(ZnS)_{60}$ double bubble is shown in Figure 4.4. It has the same dominant peak associated to the vibrations of three-coordinated atoms that the bubble clusters have, at 360 cm^{-1}, but also shows the peak associated with the vibrations of four-coordinated atoms, at 330 cm^{-1}. The result is a spectrum that is more similar to the bulk-like clusters than to bubble clusters, which is not surprising, since this cluster has a network of four-coordinated atoms.

4.2.4 *Relative stability of the bubble clusters*

To study the stability of clusters, we calculate the evolution of the nucleation energy, $E_{nuc}(n)$, defined as:

Eq. 71 $$E_{nuc}(n) = E(n) - E(n-1) - E_{ZnS}^{Bulk}$$

where $E(n)$ is the total energy of the $(ZnS)_n$ cluster, and E_{ZnS}^{Bulk} is the energy per ZnS unit in the sphalerite polymorph bulk. The nucleation energy gives information about the cluster growth. The more negative the nucleation energy is for a given cluster, the more thermodynamically favourable is the addition of a ZnS unit.

Figure 4.5 shows the variation of the nucleation energy as a function of the cluster size, calculated with two methods pure-DFT and interatomic potentials based calculations. Both methods give similar results. At the bottom of Figure 4.5 we can see the difference between the nucleation energies calculated with both methods:

Eq. 72 $$\Delta E_{nuc}(n) = \{E_{nuc}(n)\}^{IP} - \{E_{nuc}(n)\}^{pure-DFT}$$

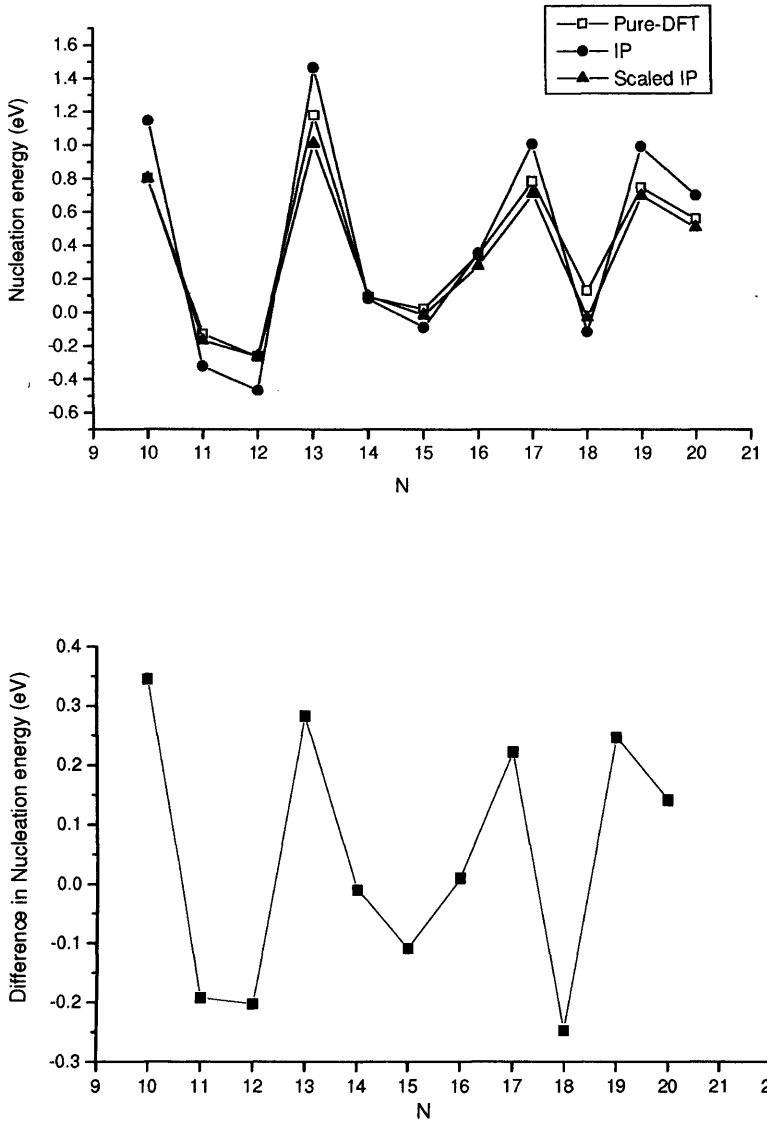

Figure 4.5

The top figure shows the values of the nucleation energies for $(ZnS)_n$ clusters (n=11-20), calculated using Eq. 71. The difference between the values obtained with interatomic potentials (IP) and with pure density functional theory (DFT) is shown in the bottom figure. Note that that difference has a similar behaviour to the nucleation energies, which allows us to scale the IP values to make them closer to the DFT ones, making use of the linear dependence expressed in Eq. 73. The top figure also shows the nucleation energies calculated after scaling the IP values, which are now very close to the DFT ones.

Two features are evident in that figure. The first is that the maximum difference in energy between both methods is smaller than 0.4eV. The second is more significant: the plot of $\Delta E_{nuc}(n)$ resembles the behaviour of $E_{nuc}(n)$ itself. It is then possible to scale the values of $\{E_{nuc}(n)\}^{IP}$ in order to give values closer to $\{E_{nuc}(n)\}^{pure-DFT}$. The scaled nucleation energies are calculated by:

Eq. 73 $$\{E_{nuc}(n)\}^{IP}_{scaled} = A * \{E_{nuc}(n)\}^{IP} + B,$$

where A and B are fitted constants, calculated by requiring that there are two points at which $\{E_{nuc}(n)\}^{IP} = \{E_{nuc}(n)\}^{pure-DFT}$. The election of these two points is almost irrelevant, so we chose n=10 and =12, which give the following values for the constants: A=0.66, B=0.05. Figure 4.5 also shows the close similarity between the two curves: $\{E_{nuc}(n)\}^{IP}_{scaled}$ and $\{E_{nuc}(n)\}^{pure-DFT}$ are for all clusters; the difference is now less than 0.16eV, which is small compared to the absolute values of the nucleation energies. The point of this analysis is that we may now use only interatomic potentials methods in order to calculate the nucleation energies for the bigger clusters, with a similar accuracy to that of the more time consuming pure-DFT calculations.

Scaled nucleation energies of all the clusters are reported in Figure 4.6. The main characteristic is the oscillatory behaviour with increasing size, rather than a constant trend. For example, the addition of a ZnS unit to the $(ZnS)_{11}$ cluster is a thermodynamically favoured process, as it leads to the highly symmetric and stable $(ZnS)_{12}$ cluster. But the addition of a further ZnS unit to this cluster reduces its stability; there is a big change in the geometry, and the $(ZnS)_{13}$ cluster is much less symmetric than $(ZnS)_{12}$ (see Figure 4.1). This difference in stability is reflected in the high positive nucleation energy of $(ZnS)_{13}$.

Interestingly the highest peak in experimental mass spectra[98, 102] corresponds to the $(ZnS)_{13}$ cluster, which our calculations show to be one of the less stable clusters, suggesting that kinetic factors stabilize that cluster rather than the thermodynamic features discussed in this study. A core-cage structure[102] has been suggested for that cluster to explain its high stability in thermodynamic terms, but recent DFT calculations[103] show that that structure is indeed less stable than the bubble cluster.

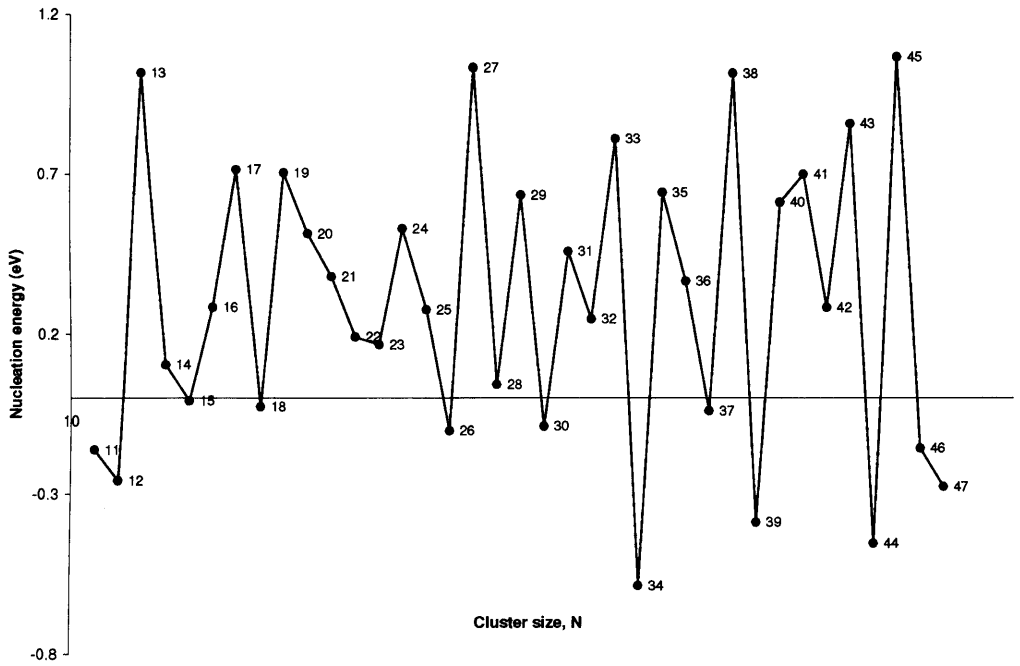

Figure 4.6

Nucleation energies of $(ZnS)_n$ clusters (n=11-47) calculated with IP, after applying the scaling factors to correct them.

Another interesting feature to note from Figure 4.6 is the parity of the maxima and minima. Most of the maxima correspond to $(ZnS)_n$ odd numbered clusters, whereas the minima correspond to even values of n. The latter are more stable owing to their more symmetric structures.

4.2.5 *Calculated band gaps*

Many electrical and optical properties are directly related to the band gap. We have calculated thus their energies using PW91/ecp-dnp procedure, as the difference in energy between the HOMO and the LUMO. Although there are more elaborate definitions of the band gap, this simple formulation allows us to compute qualitatively the trend in band gap energy with cluster size. The experimental value for bulk ZnS is 3.6 eV, while our pure DFT calculations give an energy of 2.1 eV, a difference between calculated and experimental values that falls within the usual DFT errors when calculating band gap energies[104, 105]. We assume that this shift in the band gap energy is constant for any cluster, so we add a correction of 1.5 eV to all the calculated band gaps. Support for this procedure is provided by calculations of the smaller clusters using B3LYP functionals; the values of the calculated band gaps fall within 0.15 eV of those obtained from the PW91/ecp-dnp calculations plus energy shift, corroborating the validity of adding the energy correction. Figure 4.7 shows the band gap energies of some bubble, double bubble and bulk-like clusters as a function of the cluster size (including the 1.5 eV correction). The so-called quantum size effect results in the band gap of nanoparticles of many systems decreasing as the particle size increases.

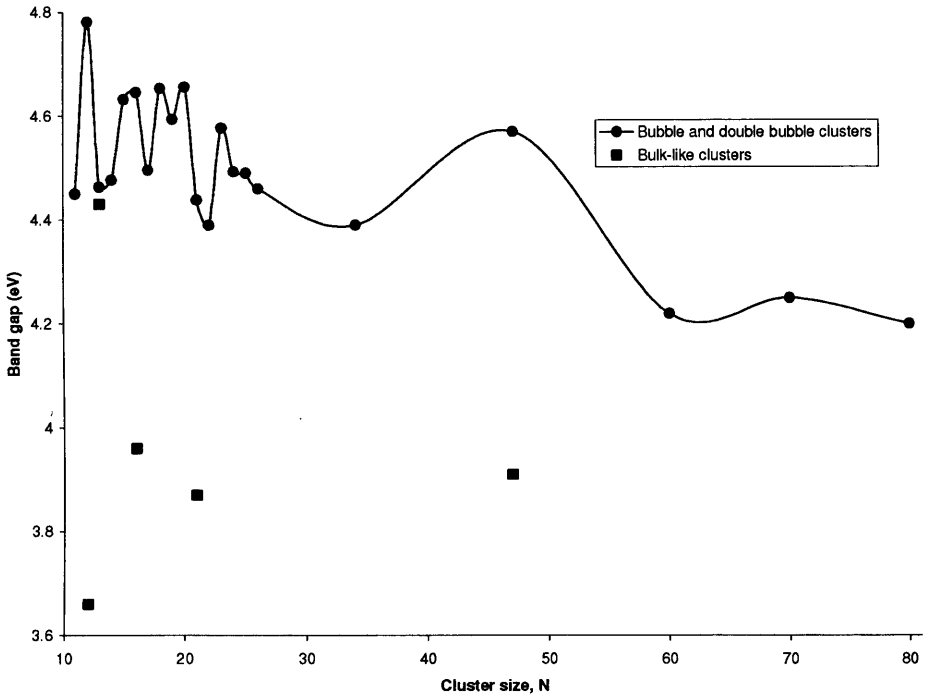

Figure 4.7

Band gap energies of bubble, double bubble and bulk-like clusters, obtained with DFT calculations. The band gap energy of the bulk ZnS (3.6eV) is set as the reference level. Bulk-like clusters have smaller band gaps compared to bubble clusters, whose band gaps vary from 4.4eV to 4.8eV. As observed in other properties, the appearance of a network of four coordinated atoms in double bubble clusters induces a change in the band gap, making it lower and more stable with respect to the cluster size.

Of all the clusters, $(ZnS)_{12}$ is that with the highest band gap, while $(ZnS)_{80}$ has the lowest with a difference of 0.55 eV. With the exception of $(ZnS)_{12}$, the band gap energies of the bubble clusters oscillate between 4.4 eV and 4.7eV, and there is no clear trend when increasing cluster size, which suggests that the electronic structure of all the clusters is similar, with its characteristics being governed not by the cluster size, but by the geometrical structure, which is the same in all: hollow clusters with three coordinated atoms forming 4

and 6-rings. The band gap of the $(ZnS)_{60}$ cluster is smaller than the band gap of the single bubble clusters, suggesting a change in the electronic structures of the clusters. The presence of a network of tetracoordinated atoms changes the electronic structure. Since there is not a clear trend of the band gap with respect to the cluster size, we can conclude that the small band gap of the $(ZnS)_{60}$ cluster is not due to the quantum size effect, but to the presence of the network of four-coordinated atoms.

The band gap energies of some bulk-like clusters are also shown in Figure 4.7. The most important feature observed is that bulk-like clusters have smaller band gap energies than the bubble clusters, typically between 3.6 eV and 4 eV, with the exception of the bulk-like $(ZnS)_{13}$ cluster, whose band gap is similar to that of the $(ZnS)_{13}$ bubble cluster of 4.43 eV. All these results suggest that the band gap would be another useful quantity indicative of the structure of these nanoclusters.

Further more detailed calculations of band gaps and electronic transitions in single and double bubble clusters would be of great interest.

4.3 *Conclusions*

The most important findings of this chapter are as follows:

- The stability of bubble like clusters for $(ZnS)_n$ is confirmed for n=10-80; double bubble structures predominate for the larger clusters.

- Experiments aiming to detect the presence of bubble clusters can use the Zn-Zn and Zn-S RDFs as evidence. A peak at the usual Zn-Zn first neighbours distance (3.75Å), and an additional one at a shorter distance (around 3.15Å) would suggest that small bubble clusters have been found.

- Measurements of the vibrational spectra may be able to distinguish between bubbles and bulk-like clusters. There will be a strong peak at around 360 cm^{-1} in both cases, but the appearance of another peak at around 320 cm^{-1} would strongly suggest that four-coordinated atoms are present, as is the case of bulk-like clusters or double bubbles.

- The nucleation energy changes with the cluster size, with no definite trend. Some clusters have much higher nucleation energies, which will have faster growth and therefore will be the predominant species. Clusters with even numbers of ZnS units tend to be more stable than odd numbered clusters.

- The band gap energy of the bubble clusters does not change significantly with the cluster size, as it appears to be dominated by the local coordination. The band gaps of the double bubbles are smaller than those of the single bubbles.

Overall, the results in this chapter reveal a fascinating and rich nanochemistry of these clusters, which would reward detailed experimental investigation.

CHAPTER 5

SIMULATION OF ZnS NUCLEATION IN AQUEOUS SOLUTION

5.1 Introduction

All the cluster structures calculated so far have been obtained in vacuo, without taking into account the influence of solvent. Solvent may change the situation, preventing the formation of the bubbles, or perhaps inducing different structures. In addition, we have so far not considered non-stoichiometric clusters. All these possibilities are studied in this chapter, in which we carry out a survey of the processes of ZnS cluster formation from aqueous solution. This final chapter allows us to have a general idea of the processes of cluster formation and nucleation of ZnS both in vacuo and in aqueous solution.

Traditionally, nucleation processes have been explained using what it is now called Classical Nucleation Theory (CNT), which has been discussed in section 2.7. CNT gives a qualitative explanation of many nucleation events in simple systems (such as nucleation from the melt) but it fails to make quantitative predictions, and the introduction of empirical parameters is required. Moreover, in some cases, as in the case of nucleation from solution, CNT gives poor results. A description of the limitations of CNT can be found in ref [106].

Since water is the most important solvent, several experimental studies have been directed towards getting a better understanding of the nucleation of ZnS in water[92, 101, 107]. EXAFS data suggest[108] the presence of small ZnS particles (<20nm) ,with very strong Zn-S bonds, that are not in reversible equilibrium with the solution phase. Electrochemical and spectroscopic experiments[92] show that zinc and sulfide ions in solution initially form pure ZnS clusters, without hydrogen present. For this reason, the approximation we use in our work of neglecting water dissociation to form H_3O^+, OH^- and HS^- complexes in water is unlikely to be significant.

The chapter is organized as follows. Section 5.2 describes the methodological aspects of the simulations; section 5.3 presents and discusses our results on both NVT and NPT simulations at a variety of temperatures and with different starting configurations. Our simulations provide detailed models for the nucleation of this material.

5.2 Computational details

We study the processes of formation and growth of ZnS clusters in water solution, using molecular dynamics simulations, employing the DL_POLY code. The influence of the temperature and of the solute concentration is investigated by performing simulations at two temperatures (300K and 500K) and four different concentrations (0.5M, 0.75M, 1.0M and 1.25M). The systems consisted of Zn^{2+} and S^{2-} ions randomly placed in a cubic box of 30Åx30Åx30Å size. The box is then filled with water molecules at the density of liquid water at room temperature ($0.977 g/cm^3$). Solutions of the four different concentrations are achieved by having respectively 8, 12, 16 and 20 Zn^{2+} and the same number of S^{2-} ions in the box, plus 818 to 842 water molecules depending on the number of ions. The first part of the simulations is a pre-equilibration period of 40ps, in which the Zn^{2+} and S^{2-} ions are kept fixed and the water molecules are allowed to move. A further 20ps run of equilibration is then applied, in which all the atoms are free to move. In order to reduce the effect of the initial configuration, two systems with different initial configurations for each concentration have been investigated. Simulation times range from 1.5ns to 6 ns.

The interatomic potentials used to describe Zn-Zn, Zn-S and S-S interactions have been successfully used previously to model ZnS surfaces as well as small clusters in chapters 2, 3 and 4. Interatomic potentials to describe the interaction between ZnS and water molecules[101] have been reported, but they fail to reproduce the values of bond distances and adsorption energies of small clusters obtained with DFT calculations. For this reason we

decided to derive a new set of interatomic potentials giving us the accuracy needed to perform the calculations. The derivation of the potentials is developed in section IIIa.

The polarizability of the S^{2-} ions is modelled via the shell model of Dick and Overhauser, discussed in section 2.1.3. A positively charged core (bearing all the mass of the ion) is connected to the massless, negatively charged shell by a harmonic spring. In static methods, such as energy minimization, the introduction of the shell model does not introduce any complications. In molecular dynamics however, shells cannot be straightforwardly introduced as they are massless. Two methods have been used to overcome this problem. The first, in the spirit of the Born-Oppenheimer approximation, performs an energy minimization of the shells at each step of the molecular dynamics simulation, so that there are no forces acting on the shells[20] before the next MD step. It would be impractical for us to use this method because it is extremely time consuming (as several minimization steps are required within each MD step) and it would not allow us to run the nanosecond simulations that are needed in the present study. We therefore opted for the second method, assigning a small mass (0.2 au in our case) to the shells[21]. Unfortunately, this method is also not without problems, as there is usually a small transfer of energy from the rest of the system to the core-shell vibrations. For very long calculations, as in the present study, this process could become problematic, since the core-shell vibrations can store a large amount of unrealistic kinetic energy. The real physical system would then lose some of its kinetic energy and ultimately it could freeze. It is possible to solve the problem by introducing an additional thermostat controlling the temperature associated with the core-shell degrees of freedom[111], but we followed a simpler approach. We introduced a small frictional drag force, b, which varies linearly with the core-shell velocity. The force between a core and shell separated by a distant x becomes now $f_{cs} = \frac{1}{2}kx^2 - b\frac{dx}{dt}$. The critical value at which the core-shell stops oscillating is b_{crit}= 462.7au/ps. We introduce a friction constant of 15au/ps, which is only 2% of the critical

value. As a result, the polarizability of the S^{2-} ion is properly described, while the core-shell temperature is maintained constant at a low level. We made the necessary changes in the DL_POLY code to include the frictional term. This friction force might induce a loss of energy of the system. To minimize this undesirable effect we chose to use the Gaussian isokinetic thermostat[18, 19, 112] to maintain the room temperature during the simulations, in which the total energy is not constant, but allowed to change in order to maintain a constant temperature. The timestep used in these simulations must be small, 0.3fs, in order to model correctly the fast vibrations of the shells, caused by their small mass.

5.3 Results and discussion

5.3.1 NVT simulations at 300K

The first sets of simulations were performed in the NVT ensemble at room temperature. During the equilibration period, the hydration spheres around the Zn^{2+} and S^{2-} ions are formed. The water molecules of the $Zn(H_2O)_6^{2+}$ complex have a strong interaction with the Zn^{2+} cation. We did not observe any exchange of water molecules between the first and second hydration spheres during the simulations, which is consistent with the experimental value[113] of the residence time of $3x10^{-8}$ s. Figure 5.1 shows the Zn-O radial distribution function (RDF) and coordination number of the Zn^{2+} cation in a $Zn(H_2O)_6^{2+}$ complex. There is a prominent peak at 2.07Å, which corresponds to the positions of the oxygen atoms in the first coordination shell of the hexa-aquo complex. The second coordination shell is less clearly defined, since its associated peak is smaller and it spreads over a broader region, from 4.2Å to 4.7Å. The maximum in this second peak is at 4.38Å, with a coordination number of 12.3.

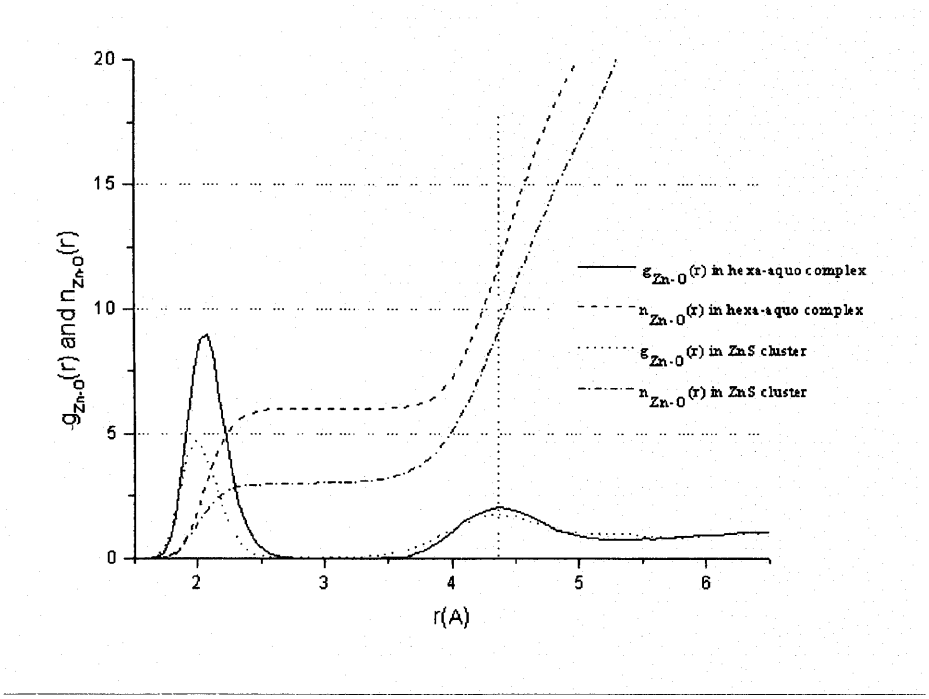

Figure 5.1

Zn-O RDFs and coordination numbers in two different configurations: Zn in a $Zn(H_2O)_6^{2+}$ complex and in a ZnS cluster. The coordination number in the latter case shows that a $ZnS(H_2O)_3$ complex is formed.

S^{2-} anions do not form a stable complex with the water molecules, since the interaction with them is weaker. They interact with 8-12 water molecules in the first hydration shell (see S-O rdf in Figure 5.2), but the residence time is very short, and they are constantly being replaced by molecules from the second hydration shell. Zn^{2+} and S^{2-} anions eventually interact to form a ZnS cluster, for which the time necessary depends on the concentration of the solution.

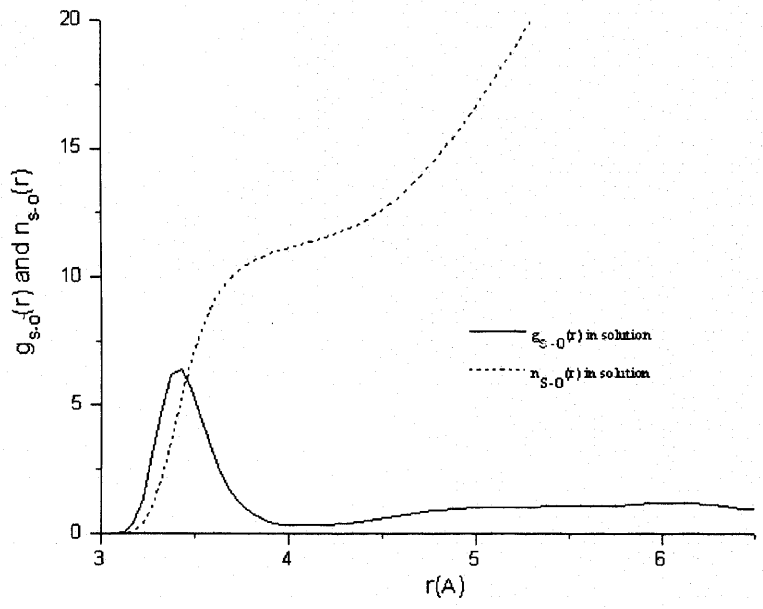

Figure 5.2

S-O RDFs and coordination number of S^{2-} in solution. The data indicate that there is no formation of a stable complex with water molecules.

The gain in energy accomplished by the formation of this ZnS bond from an $Zn(H_2O)_6^{2+}$ complex and a S^{2-} anion in water solution is -164 kJ/mol. This value is calculated using two simulations: one with a ZnS cluster in water, and another in which the two ions are separated. The Zn-O RDF and coordination numbers of a Zn atom in a ZnS cluster are plotted in Figure 5.1, clearly showing that the number of water molecules in the first hydration shell reduces to three. As can be seen in Figure 5.3, the oxygen atoms interacting with a ZnS cluster occupy three vertices of a tetrahedron and the S atom occupies the fourth.

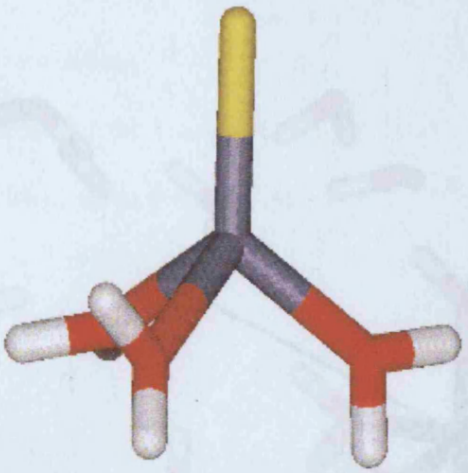

Figure 5.3

Structure of the ZnS cluster, which is bound to three water molecules and forms a $ZnS(H_2O)_3$ complex. Yellow stick represents S; blue stick represents Zn; red sticks represent O and white sticks represent H. The same colours code applies to all figures.

Despite the thermodynamic driving force, there is an energy barrier opposing the formation of a ZnS cluster from a $Zn(H_2O)_6^{2+}$ complex and a S^{2-} anion. There is a strong electrostatic attraction between Zn^{2+} and S^{2-}; but the hydrated Zn^{2+} is also strongly bound to the water molecules. An outer-sphere complex is then formed in which the $Zn(H_2O)_6^{2+}$ complex remains in fact with the S^{2-} ion at a distance of 4.6Å (Figure 5.4). Ion pairs are stable units at room temperature; they move through the liquid water without dissociating for hundreds of picoseconds. A Zn^{2+} atom can be part of more than one ion pair, since two ion pairs can interact to form a larger entity, in which the Zn^{2+} cations stay in their hexa-aquo complexes while the S^{2-} anions oscillate at 4.6Å from the Zn^{2+} atoms. As a result, a network of ion pairs is formed, involving most of the Zn^{2+} and S^{2-} ions, and creating areas with high concentrations of solute separated from areas in which no solute is present. Studies in different systems suggest that this phase separation might be the first stage of the nucleation process[4, 106, 114]. It was observed in all our simulations at room temperature, regardless of the concentration.

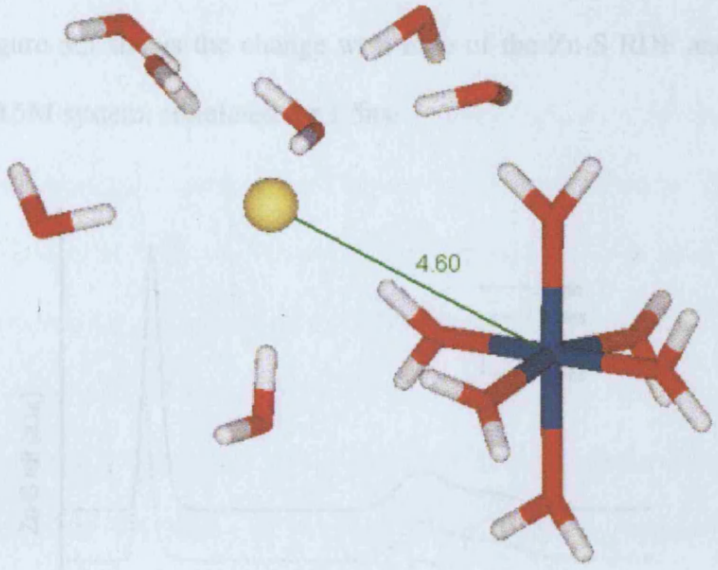

Figure 5.4

Snapshot of an ion pair with water molecules surrounding the S atom. The ion pair is formed by the $Zn(H_2O)_6^{2+}$ complex and the S^{2-} ion, attracted by coulombic forces. They move through the liquid with an average distance of 4.6Å. Zn and S do not immediately form a cluster, owing to the presence of the six water molecules strongly bound to the Zn.

We proceed now to give the detailed results obtained for each concentration derived from the NVT simulations at 300K.

0.5M concentration.

Figure 5.5 shows the change with time of the Zn-S RDF and coordination number (cn) of a 0.5M system, simulated for 1.5ns.

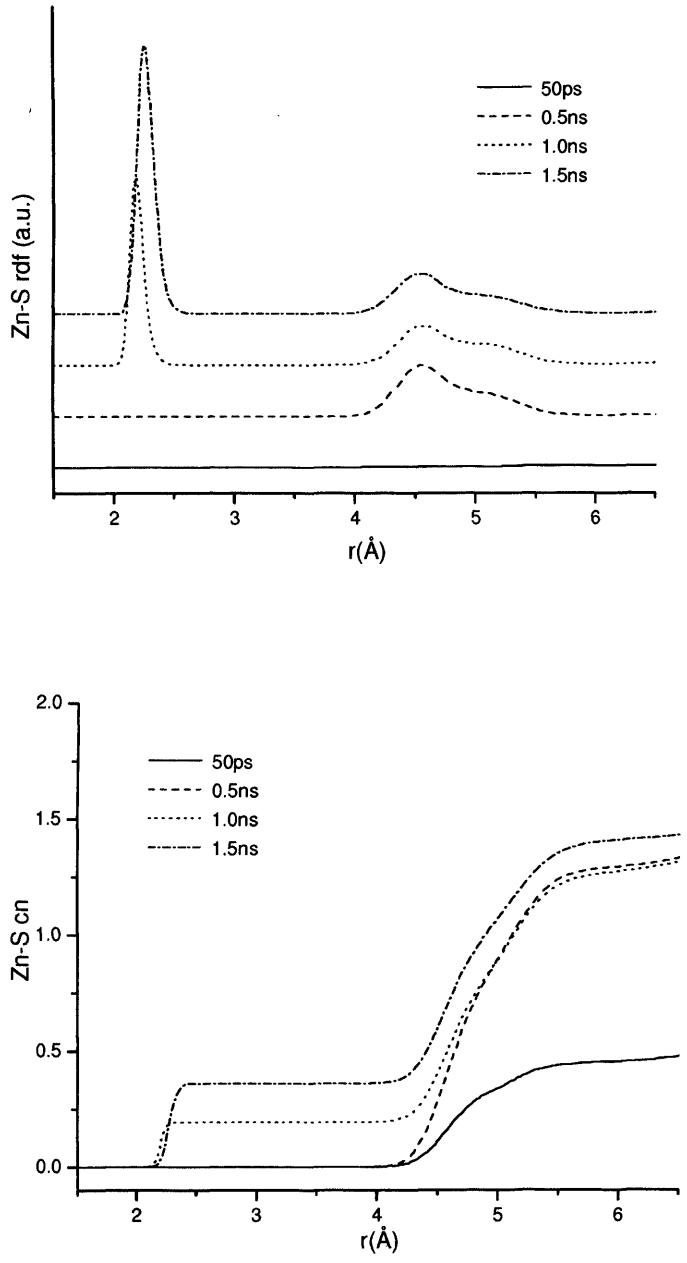

Figure 5.5

Zn-S RDFs and coordination numbers during the simulation, at a 0.5M concentration.

The RDF after 50ps is flat, showing that there is very little order (due to the random initial distribution of the ions) and no ion pairs are formed yet. After 500ps we observe a small broad peak around at 4.6Å, corresponding to the ion pair Zn-S distance. The broadening of the peak is attributable to the S^{2-} ions, which are relatively free to move in the areas around hexa-aquo complexes. There is a smaller shoulder at 5.2Å, the cause of which is a small change in the Zn-S distance that occurs when two ion pairs interact. At 1ns we see a sharp peak appearing at 2.1Å, which is the Zn-S distance in a ZnS pair, indicating that the activation energy for breaking the $Zn(H_2O)_6^{2+}$ complex has been overcome to form the pair. Once this cluster is formed, the energy barrier to break it is even larger than that to create it, hence there is no dissolution of any ZnS cluster in all the simulations, in agreement with experimental results[108].

After 1.5ns, the first peak becomes higher and sharper, indicating that there are more ZnS bonds formed. The system at that moment consists of several ion pairs, a planar $(ZnS_3)^{4-}$ cluster (Figure 5.6), and three Zn^{2+} ions interacting with the sulphide ions within the cluster.

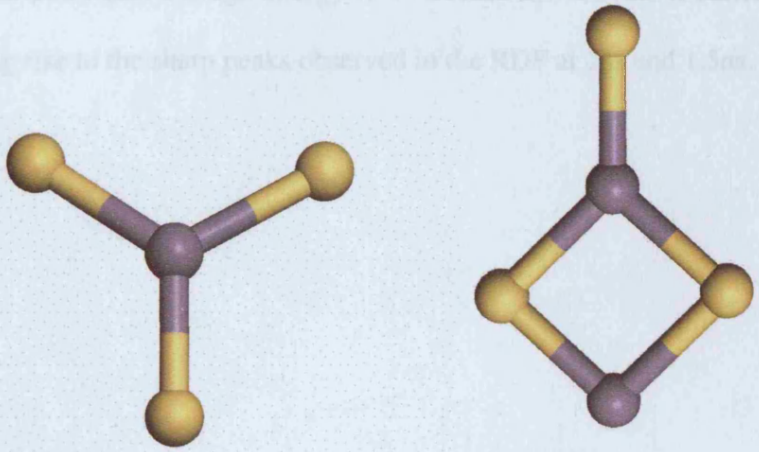

Figure 5.6

Structure of two of the first clusters formed in solution: $(ZnS_3)^{4-}$ and $(Zn_2S_3)^{2-}$.

The processes described above refer explicitly to one of the two NVT simulations performed at 300K and 0.5M concentration. However, as noted, we carried out two simulations (with different initial configurations) at each temperature and concentration, to assess the influence that the choice of the random initial configuration has over the final results. It is gratifying that in the other simulation, which is not discussed in detail, the process is similar, even the final cluster is the same. Indeed, in all the systems studied, the results of the two simulations are similar, with some obvious differences appearing due to the different starting points, but the cluster formation processes show the same general features. We may therefore have reasonable confidence in the generality of our results.

0.75M concentration.

The RDF of one of the two simulations of 0.75M systems is shown in Figure 5.7. During the first 50ps, the ion pairs start to form. At 0.5ns the network of ion pairs is already created, generating a series of "threads" that expand all across the unit cell. Eventually, some of those ion pairs gain enough energy to overcome the activation barriers and form ZnS bonds, giving rise to the sharp peaks observed in the RDF at 1ns and 1.5ns.

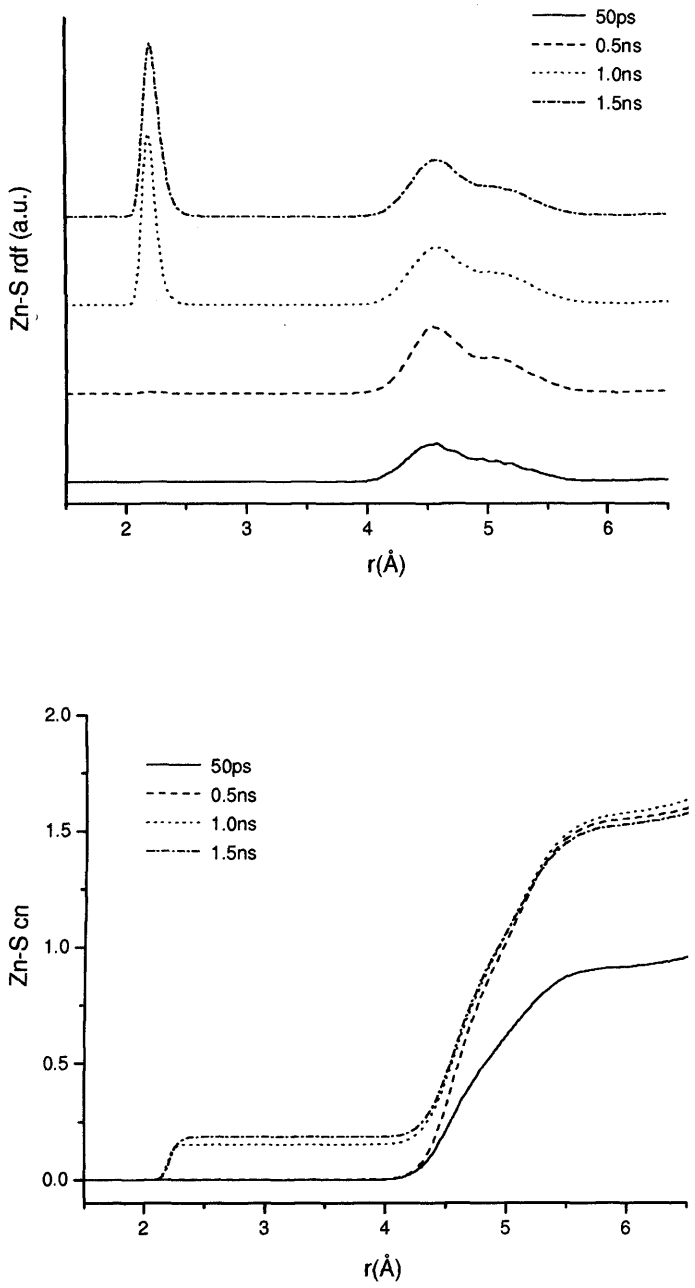

Figure 5.7

Zn-S RDFs and coordination numbers during the simulation, at a 0.75M concentration.

In simulations at 0.5M only the $(ZnS_3)^{4-}$ cluster is formed after 1.5ns, while the rest of the ions are still forming ion pairs. At 0.75M, we also observe the initial formation of this cluster. Therefore, once a ZnS cluster is formed it attracts additional S^{2-} ions rather than Zn^{2+} in hexa-aquo complexes, and forms first a $(ZnS_2)^{2-}$ cluster; again, this triplet will attract a further S^{2-} to form the $(ZnS_3)^{4-}$ cluster. To understand this behaviour we note that once a ZnS cluster is formed, the very stable hydration shell of six water molecules is broken and the Zn atom is weakly attached to only three water molecules (Figure 5.3). So when a S^{2-} anion approaches it, it will be easier to remove one of these water molecules than the water molecules interacting with a single Zn^{2+} cation; hence growth into a $(ZnS_2)^{2-}$ cluster is more facile than dissociation of another hexa-aquo complex. This feature is general and is observed in all simulations at room temperature. Nucleation does not start as an extended process in which Zn and S atoms from all the system form small clusters that subsequently aggregate and grow. Rather it is an activated process, triggered by the rupture of ion pairs. In this sense, it could be argued that the critical nucleus is a ZnS cluster, because once that cluster is formed, it will start growing. A similar effect has been observed in simulations of the nucleation of AgBr from solution[106], where the critical cluster size is found to be between 1 and 3 AgBr units.

The $(ZnS_3)^{4-}$ cluster attracts the positively charged $Zn(H_2O)_6^{2+}$ complexes, which move around it, until one of them overcomes the energy barrier allowing the Zn^{2+} ion to attach to the cluster. A very stable $(Zn_2S_3)^{2-}$ cluster is then formed (Figure 5.6), which does not grow during the rest of the simulation.

Previous experimental studies[92] of ZnS nucleation from water solution proved that the first stage of the ZnS nucleation is the creation of small clusters of 1:1 stoichiometry, followed by the formation of clusters with 3 S: 2 Zn stoichiometry. Although the systems they studied have a much lower concentration, the atomic processes involved must be similar in both cases; therefore our simulations give insight into the structure of those initial clusters, as well as the path followed in their growth.

1M concentration

For this high concentration, the formation of ZnS clusters occurs very quickly. The network of ion pairs occupies a large volume, fluctuating in the entire box, creating regions with high concentrations of ZnS and regions with only water. Figure 5.8 shows the RDF of one of the 1M systems.

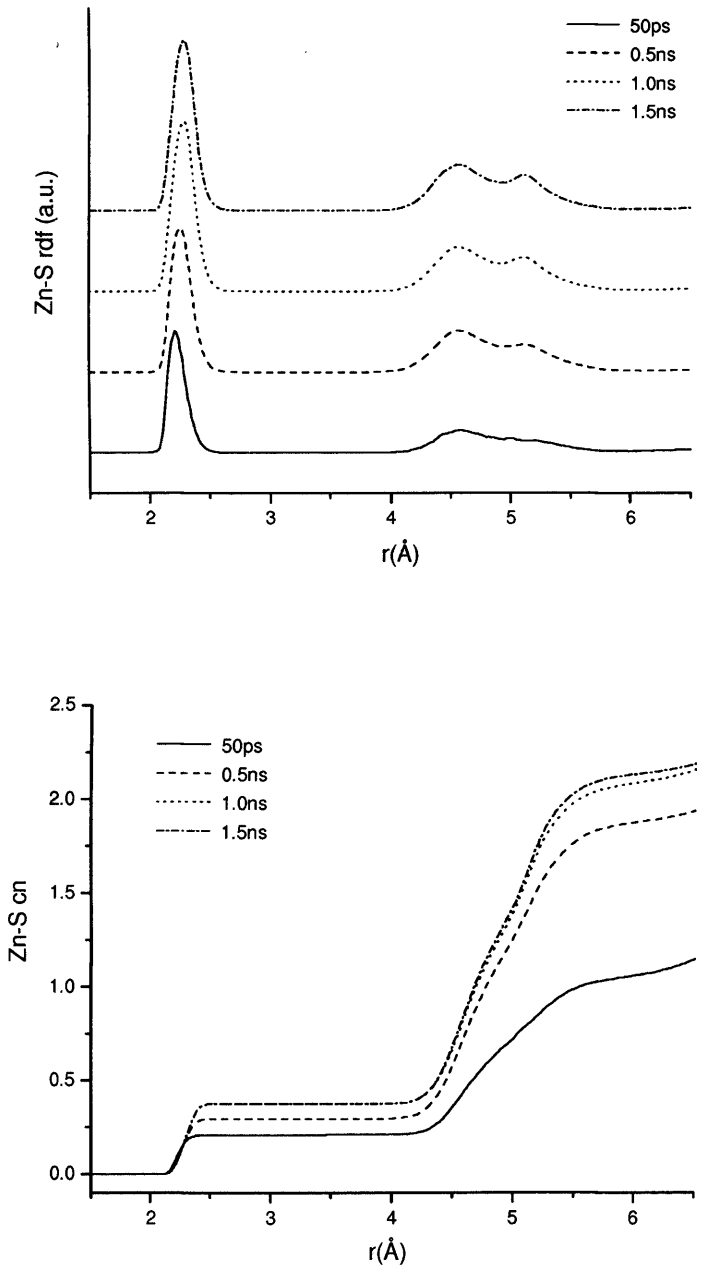

Figure 5.8

Zn-S RDFs and coordination numbers during the simulation, at a 1.0M concentration.

In the first 50ps the peak associated with the ion pair network is starting to form, as well as the peak associated with ZnS clusters. After 0.5ns, ZnS and $(ZnS_3)^{4-}$ clusters appear. The same physical reasons that make these two small clusters more likely to bind extra atoms than isolated ions also make then more likely to come together and form a $(Zn_2S_4)^{4-}$, which happens before 1ns of simulation. This cluster does not undergo further growth in the next 1.5ns. No other ion pair is broken to form a ZnS cluster in that period, as can be noted from the RDF. Figure 5.9 shows a snapshot of the system at 1.5ns. It is interesting to note the clear distinction between the regions of high and low ZnS concentration. $Zn(H_2O)_6^{2+}$ complexes have a stronger interaction with isolated S^{2-} ions (forming ion pairs) than with large clusters like $(Zn_2S_4)^{4-}$. For this reason, the latter are pushed away from the region of high ZnS concentration, as can be seen in Figure 5.9, a factor that slows down the process of cluster growth.

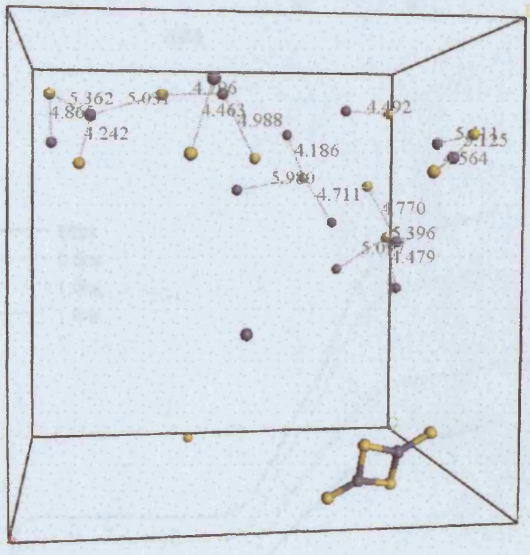

Figure 5.9

Snapshot of the system with 1.0M concentration at 1.5ns. Water molecules have been removed to allow a clear view of the Zn and S atoms. The distances between atoms forming ion pairs are shown. Note the wide range of distances over which the ion pairs exist, vibrating around the energy minimum at 4.6Å.

1.25M concentration

The behaviour of the system at this high concentration is somewhat different from that at lower concentrations. As in the case of 1.0M concentration, ZnS units are rapidly formed, which now, however, happens in many places simultaneously. As a result, the RDF (Figure 5.10) shows the first peak even before the network of ion pairs has been formed.

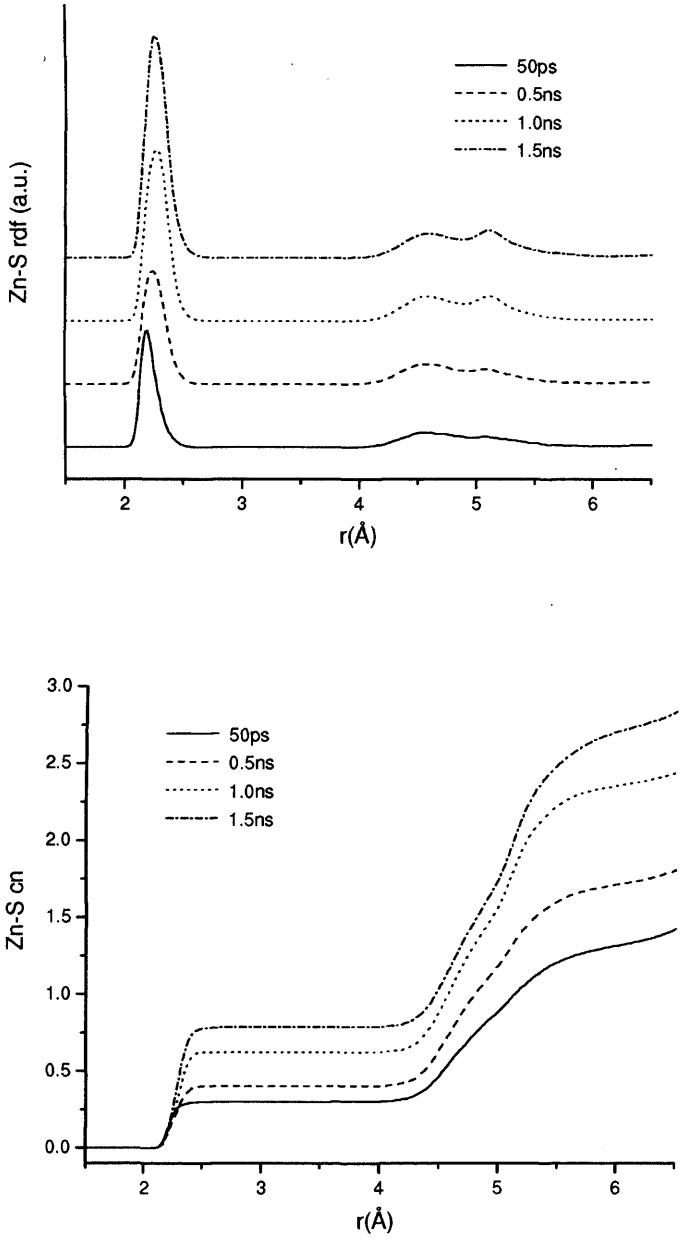

Figure 5.10

Zn-S RDFs and coordination numbers during the simulation, at a 1.25M concentration.

These small clusters aggregate to form larger clusters such as the previously described $(Zn_2S_3)^{2-}$ and $(Zn_2S_4)^{4-}$ clusters. But the most interesting result from the simulation at high concentrations is that we can see the creation of large clusters, which would require much longer simulation times to be observed at low concentrations. In one of the simulations, two $(Zn_2S_4)^{4-}$ clusters are formed, and coexist for a while. During the simulation they interact with the same $Zn(H_2O)_6^{2+}$ complex, which stays between them. Thermal motion eventually provides sufficient energy to break the complex, and the Zn^{2+} sticks to one of the clusters. Once the complex is broken, the other $(Zn_2S_4)^{4-}$ cluster is able to stick to the same Zn^{2+} ion, forming a large $(Zn_5S_8)^{6-}$ cluster, which has an almost linear structure. The large negative charge of that cluster causes another Zn^{2+} to be attracted to form $(Zn_6S_8)^{4-}$, which has a very unstable initial configuration, but undergoes a structural rearrangement to achieve the stable structure shown in Figure 5.11.

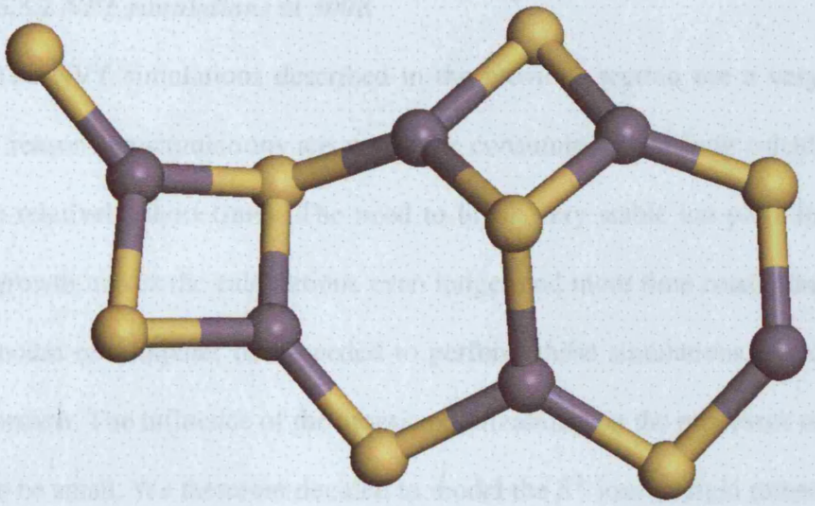

Figure 5.11

$(Zn_6S_8)^{4-}$ cluster formed after 1.5ns simulation in the system with 1.25M concentration. The structure is close to planar, and its building units are squares and hexagons, the same building units of the bubble clusters that are the most stable structures of $(ZnS)_n$ clusters in vacuo for n=10-47.

The striking characteristic of the latter cluster is that it does not have four coordinated atoms. Zn atoms have a higher coordination number than S atoms, but they are only two or three coordinated. Ab initio and interatomic potential based calculations[93, 109] have proved that the minimum energy structures for $(ZnS)_n$ clusters with n=6-47 are the so-called "bubble clusters", spheroidal structures composed of the arrangement of squares (Zn_2S_2 rings) and hexagons (Zn_3S_3 rings), in which all the atoms are three coordinated. It is not surprising then that non-stoichiometric clusters like the ones we show here also have three coordinated atoms. The $(Zn_6S_8)^{4-}$ cluster has two squares and two hexagons, which are the structural units of the bubble clusters.

5.3.2 *NPT simulations at 300K*

The NVT simulations described in the previous section use a very small timestep. For this reason the simulations are very time consuming, with long calculations needed to simulate relatively short times. The need to break very stable ion pairs in order to permit cluster growth makes the calculations even longer and more time consuming. In view of the large amount of computer time needed to perform these simulations, we decided to take a new approach. The influence of the atomic polarizability on the processes of ion aggregation seems to be small. We therefore decided to model the S^{2-} ions as rigid rather than polarizable ions, enabling an increase in the timestep up to 1fs that allows us to make a more efficient use of the computer time. We also considered that there could be significant volume changes due to the changes in the hydration spheres when the clusters grow, which would be better modelled in the NPT ensemble, where the Nosé-Hoover[115, 116] thermostat and barostat are used to maintain the system at room temperature and pressure. With these changes, we are able to simulate the systems for 6ns, which allows us to gain further insight into the nucleation process.

0.5M concentration.

In one of the two simulations at this concentration, we do not see the formation of any ZnS cluster: all ions stay in solution during the whole 6ns, indicating the high stability of the ion pairs and the large energy barrier that prevents their rupture. In the other simulation, a $(Zn_2S_4)^{4-}$ cluster like the one shown in Figure 5.9 is formed, confirming that when an ion pair is broken to form a ZnS cluster, this cluster undergoes further growth quickly.

0.75M concentration.

Systems at this concentration form larger clusters than at 0.5M. The process of cluster formation is easier to understand through the use of schematic figures, as in Figure 5.12. During the first nanosecond the clusters that are formed are the usual ones that start cluster growth: $(ZnS_2)^{2-}$ and $(ZnS_3)^{4-}$. After 1.6ns, a cluster is formed with a structure that is very representative of the way in which nucleation of ZnS occurs. The $(Zn_3S_6)^{6-}$ cluster has a planar, hexagonal-like structure, which is one of the building units of the bubble clusters. It is also a building unit of larger planar clusters such as the one in Figure 5.11. The addition of a $(ZnS_2)^{2-}$ cluster to it generates a species with a high negative charge, which is very unstable, and needs to attach another Zn^{2+} cation in order to undergo a transformation and gain a stable configuration, consisting of two planar hexagons sharing an edge. After 50ps one S atom forms a new bond bridging two Zn atoms, creating a square. As a result, the structure is no longer planar. An arrangement of hexagons alone would not be able to form a closed structure; they can only form planes (as in the graphite structure). Indeed, as discussed in reference [109], Euler's law states that it is necessary to have 6 squares in order to bend the structure and enclose a volume. So the addition of squares to an arrangement of hexagons bends the structure; the more squares present, the more bent it will be. After 4.4ns no more changes of the cluster are observed.

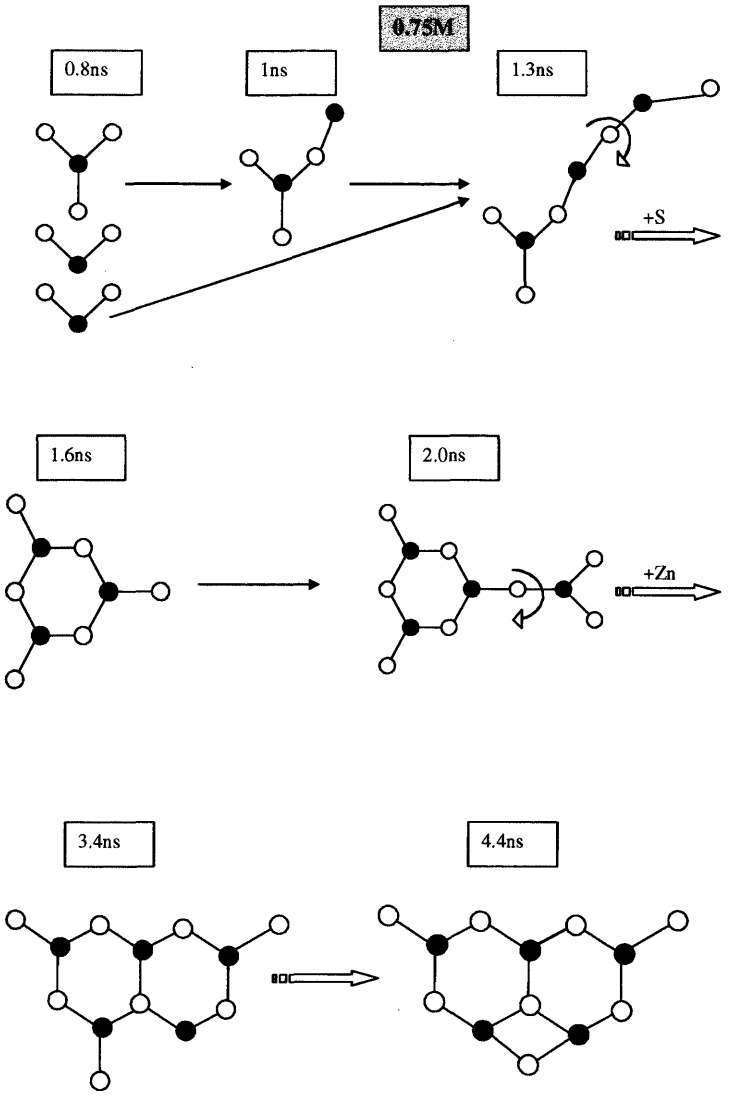

Figure 5.12

Schematic representation of the cluster formation process. Black circles represent Zn atoms, white circles represent S atoms and grey circles represent Zn atoms coordinated to four S in a tetrahedral arrangement. Bonds crossed by a semicircular arrow have freedom to rotate. This figure shows the results of one of the two systems simulated at 0.75M. (The same colour codes and representations apply to the rest of the figures from Figure 5.13 to Figure 5.16, at the concentrations indicated).

Figure 5.13 shows the behaviour of the other system studied with a 0.75M concentration. The most remarkable feature is the appearance of clusters with four coordinated atoms. After 1.2ns a $(Zn_3S_5)^{4-}$ cluster is formed in which a Zn atom is surrounded by four S atoms placed at the vertices of a tetrahedron, which is the local environment of Zn atoms in the bulk phases of ZnS. But the structure is only transient, and when a new Zn atom is attached, the cluster is transformed, to one with a planar structure comprising a hexagon and a square sharing one edge. Therefore, the presence of a Zn ion with the tetrahedral structure of the bulk is not sufficient to nucleate the crystal formation and induce the clusters to grow as bulk-like structures. The clusters present in the initial stages of crystal growth are preferentially planar; four coordinated atoms are only transient structures that easily evolve and become three coordinated.

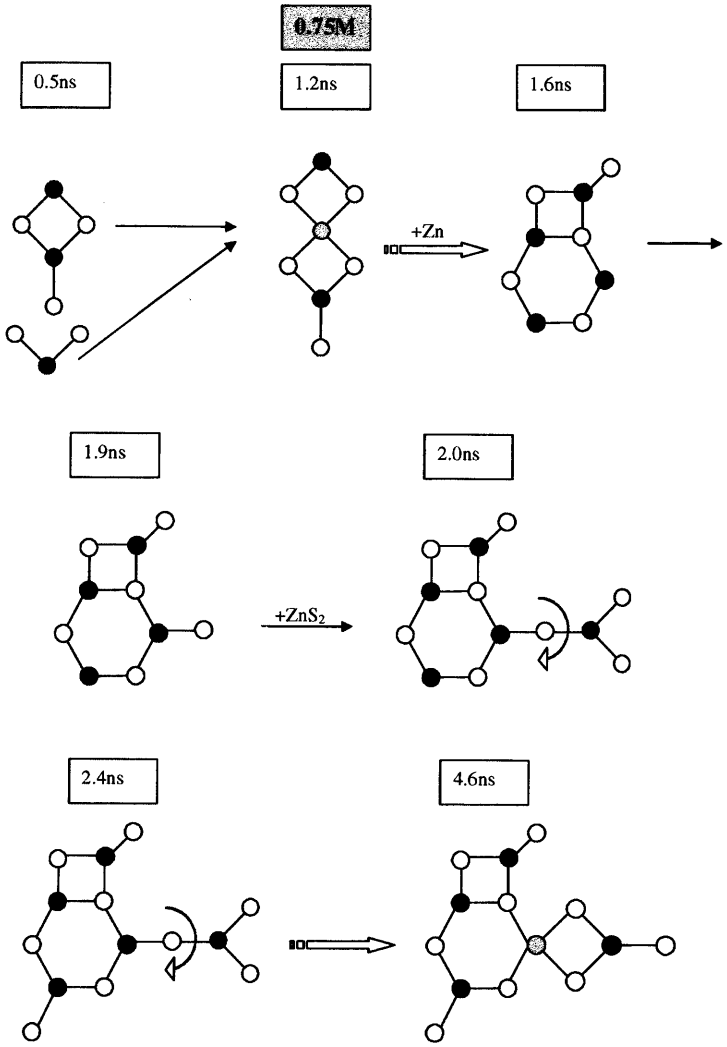

Figure 5.13

1M concentration.

The two systems with 1M concentration have similar behaviour (see Figure 5.14 and Figure 5.15). Although formed at different times, the final clusters in both systems are $(Zn_2S_4)^{4-}$ and $(Zn_3S_6)^{6-}$. The main difference between them is that in one case the $(Zn_3S_6)^{6-}$ cluster has a planar structure while in the other there is a four coordinated Zn atom with tetrahedral arrangement. The difference in total energy between the two structures show that this non-planar structure is more stable than the planar one by 0.1eV, so if the simulation was longer we could see the cluster jumping the energy barrier to undergo a structural transformation and become non-planar. But as seen for the systems with a 0.75M concentration, that structure can easily be changed when other atoms are attached and new planar clusters are more likely to be formed.

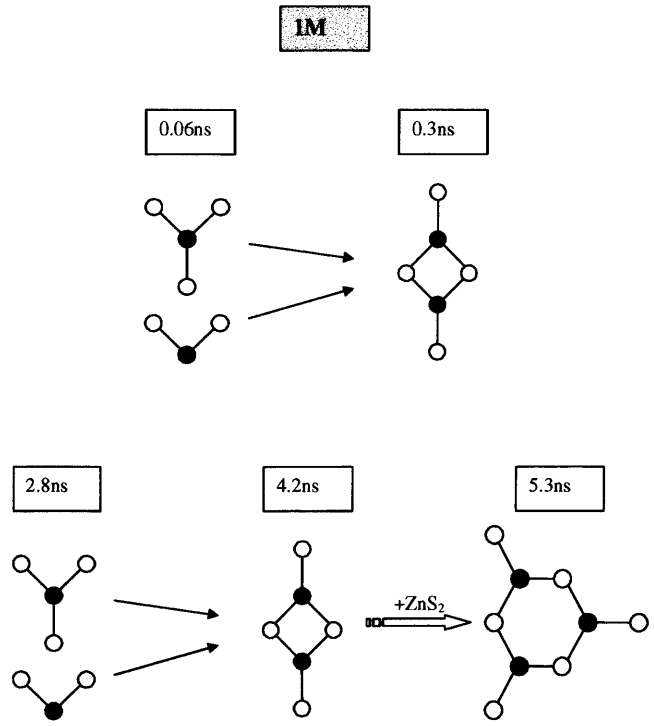

Figure 5.14

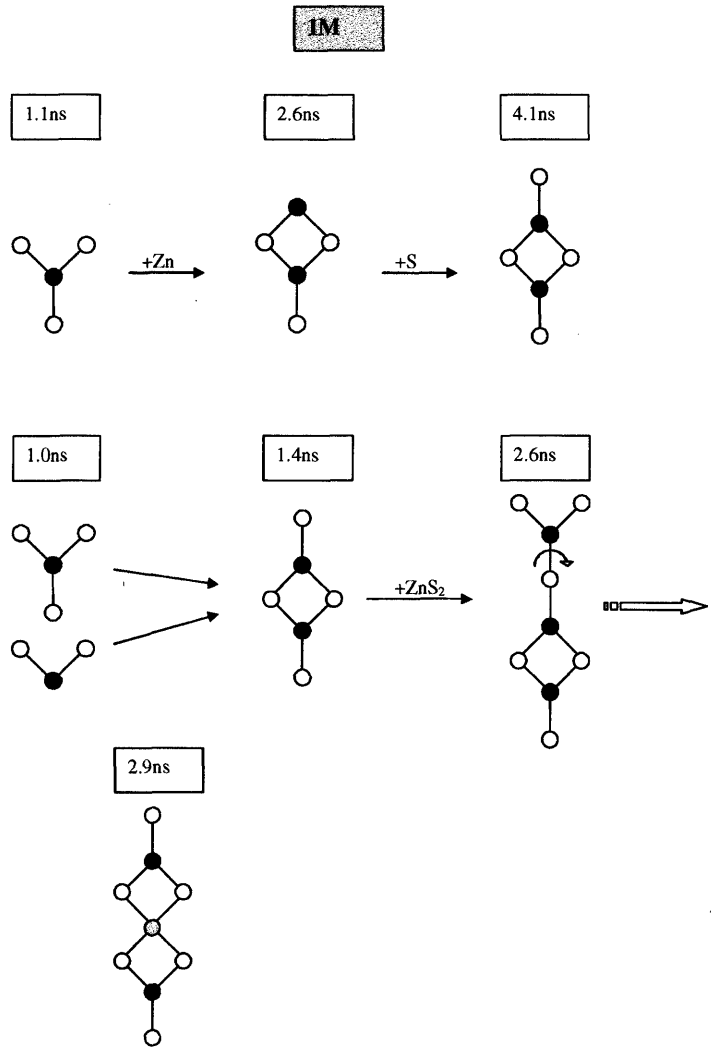

Figure 5.15

1.25M concentration.

At this concentration, larger clusters are formed (see Figure 5.16 and Figure 5.17). $(Zn_3S_6)^{6-}$ clusters are formed approximately at 3ns in the two systems simulated at this concentration. One of the systems has the planar configuration of the $(Zn_3S_6)^{6-}$ cluster, while the other one has the non-planar configuration. They remain as they are for the other 3ns of

the simulation, indicating that the energy barrier between the two conformations is quite high. More clusters are formed in other regions of the system; most are close to planar structures formed by squares and hexagons.

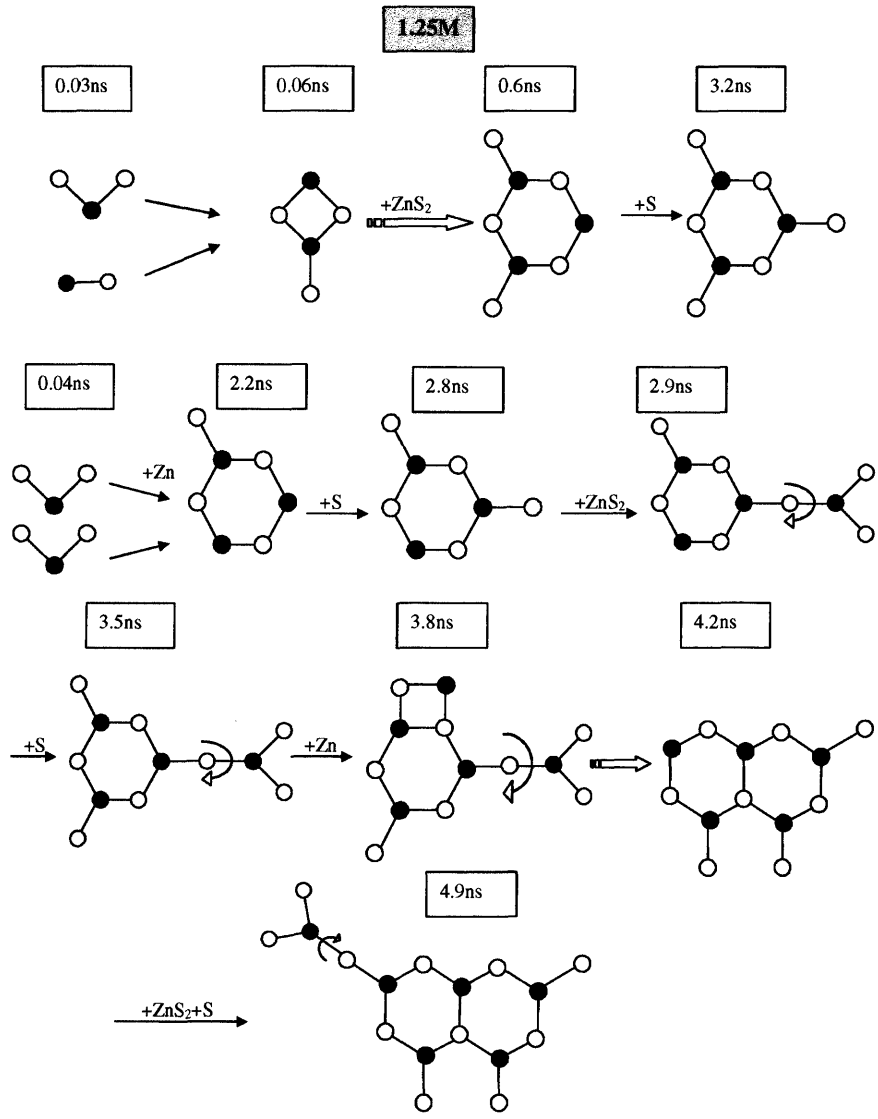

Figure 5.16

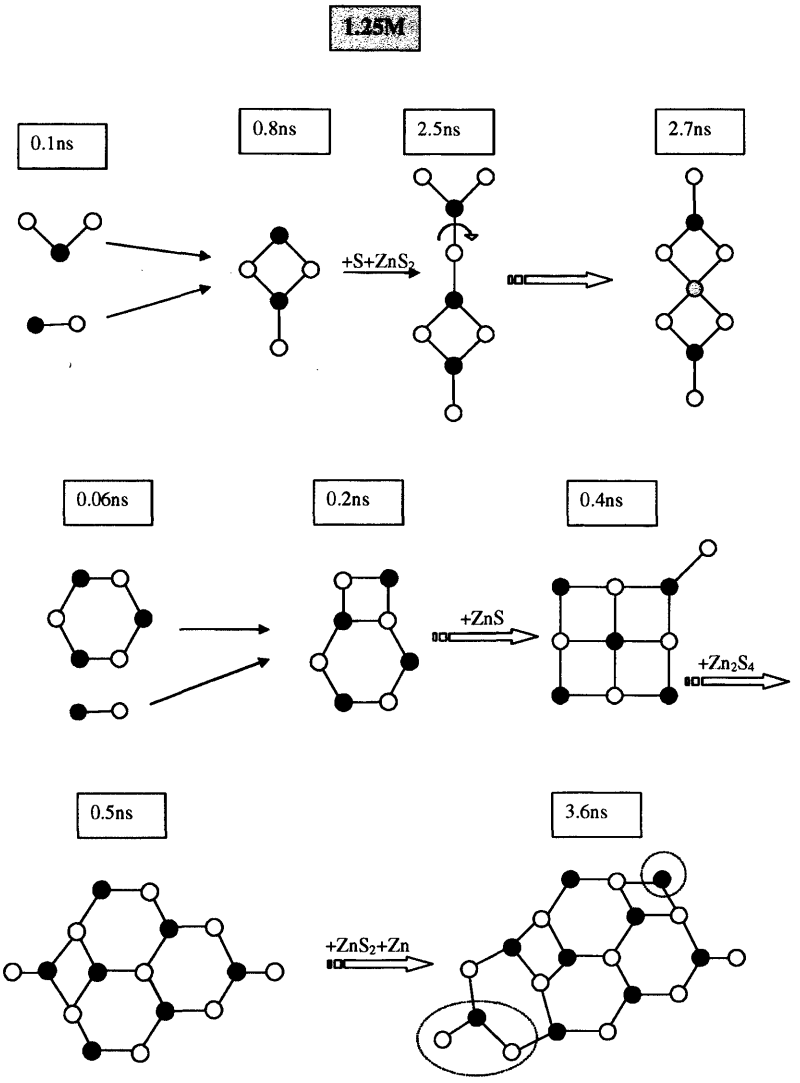

Figure 5.17

The largest cluster created at 6ns time is shown in Figure 5.18. It has 11 S and 9 Zn atoms. There are 4 hexagons and 3 squares. The presence of the 3 squares results in a bent structure, so the cluster has the shape of an open bubble, suggesting that the following step in the nucleation process of ZnS is the creation of closed bubble clusters, which are the most stable structures in vacuo. The open bubble of Figure 5.18 does not have water molecules in the region that would be the inner region of the bubble, so addition of more atoms would not enclose any water molecules inside. There are only slight changes in volume in all the

simulations we performed. But if hollow bubble clusters were created, this would generate an expansion of the system due to the creation of forbidden regions for the water molecules; the larger the bubble the bigger the expansion. It would be interesting if this effect could be observed experimentally

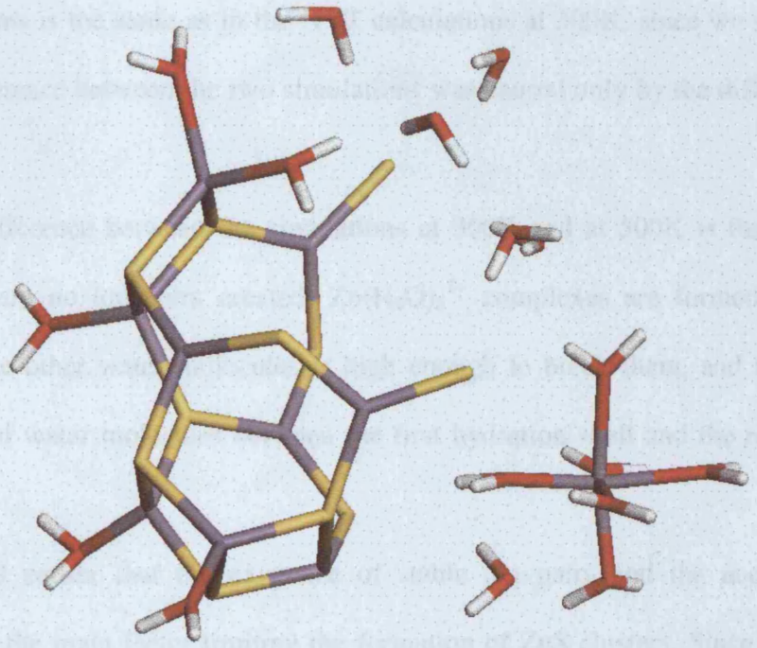

Figure 5.18

$(Zn_9S_{11})^{4-}$ cluster formed after 6ns simulation in the system with 1.25M concentration. The structure is non-planar, due to the presence of three squares, making it similar to a bubble cluster. There are no water molecules bound to the internal side of the developing bubble, suggesting that the addition of more atoms would easily form a closed bubble without water inside.

5.3.3 *NVT simulations at 500K*

In order to assess the influence of temperature on our system, we decided to perform simulations at the higher temperatures of 500K. Due to the increase in ion velocities at this temperature we do not need very long simulations to observe the initial stages of cluster growth, so we simulated the systems for 0.5ns. Polarizability via the shell model is included for the S^{2-} ions and the Evans[18, 19, 112] thermostat is used to run NVT simulations. The volume of the systems is the same as in the NVT calculations at 300K, since we wished to ensure that any difference between the two simulations was caused only by the difference in temperature.

The main difference between the simulations at 300K and at 500K is that at high temperatures there are no ion pairs created: $Zn(H_2O)_6^{2+}$ complexes are formed, but the kinetic energy of the other water molecules is high enough to break them, and there is a constant exchange of water molecules between the first hydration shell and the rest of the liquid.

We observed earlier that the existence of stable ion pairs and the necessity of breaking them were the main factor limiting the formation of ZnS clusters. Since there are no ion pairs at 500K, the process of cluster growth is much faster. After a few picoseconds of simulation, we see the formation of several ZnS and $(ZnS_2)^{2-}$ clusters, which occurs in all the systems studied, regardless of the concentration. Unlike the case of 300K (in which higher concentrations allowed a faster growth due to the higher probability of breaking ion pairs), at 500K there are no significant differences in the rate at which clusters are formed for the different concentrations, because every time a Zn^{2+} approaches a S^{2-} a new bond is created. The aggregation process is therefore only limited by the ions diffusion rates.

The small clusters formed at the beginning have the same structures as at 300K; $(ZnS_2)^{2-}$, (Zn_2S_2), $(Zn_2S_3)^{2-}$, etc. The only one that does not appear at 500K is the highly charged $(ZnS_3)^{4-}$: most of the S atoms are already attached to other Zn atoms, so there is only a small chance that a $(ZnS_2)^{2-}$ cluster finds an isolated sulphur ion. The differences

between the two temperatures become more apparent for larger clusters. At 300K we saw that the structures are mainly planar, with a very few closed configurations. At 500K, the atoms have more kinetic energy, which allows them to jump the energy barriers between different conformations; hence the lower energy configurations are found more easily. We therefore see the formation of several clusters that are also found to be the global minima structures in vacuum (Figure 5.19).

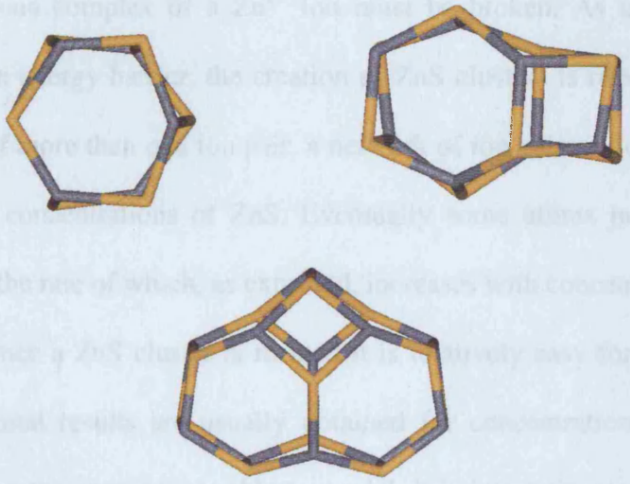

Figure 5.19

Structures of clusters formed in the calculations at 500K. The thermal motion at this high temperature allows induces jumps over energy barriers, and bubble clusters are formed faster than at 300K.

Clusters, however, do not always grow through a succession of minima. Sometimes the process is so fast that a cluster does not have enough time to rearrange and find the minimum before more atoms are attached to it, which happens for example in the calculations with high concentrations (1M and 1.25M), where the final states are very disordered clusters containing all the ions in the simulation; large clusters are formed, with a bubble-like region, while in other regions there are four coordinated atoms. For low concentrations the total number of ions is small, which makes it easier to find the global minima and the final structures are bubble clusters with only three coordinated atoms.

5.4 Summary and Conclusions

Our molecular dynamics simulations have given a new insight into the processes of nucleation of ZnS in aqueous solution. At room temperature Zn^{2+} ions interact with 6 water molecules to form very stable $Zn(H_2O)_6^{2+}$ complexes. These complexes attract by Coulomb forces the S^{2-} ions in solution (which do not form stable complexes) and form ion pairs. Ion pairs are stable units, with a mean Zn - S separation of 4.6Å. In order to form a ZnS cluster the aqueous complex of a Zn^{2+} ion must be broken. As the process has an appreciable activation energy barrier, the creation of ZnS clusters is relatively slow. Since S^{2-} ions can be part of more than one ion pair, a network of ion pairs is formed, creating regions of high and low concentrations of ZnS. Eventually some atoms jump the barrier and form ZnS clusters, the rate of which, as expected, increases with concentration.

Once a ZnS cluster is formed it is relatively easy for growth to continue. Although experimental results are usually obtained for concentrations that are thousands of times lower than the ones we are able to model, it is interesting to note that they suggest that the initial clusters formed have a 1:1 Zn to S stoichiometry, in agreement with our predictions. They also find that the next step is the formation of clusters with a S/Zn ratio of 3/2, which in our simulations is a planar cluster. These clusters continue growing due to the high concentration of our solutions, so we are not able to elucidate whether these planar clusters are the same predominant units observed experimentally at very low concentration.

As shown in the 3 previous chapters, by using global minimization techniques, the most stable structures of $(ZnS)_n$ clusters with n=6-47 are not bulk-like but bubble clusters - hollow clusters in which all the atoms are three coordinated. Our simulations show that the initial ZnS clusters formed in water solutions are not bulk-like. We found that they typically form planar structures that can be regarded as components of bubble clusters. When they reach a large size they begin to bend, acquiring a structure that is even more similar to that of the bubbles. Owing to computer time limitations, we are not able to see the formation of a closed bubble at 300K, but our calculations suggest that it should be the next step in the

nucleation process. The formation of the ZnS crystal structures must therefore be achieved at a later stage.

In summary, the process of ZnS nucleation and crystal growth, predicted from simulations, and confirmed in part by experiments is as follows: firstly small ZnS clusters form in solution when ion pairs are broken. These clusters continue growing and become bubble clusters[109]. Bubble clusters continue growing and become double bubbles[110], which have some four coordinated atoms. At some stage, a rearrangement of the network of four coordinated atoms must happen for larger clusters, leading to the creation of the known ZnS crystal phases. Small nanocrystals are more likely to show a wurtzite structure[117]. Finally, for some particle size (which must be larger than 3nm) the surface/bulk ratio is small enough to allow the formation of the sphalerite structure, which is the most stable crystal phase of ZnS.

CONCLUSIONS AND FUTURE WORK

The use of computer simulations has provided a new insight into the fascinating physics and chemistry of nanosize ZnS. Our simulations model, with an acceptable accuracy, the geometry and properties of the bulk and surfaces of ZnS, which allows a systematic study of the morphology of small crystals, on the basis of the Gibbs criterion.

With the aim of gaining an understanding of stages closer to the nucleation, we studied the structures of $(ZnS)_n$ clusters in vacuo, with n=10-47. Structures and properties appropriate for bulk systems, are often not valid for systems with very few atoms. And indeed, we have found that the most stable configurations for the small clusters studied do not show any crystal-like region, not even in the inner core. They have a structure that is completely different, based on hollow spheroids, which we named bubbles, in which all the atoms are three-coordinated, despite the fact that in the two ZnS crystal phases usually found in nature (sphalerite and wurtzite) both Zn and S are four-coordinated. In recent years this surprising behaviour has been found in several compounds, such as AgI, GaN, BN, ZnO, CdS. It has been recently[118] suggested that clusters of compounds that, in the bulk, form tetrahedrally coordinated structures are likely to exhibit these hollow structures; but the reasons why are far from clear yet.

Continuing the study of ZnS clusters, we then calculated the structures of larger clusters: $(ZnS)_{50}$, $(ZnS)_{60}$, $(ZnS)_{70}$ and $(ZnS)_{80}$, finding another unexpected result. For these larger clusters the structure is no longer a single bubble, but two of them, one inside the other. We named these structures double bubbles. Atoms in the inner bubble are bonded to those in the outer bubble, so this is the first case in which four-coordinated atoms appear in ZnS clusters. This group of four-coordinated atoms changes the properties of the whole cluster. The effect could be used by experimentalists aiming to detect the formation of

double bubbles. In this thesis we have indicated some of the properties that could be used to detect both single and double bubbles.

Our final study is concerned with the formation and subsequent growth of ZnS clusters from aqueous solution. The formation of ion pairs slows down the process, but nevertheless we observed the formation of the very first clusters in water, which usually are non-stoichiometric, having more S than Zn atoms, which we rationalize by noting that, unlike Zn^{2+} cations, S^{2-} anions do not interact strongly with water; they are more stable as part of ZnS clusters. There are no four-coordinated atoms; the structures of the clusters are usually planar adopting four-atom and six-atom rings from which the bubble clusters are built up. Our simulations show that ZnS clusters grow smoothly towards a bubble-like configuration. Due to computer time limitations we were not able to observe the complete formation of a bubble cluster in water; but all our results suggest that this process will occur.

Overall, the simulations presented in this thesis enable us to provide a general picture of the process by which ZnS crystals are formed. Firstly, individual atoms come together to form small clusters, which initially tend to be negatively charged. These clusters have planar structures, and will grow until they form bubble clusters. The size range in which $(ZnS)_n$ bubble clusters are stable is n=10-47. When more atoms are attached, they form double bubbles, which can grow increasing the size of both inner and outer shells. Experimental studies in BN suggest the existence of double and triple bubbles. But at some point, the presence of a network of four-coordinated atoms in the multilayered structures might induce the formation of the first bulk-like region, which is likely to happen for cluster sizes of 2-3nm. That bulk-like region might be different from that of the two ZnS crystal phases. In that case, a rearrangement of the structure must occur afterwards, since particles larger than 3-4nm have wurtzite structure. Finally, another rearrangement must occur after further growth of the clusters, because the most stable crystal structure for macroscopic crystals is sphalerite.

All these processes clearly suggest that the nucleation and crystal growth of ZnS is much complex than that described by the Classical Nucleation Theory. The failure of CNT to explain nucleation in this system, as well as in several other relevant systems, increases the necessity of carrying out more nucleation studies, with the ultimate goal of elaborating a new Nucleation Theory.

Much of the work described in this thesis has been published in the open literature, see references [94, 109, 110].

There are many interesting problems that it has not been possible to investigate in the limited period of time available to do a PhD, among them:

~ Our calculations predict that $(ZnS)_{13}$ cluster has a remarkable behaviour, because it is particularly unstable compared to $(ZnS)_{12}$ and $(ZnS)_{14}$. However, laser ablation experiments show that $(ZnS)_{13}$ is a "magic cluster", in the sense that it is much more common than any other cluster. It would be desirable to perform a detailed study of this cluster. Our results suggest that are kinetic rather than thermodynamic factors which will stabilize it. Another part of that study would be to perform *ab initio* calculations on the charged clusters $(ZnS)_{12}^{+}$, $(ZnS)_{13}^{+}$ and $(ZnS)_{14}^{+}$, which are the ones measured in the mass spectra.

~ Another interesting study would be to continue the prediction of larger $(ZnS)_n$ clusters using global minimization techniques, to see whether a sphalerite or wurtzite bulk structure appears, or perhaps a new bulk structure not present in macroscopic crystals. For values of n of 256 and 512, clusters of sizes 2.5nm and 3.5nm respectively could be modelled.

~ The MD simulations of cluster formation in aqueous solutions could be easily continued. Perhaps the best option would be to model only the higher concentration (1.25M), with a slightly larger unit cell, in order to include more Zn^{2+} and S^{2-} ions, and observe the complete formation of a bubble cluster.

~ Finally, another interesting study would be the simulation of the processes of bubble cluster growth and aggregation. This could be performed using two sets of NPT simulations, both at ambient conditions. In one set, an already formed bubble cluster would be inserted in liquid water, as well as a certain amount of Zn^{2+} and S^{2-} ions in solution. During the simulation, some of them would be attached to the bubble, which must then undergo a rearrangement to minimize its energy. The second set of simulations would be to insert two or more bubble clusters in liquid water, and observe how they aggregate to form larger clusters.

Bibliography

[1] J. Haleblian, W. McCrone, *J. Pharm. Sci.* **1969**, *58*, 911.

[2] J. Huang, W. Lu, L. S. Bartell, *J. Phys. Chem.* **1995**, *99*, 11147.

[3] S. Auer, D. Frenkel, *Nature* **2001**, *413*, 711.

[4] J. Anwar, P. K. Boateng, *J. Am. Chem. Soc.* **1998**, *120*, 9600.

[5] H. Gleiter, *Adv. Mater.* **1992**, *4*, 474.

[6] Y. Wang, N. Herron, *J. Phys. Chem.* **1991**, *95*, 525.

[7] J. Muilu, T. Pankanem, *Surf. Sci.* **1996**, *364*, 439.

[8] V. Albe, C. Jouanim, D. Bertho, *J. Crystal Growth* **1998**, *184/185*, 388.

[9] L. E. Brus, *J. Chem. Phys.* **1983**, *79*, 5566.

[10] P. P. Ewald, *Ann. Phys. (Leipzig)* **1921**, *64*, 253.

[11] B. G. Dick, A. W. Overhauser, *Phys. Rev.* **1958**, *112*, 90.

[12] D. H. Gay, A. L. Rohl, *J. Chem. Soc., Faraday Trans.* **1995**, *91*, 925.

[13] W. Smith, T. R. Forester, *J. Molecular Graphics* **1996**, *14*, 136.

[14] L. Verlet, *Phys. Rev.* **1967**, *159*, 98.

[15] R. W. Hockney, *Methods Comput. Phys.* **1970**, *9*, 136.

[16] W. G. Hoover, J. C. Ladd, B. Moran, *Phys. Rev. Lett.* **1982**, *48*, 1818.

[17] J. C. Ladd, W. G. Hoover, *Phys. Rev. B* **1983**, *28*, 1756.

[18] D. J. Evans, *J. Chem. Phys.* **1983**, *78*, 3297.

[19] D. J. Evans, W. G. Hoover, B. H. Failor, B. Moran, J. C. Ladd, *Phys. Rev. A* **1983**, *28*, 1016.

[20] P. J. D. Lindman, M. J. Gillan, *J. Phys.: Condens. Matter.* **1993**, *5*, 1019.

[21] P. J. Mitchell, D. Fincham, *J. Phys.: Condens. Matter.* **1993**, *5*, 1031.

[22] R. Ferneyhough, D. Fincham, G. D. Price, M. J. Gillan, *Modell. Simul. Mater. Sci. Eng.* **1994**, *2*, 1101.

[23] J. M. Thijssen, *Computational Physics*, Cambridge University Press, **1999**.

[24] K. Raghavachari, B. Anderson, *J. Phys. Chem.* **1999**, *100*, 12960.

[25] P. Hohenberg, W. Kohn, *Phys. Rev. B* **1964**, *136*, 864.

[26] G. R. Parr, W. Yang, *Density functional theory of atoms a molecules*, Oxford University Press, **1989**.

[27] W. Kohn, L. J. Sham, *Phys. Rev. A* **1965**, *140*, 1133.

[28] J. P. Perdew, A. Zunger, *Phys. Rev. B* **1981**, *23*, 5048.

[29] S. H. Vosko, L. Wilk, Nussair, *Can. J. Phys.* **1980**, *58*, 1200.

[30] A. D. Becke, *J. Chem. Phys.* **1986**, *84*, 4524.

[31] B. G. Johnson, P. M. W. Gill, J. A. Pople, *J. Chem. Phys.* **1993**, *98*, 5612.

[32] A. D. Becke, *J. Chem. Phys.* **1992**, *97*, 9173.

[33] B. Delley, *J. Chem. Phys.* **1990**, *92*, 508.

[34] B. Delley, *J. Chem. Phys.* **2000**, *113*, 7756.

[35] J. Baker, *J. Comp. Chem* **1986**, *7*, 385.

[36] J. P. Perdew, J. A. Chevary, S. H. Vosko, K. A. Jackson, M. R. Pederson, D. J. Singh, C. Fiolhais, *Phys. Rev. B* **1992**, *46*, 6671.

[37] J. P. Perdew, Y. Wang, *Phys. Rev. B* **1992**, *45*, 13244.

[38] H. J. Monkhorst, J. D. Pack, *Phys. Rev. B* **1976**, *13*, 5188.

[39] J. W. Gibbs, *Collected Works*, Longman, New York, **1928**.

[40] G. Z. Wulff, *Krystallogr.* **1901**, *34*, 449.

[41] S. D. Loades, S. W. Carr, D. H. Gay, A. L. Rohl, *J. Chem. Soc., Chem. Comm.* **1994**.

[42] M. S. D. Read, M. S. Islam, G. W. Watson, F. King, F. E. Hancock, *J. Mater. Chem.* **2000**, *10*, 2298.

[43] F. Bertaut, *Compt. Rend. Acad. Sci. (Paris)* **1958**, *246*, 3447.

[44] P. W. Tasker, *J. Phys. C: Solid State Phys.* **1979**, *12*, 4977.

[45] P. M. Oliver, G. W. Watson, S. C. Parker, *Phys. Rev. B* **1995**, *52*, 5323.

[46] A. Wander, F. Schedin, P. Steadman, A. Norris, R. McGrath, T. S. Turner, G. Thornton, N. M. Harrison, *Phys. Rev. Lett.* **2001**, *86*, 2811.

[47] J. H. Harding, *Surf. Sci.* **1999**, *442*, 87.

[48] R. Horst, P. M. Pardalos, N. V. Thoai, *Introduction to Global Optimization*, 2nd ed. ed., Kluwer, Dordrecht, **2000**.

[49] J. D. Pintér, *Global Optimization in Action*, Kluwer, Dordrecht, **1996**.

[50] S. Kirkpatrick, J. C. D. Gellat, M. P. Vecchi, *Science* **1983**, *220*, 671.

[51] W. J. Boettinger, J. H. Perepezko, *Rapidly Solidified Crystallite Alloys*, TMS-AIME, Warrendale, PA, **1985**.

[52] S. Mann, G. A. Ozin, *Nature* **1996**, *382*, 313.

[53] M. Kulmala, L. Pirjola, J. M. Mäkelä, *Nature* **2000**, *404*, 66.

[54] D. B. Fahrenheit, *Phil. Trans. Roy. Soc.* **1724**, *39*.

[55] D. Turnbull, J. C. Fisher, **1949**, *17*, 71.

[56] E. R. Buckle, *Proc. R. Soc. London* **1961**, *A261*, 189.

[57] D. W. Oxtoby, *J. Phys.: Condens. Matter.* **1992**, *4*, 7627.

[58] K. Wright, R. A. Jackson, *J. Mater. Chem.* **1995**, *5*, 2037.

[59] J. D. Gale, *J. Chem. Soc., Faraday Trans.* **1997**, *93*, 629.

[60] R. W. G. Wyckoff, *Crystal Structures, Vol. 2*, Second ed., Interscience Publishers, **1967**.

[61] D. L. Lide, *Handbook of chemistry and physics*, 80th ed., CRC Press, **1999-2000**.

[62] H. Bilz, W. Kress, *Phonons dispersion relations in Insulator*, Springer-Werlag, New York, **1979**.

[63] C. B. Duke, *J. Vac. Sci. Technol. B* **1983**, *1*, 732.

[64] C. B. Duke, Y. R. Wang, *J. Vac. Sci. Technol. A* **1989**, *7*, 2035.

[65] T. T. Rantala, T. S. Rantala, V. Lantto, J. Vaara, *Surf. Sci.* **1996**, *77*, 352.

[66] D. C. Sayle, C. R. A. Catlow, J. H. Harding, M. J. F. Healy, S. A. Maicaneanu, S. C. Parker, B. Slater, G. W. Watson, *J. Mater. Chem.* **2000**, *10*, 1315.

[67] C. R. A. Catlow, D. S. Coombes, D. Lewis, J. C. G. Pereira, *Chem. Mater.* **1998**, *10*, 3249.

[68] C. B. Duke, A. Paton, A. Kahn, *J. Vac. Sci. Technol. A* **1984**, *2*, 515.

[69] H. Sasakura, H. Kobayashi, S. Tanaka, J. Mita, T. Tanaka, H. Nakayama, *J. Appl. Phys.* **1981**, *52*, 6901.

[70] K. Hirabayashi, O. J. Kogure, *J. Appl. Phys.* **1985**, *24*, 1484.

[71] Y. R. Wang, C. B. Duke, *Phys. Rev. B* **1987**, *36*, 2763.

[72] C. Mailhiot, C. B. Duke, D. J. Chadi, *Surf. Sci.* **1985**, *149*, 366.

[73] H. Zhang, F. Huang, B. Gilbert, J. F. Banfield, *J. Phys. Chem. B* **2003**, *107*, 13051.

[74] N. H. d. Leeuw, J. A. Purton, S. C. Parker, G. W. Watson, G. Kresse, *Surf. Sci.* **2000**, *452*, 9.

[75] N. H. d. Leeuw, S. C. Parker, C. R. A. Catlow, G. D. Price, *Phys. Chem. Minerals* **2000**, *27*, 332.

[76] F. Jones, A. L. Rohl, J. B. Farrow, W. v. Bronswijk, *Phys. Chem. Chem. Phys.* **2000**, *2*, 3209.

[77] D. Ferry, A. Glebov, V. Senz, J. Suzanne, J. P. Toennies, H. Weiss, *J. Chem. Phys.* **1996**, *105*, 1697.

[78] M. J. Stirniman, G. Huang, R. S. Smith, S. A. Joyce, B. D. Kay, *J. Chem. Phys.* **1996**, *105*, 1295.

[79] N. H. d. Leeuw, G. W. Watson, S. C. Parker, *J. Chem. Soc., Faraday Trans.* **1996**, *92*.

[80] N. H. d. Leeuw, S. C. Parker, *Phys. Rev. B* **1999**, *60*, 13792.

[81] A. Marmier, P. N. M. Hoang, S. Picaud, C. Girardet, R. M. Lynden-Bell, *J. Chem. Phys.* **1998**, *109*, 3245.

[82] N. H. d. Leeuw, S. C. Parker, *Phys. Rev. B* **1998**, *58*, 13901.

[83] K. F. Lau, H. E. ALper, T. S. Thacher, T. R. Stouch, *J. Phys. Chem.* **1994**, *98*, 8785.

[84] P. D'Angelo, V. Barone, G. Chillemi, N. Sanna, W. Meyer-Klaucke, N. V. Pavel, *J. Am. Chem. Soc.* **2002**, *124*, 1958.

[85] H. W. Kroto, J. R. Heath, S. C. O'Brien, R. F. Curl, R. E. Smalley, *Nature* **1985**, *318*, 162.

[86] S. Iijima, *Nature (London)* **1991**, *354*, 51.

[87] N. G. Chopra, R. J. Luyken, K. Cherrey, V. H. Crespi, M. L. Cohen, S. G. Louie, A. Zetti, *Science* **1995**, *269*, 966.

[88] P. A. Parrilla, A. C. Dillan, K. M. Jones, G. Riker, D. L. Schulz, D. S. Ginley, M. J. Heben, *Nature* **1999**, *397*, 114.

[89] D. Golberg, Y. Bando, M. Eremets, K. Takemura, K. Kurashima, H. Yusa, *Appl. Phys. Lett.* **1996**, *69*, 2045.

[90] D. Golberg, Y. Bando, O. Sthéphan, K. Kurashima, *Appl. Phys. Lett.* **1998**, *73*, 2441.

[91] T. Oku, A. Nishiwaki, I. Narita, M. Gonda, *Chem. Phys. Lett.* **2003**, *380*, 620.

[92] G. W. Luther, S. M. Theberge, D. T. Rickard, *Geochim. Cosmochim. Acta* **1999**, *63*, 3159.

[93] J. M. Matxain, J. E. Fowler, J. M. Ugalde, *Phys. Rev. A* **2000**, *61*, 053201.

[94] S. Hamad, S. Cristol, C. R. A. Catlow, *J. Phys. Chem. B* **2002**, *106*, 11002.

[95] A. D. Becke, *J. Chem. Phys.* **1993**, *98*, 5648.

[96] M. J. Frisch, G. W. Trucks, H. B. Schlegel, G. E. Scuseria, M. A. Robb, J. R. Cheeseman, V. G. Zakrzewski, J. J. A. Montgomery, R. E. Stratmann, J. C. Burant, S. Dapprich, J. M. Millam, A. D. Daniels, K. N. Kudin, M. C. Strain, O. Farkas, J. Tomasi, V. Barone, M. Cossi, R. Cammi, B. Mennucci, C. Pomelli, C. Adamo, S. Clifford, J. Ochterski, G. A. Petersson, P. Y. Ayala, Q. Cui, K. Morokuma, D. K. Malick, A. D. Rabuck, K. Raghavachari, J. B. Foresman, J. Cioslowski, J. V. Ortiz, A. G. Baboul, B. B. Stefanov, G. Liu, A. Liashenko, P. Piskorz, I. Komaromi, R. Gomperts, R. L. Martin, D. J. Fox, T. Keith, M. A. Al-Laham, C. Y. Peng, A. Nanayakkara, M. Challacombe, P. M. W. Gill, B. Johnson, W. Chen, M. W. Wong, J. L. Andres, C. Gonzalez, M. Head-Gordon, E. S. Replogle, J. A. Pople, Gaussian, Inc., Pittsburgh PA, **1998**.

[97] W. J. Stevens, M. Krauss, H. Basch, P. G. Jasien, *Can. J. Chem.* **1992**, *70*, 612.

[98] A. Burnin, J. J. Belbruno, *Chem. Phys. Lett.* **2002**, *362*, 341.

[99] J. L. Gavartin, A. M. Stoneham, *Phil. Trans. Roy. Soc. London A* **2003**, *361*, 275.

[100] O. Stéphan, Y. Bando, A. Loiseau, F. Willaime, N. Shramchenko, T. Tamiya, T. Sato, *Appl. Phys. A* **1998**, *67*, 107.

[101] H. Zhang, B. Gilbert, F. Huang, J. F. Banfield, *Nature* **2003**, *424*, 1025.

[102] T. Nirasawa, V. R. Romanyuk, V. Kumar, S. V. Mamykin, K. Tohji, B. Jeyadevan, K. Shinoda, T. Kudo, O. Terasaki, Z. Liu, R. V. Belosludov, V. Sundararajan, Y. Kawazoe, *Nature* **2004**, *3*, 99.

[103] S. Woodley, A. Sokol, C. R. A. Catlow, *Z. Anorg. Allg. Chem.* **2004**, *630*, The page number will be added in the proofs reading stage.

[104] R. W. Godby, M. Schluter, L. J. Sham, *Phys. Rev. Lett.* **1986**, *56*, 2415.

[105] R. W. Godby, M. Schluter, L. J. Sham, *Phys. Rev. Lett.* **1988**, *37*, 10159.

[106] J. D. Shore, D. Perchak, Y. Shnidman, *J. Chem. Phys.* **2000**, *113*, 6276.

[107] M. Labrenz, G. K. Druschel, T. Thomsen-Ebert, B. Gilbert, S. A. Welch, K. M. Kemmer, G. A. Logan, R. E. Summons, G. D. Stasio, P. L. Bond, B. Lai, S. D. Kelly, J. F. Banfield, *Science* **2000**, *290*, 1744.

[108] G. R. Helz, J. M. Charnock, D. J. Vaughan, C. D. Garner, *Geochim. Cosmochim. Acta* **1993**, *54*, 15.

[109] E. Spanó, S. Hamad, C. R. A. Catlow, *J. Phys. Chem. B* **2003**, *107*, 10337.

[110] E. Spanó, S. Hamad, C. R. A. Catlow, *Chem. Commun.* **2004**, 864.

[111] G. Lamoureux, B. Roux, *J. Chem. Phys.* **2003**, *119*, 3025.

[112] D. J. Evans, G. P. Morris, *Computer Physics Reports* **1984**, *1*, 297.

[113] T. Miyanaga, Y. Sawa, Y. Sakane, I. Watanabe, *Phys. B: Condens. Matter* **1995**, *208-209*, 393.

[114] P. R. t. Wolde, D. Frenkel, *Science* **1997**, *277*, 1975.

[115] W. G. Hoover, *Phys. Rev. A* **1985**, *31*, 1695.

[116] S. Melchionna, G. Ciccotti, B. L. Holian, *Molec. Phys.* **1993**, *78*, 533.

[117] H. Zhang, J. F. Banfield, *Nano Lett.* **2004**, *4*, 713.

[118] A. Wootton, P. Harrowell, *J. Phys. Chem. B* **2004**, *108*, 8412.